Rio de Janeiro, Rio de Janeiro

August 26, 2024

Advanced Lithography Methods for Creating Josephson Junctions and Superconducting Circuits at Nano and Micro Scales

A Thesis Presented to the
Brazilian Center of Physics Research
in Candidacy for the
Degree of Doctor in Physics

M.Sc. Arthur C. M. Rebello,
Supervised by: Prof. Dr. JoÃčo Paulo Sinnecker,
Co-supervisor: Prof. Dr. Francisco Rouxinol,
Co-supervisor: Prof. Dr. Ivan S. Oliveira

Advanced Lithography Methods for Creating Josephson Junctions and Superconducting Circuits at Nano and Micro Scales

M.Sc. Arthur Chianelli Monteiro Rebello

Centro Brasileiro de Pesquisas FÃŋsicas

August 26, 2024

MINISTÉRIO DA CIÊNCIA, TECNOLOGIA E INOVAÇÃO

GOVERNO FEDERAL BRASIL UNIÃO E RECONSTRUÇÃO

"ADVANCED LITHOGRAPHY METHODS FOR CREATING JOSEPHSON JUNCTIONS AND SUPERCONDUCTING CIRCUITS AT NANO AND MICRO SCALES"

ARTHUR CHIANELLI MONTEIRO REBELLO

Tese de Doutorado em Física apresentada no Centro Brasileiro de Pesquisas Físicas do Ministério da Ciência Tecnologia e Inovação. Fazendo parte da banca examinadora os seguintes professores:

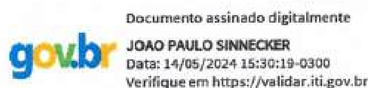

João Paulo Sinnecker - Orientador/CBPF

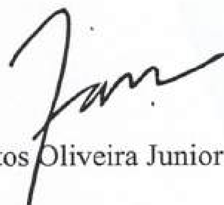

Ivan dos Santos Oliveira Junior - Coorientador/ CBPF

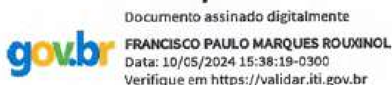

Francisco Rouxinol - Coorientador/ IFGW-UNICAMP

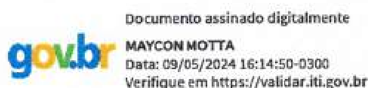

Maycon Motta - UFSCAR

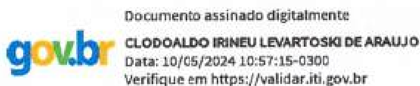

Clodoaldo Irineu Levartoski de Araujo – UFV

Centro Brasileiro de Pesquisas Físicas
Rua Doutor Xavier Sigaud, 150, URCA, Rio de Janeiro, Brasil
Tel.: +55 21 2141-7100 CEP:22290-180
http://www.cbpf.br

gov.br Documento assinado digitalmente
YUTAO XING
Data: 10/05/2024 11:58:50-0300
Verifique em https://validar.iti.gov.br

Yutão Xing - titular/ UFF

gov.br Documento assinado digitalmente
JORLANDIO FRANCISCO FELIX
Data: 10/05/2024 15:09:06-0300
Verifique em https://validar.iti.gov.br

Jorlandio Francisco Felix - UNB

Rio de Janeiro, 09 de maio de 2024.

Centro Brasileiro de Pesquisas Físicas
Rua Doutor Xavier Sigaud, 150, URCA, Rio de Janeiro, Brasil
Tel.: +55 21 2141-7100 CEP:22290-180
http://www.cbpf.br

Contents

1 Introduction **1**
1.1 Quantum Computing . . . 2
1.1.1 Josephson Junctions . . . 2
1.1.2 Objective . . . 3
1.1.3 Structural Overview of this Thesis . . . 4

2 Theoretical Foundation **5**
2.1 One-Dimensional Microwave Cavities . . . 5
2.1.1 Lumped Element Electrical Harmonic Oscillator . . . 5
2.1.2 The Lossless Line . . . 7
2.1.3 S-parameter . . . 7
2.2 Coupled Resonator . . . 8
2.3 Josephson Equations . . . 9
2.3.1 Superconducting Quantum Interference Devices . . . 10
2.4 Cavity Quantum Electrodynamics . . . 11
2.4.1 Superconducting Qubits . . . 11
2.4.2 Atom-Cavity Coupling . . . 14
2.5 Quantum Processing Unit . . . 15
2.5.1 Architecture . . . 16

3 Simulation **20**
3.1 Simulation Methodology . . . 20
3.1.1 Circuit Analysis and Simulation . . . 21
3.1.2 Qiskit Metal . . . 22
3.1.3 Qutip . . . 23

4 Results **24**
4.1 Nanofabrication Procedures . . . 24
4.1.1 Physical Vapor Deposition . . . 24
4.1.2 Lithography Overview . . . 27
4.1.3 Photolithography . . . 28
4.1.4 Etching . . . 34
4.1.5 Superconducting Circuits . . . 40

4.1.6 Scanning Electron Microscope . . . 40
4.1.7 Nanolithography EBL . . . 41
4.2 Josephson Junctions Fabrication Modeling . . . 46
4.2.1 Point Spread Function . . . 49
4.2.2 Proximity Effect Correction . . . 50
4.2.3 Integrating the PSF Over Josephson Junction Lithography Patterns . . . 51
4.3 Nanofabrication results on Josephson Junctions . . . 52
4.3.1 Partial Conclusion and Discussion . . . 61
4.4 Further Results on Josephson Junctions . . . 61
4.4.1 Josephson Junctions Fabrication Procedure . . . 62
4.4.2 Dose Tests . . . 64
4.4.3 Considerations on Angle of Deposition . . . 71
4.4.4 Considerations on e-Beam Developers . . . 72
4.4.5 Josephson Junction Lift-off Process . . . 73
4.4.6 Defining Recipe Stability Metric from Room Temperature Measurements . . . 75
4.4.7 SEM Junction Area Analysis . . . 76
4.4.8 General Josephson Junction Fabrication Results . . . 77
4.4.9 Sample Mounting . . . 84
4.5 Simulation Results and Low Temperature Measurements . . . 85
4.5.1 Measurement Setup . . . 85
4.5.2 One Qubit Chip Design and Simulation . . . 89
4.5.3 Trilayer Circuit - Horseshoe Junction - Sample Characterization . . . 93

5 Conclusions and Perspectives 99
5.1 Four Qubit QPU Perspectives . . . 99
5.1.1 Chip Fabrication . . . 100
5.2 Accomplishments . . . 100
5.2.1 Acknowledgements . . . 103
5.2.2 Abbreviations . . . 103

A Four qubit Quantum Processing Unit 104

B Superconducting Circuits 109

C Trilayer Al/Nb/Al Circuit Recipe 113

List of Figures

1.1 Artistic image of the Eagle QPU, adapted from [1]. 1

2.1 Diagrams for three levels of abstraction of microwave cavivity. a) Cavity modeled by lumped elements. b) Plot of the real and imaginary parts of the impedance of an oscillator. c) Cavity modeled as impedance per length. d) Cavity modeled as infinite series of resistors, inductors, conductance and capacitance lumped elements. e) S parameter model diagram. 6

2.2 On the left we have a quantum harmonic oscillator with fixed capacitance C and Inductance L, on the right is the anharmonic oscillator produced by the nonlinear Josephson Junction in the circuit (box with x inside). 13

2.3 a) Two multiplexed waveguides coupled to a feed line, the top one is $\lambda/2$ while the bottom one is a $\lambda/4$ waveguide due to one end being shorted. The first four harmonics are displayed for each variant. The capacitors are referred to as hang capacitors. To the left hanger type capacitor, to the right interdigitaded capacitor. b) Waveguide capacitively coupled on both sides, transmon diagram is placed near indicating interaction with standing waves generated by the oscillator. 16

2.4 Variations of the transmon qubit: transmon, X transmon, concentric transmon, unimon qubits. The x indicates position of Josephson junctions. 17

2.5 Qistkit Metal components, they can be used to put together CQED circuits. Components include: a) capacitors , b) hanger coupler, c) wirebond pads, d) line tee, e) line tee couplers, f) qubits and others. 19

4.2 Top left: Argon Magnetron Sputtering, Wafer mounted ready for thin film deposition. Top right: Magnetron sputtering of Nb film onto wafer, 2 cm distance from target to wafer and the sample is spinning through the entire process to ensure an even deposition. Bottom: Magnetron Sputtering diagram showing magnetic field lines trapping nearby argon atoms, which become ionized and trapped by magnetic fields near the sputtering target. Ions are repeatedly bombarded against the target metal, this case Nb. Atoms which are dislodged make their way to the target, the pressure in the deposition chamber is raised to 3 mTorr, in order to have enough argon to keep the plasma on. 25

4.3 Bottom left: Aluminum metal in the e-beam crucible, brightness in the bottom of the image indicates the source of electron beam. The beam is deflected on to the aluminum, which melts and begins to evaporate on the samples above (Top Left). Right: E-beam deposition diagram, electrons are created by heated filament and accelerated towards a target material, heating the material until it boils and evaporates. The substrate has angle adjustment and is placed about a meter away from the crucible, enabling anisotropic deposition. 27
4.4 On the left we have a measurement of an 1 micrometer capacitor finger made of resist, on a optical microscope. Right: wafer after developing and heat treatment to harden resist for the etching procedure. 29
4.6 Wafer map, Displacement measurement cross. Image of wafer with circle pointing out blurry alignment marks. The blue arrow indicate where centering the wafer would probably land accoding to the wafermap. The user should then use one of the green arrow paths to find a cross and align the wafer. 32
4.7 Diagram of ion milling system. Argon gas is stripped of its electrons, then subjected to an electric field. After acceleration it passes by a heated tungsten filament, and is neutralized by the free electrons. It then makes its way to mechanically remove atoms from the surface. Al_xO_y is easily removed by this method. 34
4.8 SEM image showing left over resist on Josephson junctions. Green arrows indicate polymer leftovers. 35
4.9 Reactive ion etching of Nb with SF_6 and Ar plasma diagram. A diagram shows the interaction of the particles with the RF field, creating a plasma over the sample. a) Etching of Nb over Si with SF_6. b)Etching of Nb over a passive layer of Al with SF_6. 36
4.10 a)Wafer showing uneven etching, b) wafer with damaged substrate, c) close up of damaged region in optical microscope. d,e)Etching of Si/Nb Wafer, goes from dark silvery color to dark grey (f). g-i) SEM images demonstrating overetching of up to 800 nm (measurements are not exact as the sample is clearly at a very high angle $> 80°$, however there is still some distortion.SF_6 is a powerful Si etchant, once the Nb layer is etched away it begins to fiercely remove the Si. Proving difficult to optimize reproducible recipes.g) two contact structures for deposition of Josephson junctions. h,i) Close up shows overetched substrate. 37
4.11 Top : Images of patterned trilayer wafer Al (20 nm)/ Nb (80nm) / Al (20 nm) before and after dry etching. At this point only two layers Nb (80nm) / Al (20 nm) are left on the substrate. Starting from the top left, patterned wafer after wet etching. Center image shows wafer positioned on the RIE carbon chuck in the etching chamber, Since Al is etched at much slower rate, it protects the substrate. The Al can be easily removed with wet etching procedures. Top Right shows wafer after etching the dark silvery color transforms into very light and reflective metalic color with only a thin film of Al 20 nm patterned region. Bottom: Two SEM images (20k mag and 60k mag) of Josephson Junction intersection with previously fabricated pads on trilayer Si/Al/Nb/Al Wafer. This angled image shows good contact, and that the Si wafer was preserved during etching. 38
4.12 In the image a trilayer film Al (20 nm)/ Nb (80nm) / Al (20 nm) Si wafer is seen, a particularly pristine sample with a very high yield. 39

4.13 LABNANO CBPF Raith e-Line 30 kV field emission electron beam lithography system on the left, device capable of nanometric patterning on ultra flat surfaces such as Silicon or Saphire wafers. On the right simulation of deposited energy by e-beam for the specific resist stack explored in this study to fabricate Josephson Junctions. 42
4.1 Top) LABNANO CBPF, photo lithography system Heilderberg DWL 66+. Bottom) LFDQ IFGW AJA Magnetron sputtering and angled e-beam deposition system. 44
4.5 a) The first image shows the wafer positioned within the spinner covered with resist. b) Resist defects: shooting star and edge fringes. c) Perfect resist deposition, no visible shooting stars, the coating is evenly spread with out contaminants. d) This image shows how the wafer is properly aligned. It is critical that the drawing is oriented according to the crystallography of the wafer for cutting purposes. By setting the wafer chanfer flat on the positioning screws, then pushing towards the back screw, guarantees less variation between exposures. 45
4.14 Schematic representation of the pattern transferred onto a double-layer resist stack followed by aluminium deposition process, delineating the steps involved in fabricating Josephson junctions, alongside electron trajectory simulation within the resist layers. a) Dolan Josephson junction scheme showcasing the exposed area (in dark blue) and the central bridge region (in grey). b) Bird's-eye perspective of the anticipated Josephson junction bridge structure. c) Initial 30° angle deposition, d) oxidation phase, e) subsequent -30° angle deposition. f) Representation of the Josephson junction post-lift-off process, with the green coating symbolizing the AlO_x layer. g) Visualization of electron dispersion trajectories in a 230 nm PMMA layer (top) and a 500 nm MMA Co-polymer layer (bottom), both situated on a silicon substrate, under the influence of a 30 kV electron beam. The trajectories of the primary electrons from the incident beam are depicted in blue, whereas the backscattered electrons are illustrated in red. 47
4.15 Point spread functions calculated via Casino and Urpec or Raith e-line commercial software. The Casino simulation resulted in three PSF (Full, only backscattered, only incident). The raith software allows for the PSF to be calculated at any height within the resist stack. . . 49
4.16 On the left a square next to a bigger polygon, and it is noticeable how the small feature affects the big one and vice versa. The dose distribution is aimed at making up for this issue and making the dose more homogeneous throughout the geometry. On the right PEC applied to horseshoe junction pattern. This distribution is created to minimize pattern distortion. 51
4.17 E-beam Pattern integrated with the PSF, and a 10 nm step size. From left to right: thin Dolan, L and horseshoe patterns. The color diagram is with respect to dose intensity in arbitrary units. Exposed regions received the same dose for all patterns, furthermore integration was done over an area of 10 μm x 10 μm, with a respective step size of 10 nm for all geometries. 51

4.18 Statistical analysis of simulated backscattered electron trajectories illustrating the correlation with angle and radius, accompanied by a schematic representation of the energy surface. a) Simulated backscattered energy versus angle, with the green dashed line indicating the 2σ confidence region. b) Radius of the deposited energy surface for backscattered electrons as determined by simulation. First 300 nm section to be within resist material selectivity threshold is from 60 to 360 nm where the fitted backscattered energy will decay 75% from start to end, region is shaded in orange. Comparative 50% decay region in shaded in green. c) The energy surface of backscattered electrons (orange shade) surrounding the incident beam (red), integrated into a cross-sectional diagram of the bridge region. The pattern areas within 500 nm of the bridge section are highlighted in red, and areas within 1000 nm are shown in light red. Red arrow depicts the beam incident direction, orange arrow shows electrons backscattered within the resist stack, green arrows indicate backscattered electrons permeating from within the substrate. 53
4.19 a) Designs employed to investigate the effects of backscattered electrons across different geometries, identified from left to right as: thin Dolan, L, and horseshoe junction designs; b) Resulting dose map from the integration of the Point Spread Function (PSF) over the thin geometry, with detailed analysis presented in panels (e) and (f). c) Detailed view of the unexposed bridge region, with percentiles marking the total deposited dose per region; (d) Colored scanning electron microscope (SEM) image of an L-shaped Josephson junction, where the blue region indicates the first deposited aluminium layer, and the AlO_x tunnelling barrier is highlighted in the center; e) Total dose distribution profiles along vertical trace, including some of exposed region (200 nm on each side), f) only 300 nm unexposed section, for horseshoe, L and Thin Dolan geometry - percentiles here denote the range of maximum dose variation; the percentages on the legend in (e) and (f) are ratio of energy deposited in the directly exposed areas to the indirectly exposed gap. (g) Angled coloured SEM images showcasing the resist stack; on the left, the Thin Dolan pattern is inscribed without bridge formation, whereas on the right, the horseshoe pattern is exposed, clearly displaying the bridge structure. Green indicates Si substrate, blue PMMA resist surface and orange for resist side walls seen at an angle. 55
4.20 Analysis of dose factors and the ratio of backscattered to total incident dose for various geometries investigated in this study. a) Distribution of backscattered electrons along a vertical trace; b) Distribution along a horizontal trace; c) Ratio of backscattered to incident dose over the vertical trace. d) Dose variation observed in a thin Dolan geometry. 56

4.21 Analysis of dose factors and the ratio of backscattered to total incident dose for proposed geometry designed to utilize backscattered electrons for undercut definition. a) The logical basis to create a new geometry, specifically conceived to tailor the distribution of backscattered electrons, thereby minimizing variance across the junction area. The blue region is intended to receive the minimal necessary dose to develop the top resist layer, with backscattered electrons being generated within the green circle region by a higher dose factor. The larger circles represent a simplified model for the overlap of backscattered regions, assuming point sources, with different colours indicating the degree of overlap. b) X junction Geometry designed with features to retain geometric resolution while achieving the (4:1) ratio for the c) total deposited dose over the vertical trace. d) Horizontal profile of the total deposited dose. e) Ratio of backscattered to incident dose for the X junction. 58
4.22 a) 3D copper cavity, on the top half a silicone chip is seen where the transmon has been deposited. b) Quantum Rabi Map provides a profile of the dynamic evolution of qubit states in a time-dependent landscape. 60
4.23 Circuit designed to measure 270 Josephson junctions. This enables to minimize variations which change from sample to sample. Isolating the properties of lithography process from the environment of perturbations due to temperature, humidity, process time and human error. 62
4.24 a) Angled SEM image of patterned resist with T type L junction prior to Al deposition, dark area in bridge region shows the undercut. b) Al e-beam vapor deposition (LFDQ), samples shown to be in angle, amber glow is seen from melted Al in the crucible below. c) SEM image of junction after double angle shadow deposition with the steps described on d-f. d) First deposition at 45° angle, e) oxidation in controlled atmosphere and f) deposition at 90 degrees to normal. g-i) Shows a small angle deposition of 30° (g), followed by oxidation (h) and finally a -30° depostion to form the contact over the oxide (i). 63
4.25 a) E-beam Pattern with applied PEC of thin Dolan junction, gap is shown to be 300 nm. b-e) SEM image of patterned resist with the Dolan junction Pattern, clearly shows teh full resist stack deteriorating. f) A particular sample where two dolan junctions were placed near each other ($4\mu m$) causing it to at least form a very brittle bridge pattern. 66
4.26 a) E-beam Pattern with applied PEC of L junction, gap is shown to be 300 nm. SEM images L junction pattern exposed onto resist, b) zoomed out image of whole exposed area, c) close up to underdosed exposure of the bridge structure. d) Bridge structure formation, e) bridge thinning due to increasing dose. 67
4.27 a) E-beam Pattern with applied PEC of horseshoe junction, gap is shown to be 300 nm. SEM images of patterned resist with the horseshoe junction pattern. b) Horseshoe junction from the contacting side, a clear gap is shown, with no MMA in the bridge region (c). Image (d) shows the view from the opposite side, here we see that the opening is has a curved shape (e). Now we look at how the opening widens as the dose is raised (f) until PMMA deteriorates (g). 68

4.28 a) E-beam Pattern with applied PEC conceived to create backscattered electrons, from the sides. This geometry was intended to test the effect of nearby expositions to bridge gap formation. Here we keep the dose of the contacting geometries constant, while varying the dose of the side structures, progressively diminishing the MMA.b-e) SEM images of progressively higher doses being applied to the side structures.It is noticeable the technique causes bridge side walls to collapse, nevertheless proves that it is possible to produced backscattered electrons in regions far (up to 4 μm) from bridge structure. 69
4.29 Angled deposition images. First image shows crack near junction area resulting from 90 degree deposition followed by 40 degree deposition. Angle measurement can be used to calculate resist height.In this case 30 degree angle first and 90 degree second deposition makes for easy resist height calculation. 71
4.30 a) A becker with a chip inside undergoing lift off procedure in Acetone or DMF solvent. b) Aluminum layer is seen completely detached from sample. c-e) SEM images of defected circuits we believed to have been damaged during this process when ultrasound is applied to speed up the process. 73
4.31 Chart displaying resistance of Josephson junction devices based on the dose applied during patterning. This chart results from a dose test deposition and the measurements of junction resistance as a function of e-beam dose. A higher dose window resulting in a functional device indicates a recipes robust to process variation. 75
4.32 a) Horseshoe e-beam pattern with applied PEC. Three out of 27 SEM images of horseshoe junction fabricated with the same dose on the same sample within the same exposure. b) Image of horseshoe junction with measured gap of 74 nm and area of 0.161 μm^2 . c) Image of horseshoe junction with measured gap of 74 nm and area of 0.170 μm^2. d) Shorted horseshoes junction with area of 0.161 μm^2. 76
4.33 Left: histogram of gap values for 17 out of the 27 junctions which were not shorted. Right: histogram of measured area through SEM imaging of the 27 samples. 77
4.34 Dose test deposition of Dolan Junctions, the tree geometries are thin medium and wide Dolan. On the first column we have underdosed junctions, on the middle column the best junctions and on the right a short circuit. a-c) Thin Dolan junctions, not one properly formed junction was registered in this dose test. d-f) Midium Dolan was the best performer and the best dose yielded a satisfactory junction (e). g-i) Wide Dolan dose test showing a well formed junction (h). 78
4.35 Examples of L junctions. a) L junction birds eye view. b) L junction with T shaped finger shown from above, developed with weak developer 300-56, top view. c) Regular L junction developed with strong 300-55 developer top view. 79
4.36 SEM image of pristine L junction deposited at 30 / -30 degrees. On the left a close up view of oxidized Al from the first deposition is contacted by non oxidized Al of the second layer. On the right the junction is seen in a zoom out view, showing its anchoring to a previously fabricated contact pad. 80
4.37 SEM images of the horseshoe junction, a) Top view of Junction, b) Angled view from the side of the junction, c) Angled view from the contact point. 81

4.38 SEM image of L type squid junction, and squid. This Squid encloses a area of 100 μm^2. a) Image of squid device, b) zoom into junction contact points. 82
4.39 Images displaying Josephson junction arrays patterned on resist and resulting deposited devices. a) Full patterned resist structure, b)zoomed view. c-f) deposited Josephson Junction array at progressively higher magnification. SEM image 83
4.40 Right: Partially cut wafer with tens of samples. Left: Sample mounted and wirebonded to sample holder with 8 ports (LFDQ). 84
4.41 LFDQ Dilution Refrigerator, in the image 4 stages can be seen. From top to bottom we have 4k, 900mk still, 100 mK cold plate and the mixing chamber flange at 10 mK. The bottom stage is able to keep 10 mK continuously using a mixture of ^{3}He and ^{4}He isotopes. 86
4.42 On the left we have VNA Experimental setup for measuring one microwave cavity. Signal is sent out from the VNA, passing through a digital variable attenuator, signal is them combined with RF STIM. A series of cryogenic attenuators, further attenuate the signals before reaching the cavity. The signal exits the cavity passing through a circulator and then a series of amplifiers before being captures once again by the VNA. Vdc is a voltage source used to apply magnetic flux to the qubit. On the right two tone qubit control and measurement experimental setup diagram. 88
4.43 Chip containing two distinct cavity qubit systems, each cavity has a distinct frequency, one projected for 5 GHz and the other 6 GHz. Qubits were projected to have the same properties, including caivty coupling of 80 MHz. 90
4.44 Here we have the convergence of the simulated qubit characteristics g, χ, charging energy (alpha), qubit frequency and delta. Capacitance Matrix simulation results acquired by ANSYS, these results are then processed using the LOM package for circuit quantization by Qiskit Metal. 92
4.45 The circuit measured which contained 96% functioning junctions along the border. Green traces are feedlines, red squares indicated capacitors, orange is the waveguide, blue indicates the fluxline. Purple indicates the qubit. 94
4.46 Left: Histogram of Resistance (kOhms) Values for the 26 samples which had resistance greater than zero, with mean value of 24.7 kOhm and standard deviation of 7.83 kOhm. On the right, updated predicted circuit values. 95
4.47 Circuit fabricated using trilayer technique and horseshoe EBL pattern. a-d) progressive zoom SEM images of the circuit and the deposited Josephson Junction, this circuit was discarded during inspection and we can see that junction is fine bur the surface has some sort of metallic residue. 96
4.48 On the left side we see the cavity dressed and bare mode, we would hope to see two Lorentzian curves, however we suspect this specific sample had a damaged capacitor. Nonetheless two resolved peaks can be seen and $\chi = 10$ MHz. On the right side a flux sweep is performed, demonstrating the attenuation of the Josephson energy using magnetic flux. 97
4.49 Left image shows bare to dressed mode oscillation due to applied flux, fitted with Qutip model. Left image displays the full energy spectrum derived from the fitting of the observed spectrum. 97

5.1 Four qubit Quantum Processing Unit, designed and fabricated. 100

A.1 Top image displays full lay out of the Four Qubit Tunable Coupler chip. In the bottom image we see a zoomed in view of the main components. 105
A.2 Top left displays gds file for x transmon, top right shows zoom in to Josephson Junction area. Bottom left shows SEM image of fabricated device with deposited Josephson junctions Bottom right shows zoom in to horseshoe junction. 106
A.3 EDS Analysis of Josephson junction deposition region. Analysis shows that all contacts are properly isolated, furthermore the Si substrate is free from Al or Nb contamination. 107
A.4 Four qubit QPU experimental set-up. In this set-up each qubit is coupled to a cavity, making a total of four multiplexed microwave cavities. The qubit control is done using a bias-T to apply microwave signals and current through the same feed line. Furthermore an additional three feed lines are used to tune couplers which can be switched on or off, connecting or isolating the qubits. 108

B.1 Metallic pads for Josephson junction probing at room temperature. The design allows for one probe to stay stationary while the pads are probed. 110
B.2 Top: Circuit with two transmon pocket qubits and one half wave capacitively coupled microwave cavity. Bottom: Two Xmon qubits connected by a third qubit serving as variable coupler. 111
B.3 Top: KITWPA Bottom: Circuit with two multiplexed Xmons qubits multiplexed to a feed line and a photonic crystal on the right side. 112

Acknowledgements

I would like to express my deepest gratitude to my wife, Maria Clara, for her unwavering support, and to my parents, Mônica and Sergio, my brother João, sister Renata and my grandmother, Marisa, for their endless encouragement. I also extend my heartfelt thanks to my entire family, whose love and belief in me have been a constant source of strength.

I am immensely grateful to my colleagues and professors for their invaluable contributions through countless discussions and overall partnership. In particular, I want to thank Dr. Naiara Klein for the many hours we spent doing e-beam lithography, and for sharing her extensive knowledge of nanofabrication techniques and process analysis. I also thank Dr. Juciane Alves for her tireless dedication to assisting LABNANO users in their research, Dr. Lucas Ruela for his deep expertise in qubit measurement techniques and his impeccable taste in board games, and Ms. Gustavo Moreira for collaborating with me on Josephson junction recipes and for having a cool motorcycle.

I am also deeply thankful to my professors: Dr. Francisco Rouxinol, for his profound knowledge in cavity quantum electrodynamics (cQED) research and for welcoming me into his laboratory, where he leads a highly talented group of students in a great atmosphere. I must extend my profound appreciation to Dr. Ivan Oliveira, for his expertise in quantum mechanics and for giving me the opportunity to work with quantum technology from the beginning. My deepest appreciation goes to my main advisor, Dr. João Paulo Sinnecker, for his guidance in nanofabrication and invaluable career advice. I consider myself very fortunate to have had these outstanding mentors, and I am incredibly grateful for their support.

I also want to thank Petrobras and CAPES for directly funding this research. I extend my gratitude to the Brazilian Center for Research in Physics (CBPF) for being the place where it all came together, and to LABNANO, the laboratory where most of this research took place. I also thank FAPERJ for funding my trips to Campinas, where the measurements were conducted. Finally, I am grateful to the "Gleb Wataghin" Institute of Physics (IFGW) at UNICAMP, where the Quantum Device Physics Laboratory (LFDQ) is located and consequently where much of this work took place.

Abstract

This Thesis explores methods to enhance the reproducibility of Josephson junctions, crucial elements in superconducting quantum technologies, when employing the Dolan technique in 30 kV e-beam processes. The study explores the influence of dose distribution along the bridge area on reproducibility, addressing challenges related to fabrication sensitivity. Experimental methods include E-beam lithography, with electron trajectory simulations shedding light on backscattered electron behavior. We describe the fabrication of various Josephson junction geometries and analyze the correlation between the success rates of different lithography patterns and the simulated distribution of backscattered electrons. Our findings demonstrate a success rate of up to 96.3% for the double resist 1-step low-energy e-beam lithography process. As a means of implementation strategy, we provided a geometric example that takes advantage of simulated stability regions to administer a controlled, uniform dose across the junction area, introducing novel features to overcome the difficulties associated with fabricating bridge-like structures.

Furthermore we also explore the fabrication of superconducting circuits through thin film deposition and subsequent etching, also known as "Top Down" method. The thin films studied were Nb and Al, they were tested with various reagents and for many applications, allowing us to define configuration which can best be used for superconducting circuit fabrication.

Furthermore we employ the techniques developed into a working Transmon device. We observe cavity dressed and bare mode, demonstrating an effective means of developing Josephson junction based superconducting quantum devices.

Chapter 1

Introduction

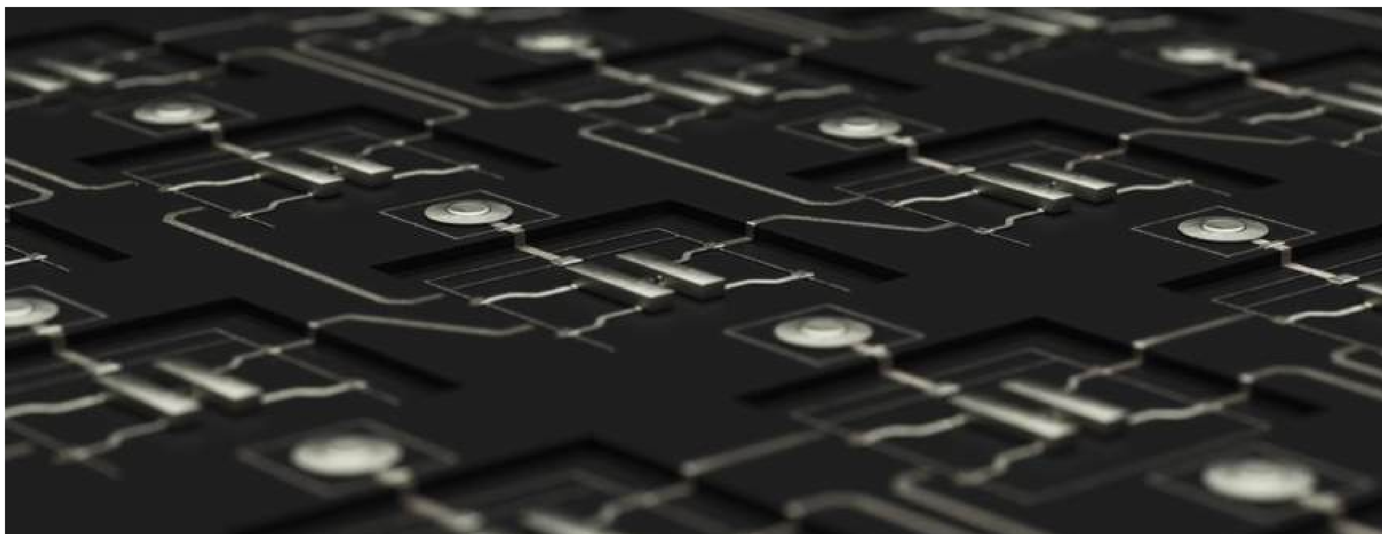

Figure 1.1: Artistic image of the Eagle QPU, adapted from [1].

The field of circuit quantum electrodynamics (cQED), as pioneered by Wallraff et al. [2], has ushered in a new era in condensed matter physics by demonstrating the strong coupling regime between an engineered artificial superconducting atom and a microwave cavity. This paradigm has granted us the unprecedented ability to engineer Hamiltonians and manipulate quantum states at the level of individual quanta. The development of these quantum systems has required significant advancements in cryogenic technology, leading to the construction of dilution refrigerators and RF electronics of unprecedented scale [3].

Despite not yet matching the robustness of natural quantum systems like ion traps, superconducting cQED has seen remarkable progress and numerous breakthroughs. For instance, in 2007, Majer et al. demonstrated the coherent interaction of two superconducting qubits via a cavity bus [4], paving the way for studies on increasing coherence and scalability [5, 6, 7, 8, 9, 10]. This progress has been further accelerated by recent developments in material science, fabrication techniques, and measurement methodologies.

In this thesis, we delve into the intricate processes involved in fabricating superconducting circuits and Josephson junctions, essential components for building superconducting quantum processors. We present novel approaches to e-beam lithography and multilayered superconducting circuit fabrication, highlighting their crucial role in achieving precise control and manipulation of qubits. Our work focuses on not only fabricating these components but also on developing robust measurement techniques to characterize and optimize qubit performance.

Through this research, we aim to contribute to the ongoing advancement of superconducting quantum processors, with a focus on enhancing coherence times, reducing error rates, and ultimately realizing scalable quantum computing architectures. By combining theoretical insights with practical experimental techniques, we strive to push the boundaries of what is possible in the field of quantum information processing.

1.1 Quantum Computing

Quantum mechanics, stemming from the foundational contributions of Max Planck, Albert Einstein, Niels Bohr, Werner Heisenberg, Erwin Schrödinger and others, has provided an extraordinarily precise framework for understanding the behavior of particles at the smallest scales.

The advent of the first quantum computers, pioneered by Google [11] and IBM [12], marked the dawn of the NISQ (Noisy Intermediate-Scale Quantum) era [13].

However, the significance of quantum computing to a physicist transcends its potential for solving complex algorithms. It offers a profound insight into the fundamental fabric of reality, bridging the realms of quantum mechanics and classical physics. Quantum mechanics, with its elusive nature and ethereal manifestations, captivates all who engage with it. Despite our mathematical understanding, there remain profound mysteries surrounding the "whys and hows" of quantum behavior. Since Davisson and Germer's groundbreaking electron diffraction experiment [14], confirming Louis de Broglie's 1924 prediction, researchers have relentlessly probed the nature of quantum mechanics. With advancements, we can now observe atoms transitioning from particle-like behavior to wave-like probabilistic distributions [15]. Demonstrating the ever increasing control and sophistication of quantum experiments.

The realization of quantum computing symbolizes humanity's mastery of quantum mechanics, harnessing its power to its fullest potential. It represents our ongoing quest to engineer systems that can exert precise control over quantum phenomena, enabling us to utilize a tool that has thus far remained beyond our reach. Quantum code can be seen as the most fundamental abstraction layer—the assembly language—of the universe, offering a glimpse into the intrinsic workings of the cosmos.

1.1.1 Josephson Junctions

Superconducting Quantum computing represents a frontier in contemporary physics and engineering, promising revolutionary advancements in computation [16, 17], communication [18, 19] and sensing [20, 21, 22]. Central to these technologies are Josephson junctions, critical components that enable the unique nonlinear properties of superconducting quantum circuits. Much progress has been made to improve functionality and quality of Josephson junctions and their applications [23, 24, 25, 26, 27, 28, 29, 30, 31, 32]. The fabrication process, however, remains exceedingly sensitive; even minor variations in junction area or

stochastic fluctuations in oxide formation can lead to inconsistencies in the overall oxide barrier, making the reproducibility of Josephson junctions a hindering factor in the performance and scalability of quantum devices [33]. Observations from fabricating hundreds of Josephson junctions led us to examine whether variations in the geometry of these junctions could significantly influence their reproducibility. Our research indicates backscattered electron distribution is essential to the proper formation of bridge like structures, thereby affecting the functionality and scalability of superconducting quantum devices. Defining such correlations benefit the reliability of Josephson junctions, particularly when utilizing low-energy 30 kV electron beam lithography (EBL).

Various groups have developed distinct strategies to enhance the reproducibility of Josephson junctions using low-energy 30kV electron beam lithography. These improvements primarily focus on variations in junction geometry and the employment of different resist stacks [34, 35], which have facilitated the fabrication of superconducting qubits with relaxation and coherence times ranging from hundreds of nanoseconds to tens of microseconds [36, 37, 38] for diverse applications. Despite these advancements, the underlying mechanisms contributing to the enhanced reproducibility of the junctions remain ambiguous. Claims have been made regarding the influence of surface tension in the resist [39, 40] the impact of resist thickness, and charge dissipation [23, 24]. To ensure the continued utility of low-energy electron beam lithography, comprehending the mechanisms affecting junction reproducibility and the role of geometry is crucial.

While the technical aspects of the 30 kV e-beam process are well-documented[35], bridge structure integrity is a known issue in fabricating Josephson Junctions with Dolan technique [41, 42, 43, 44]. Some groups claim robustness is compromised due to stress which occurs to PMMA layer depending on geometry used [39, 40]. Others deal with this by pre-exposing the bottom resist [34]. Our study addresses issue by focusing on enhancing fabrication reproducibility through the strategic selection of optimal geometries which correctly engineer the doses of backscattered electrons on the bridge area. Moreover, additional teams have recognized the issue we raise in this letter, they have attempted to apply complex commercially available 3D proximity effect correction (PEC)[45]. However even at 100kV where the backscattered electron distribution is nearly homogeneous they had to resort to manually modifying the dose in different parts of their exposure layout to achieve desired results. We do acknowledge that even the traditional PEC [46] improved our results, and PEC was in fact used for the fabrication of all junctions in our study, nevertheless it was not enough to yield satisfying results. In this paper, we present modifications to the fabrication methodology of Josephson junctions using 30 kV e-beam lithography, specifically employing the Dolan technique.

1.1.2 Objective

The objective of this thesis is to pave way for the fabrication of superconducting circuits applied to quantum computing. We aim to show methods for simulation of microwave cavities coupled to qubits. Top down fabrication of superconducting circuits followed by the overlay of Josephson Junctions using the bottom up method. Ending with the characterization of superconducting qubits. Enabling the flow from ideas to circuits to be reached through practical and reliable means. Essentially we look to develop robust techniques for fabricating superconducting circuits and Josephson junctions. Techniques which have a broad range of device applications such as superconducting qubits, Josephson Parametric Amplifiers [47] (JPA), Josephson Traveling Wave parametric amplifier[48] (JTWPA), Kinetic Inductance traveling wave parametric amplifier

[6] (KITWPA), photonic crystals and others. Ultimately, we will show the development of a few different superconducting circuit recipes, and proceed to in depth analysis of electron beam lithography applied to the fabrication of Josephson Junctions. Next we will show a path to design and simulate qubit cavity systems. We will conclude with the measurement of a device constructed with the methods described. Additionally we will share future prospects towards a four qubit QPU.

1.1.3 Structural Overview of this Thesis

This thesis spans a broad scope, guiding the reader from the design and conception of circuit quantum electrodynamics (cQED) experiments to the top-down fabrication of superconducting circuits. We then delve into an in-depth analysis of the bottom-up fabrication process of Josephson Junctions using the Dolan method, and conclude by measuring a qubit coupled to a 1D microwave cavity. The thesis emphasizes the experimental implementation of cQED experiments, detailing the fabrication of superconducting circuits using aluminum (Al), niobium (Nb), and multilayered films of these materials. We extensively investigate the Dolan method for fabricating Josephson junctions, which are critical components in superconducting qubits. Finally, we perform measurements on a qubit coupled to a superconducting cavity fabricated using the processes developed in this thesis.

Chapter 2 provides the theoretical background necessary to understand four key components: 1D microwave cavities, Josephson junctions, superconducting qubits, and the interaction of these elements in a coupled system. Chapter 3 outlines the methodology for simulating superconducting qubits, superconducting microwave cavities, and their coupled systems. Chapter 4 details the results from our fabrication procedures, beginning with the simulations of electron beam (e-beam) sample interactions to determine the necessary parameters for achieving high yield in a 30 kV e-beam process. We then present complementary results on Josephson junction fabrication and conclude the results section with the measurement of a qubit, showcasing our unique approach to fabricating Josephson junctions and trilayer superconducting circuits.

Chapter 5 concludes the thesis by offering perspectives on the development of a 4-qubit Quantum Processing Unit (QPU), highlighting the potential of the methods and insights gained in this work for advancing quantum technologies.

Chapter 2

Theoretical Foundation

We will commence the thesis by adopting a methodology akin to that of Dr. Dave Schuster[49], with a review of pertinent topics in microwave engineering[50]. However, our analysis will be more succinct, as this thesis concentrates on the experimental endeavors conducted in the clean room for fabricating these devices.

The microwave cavity serves as the circuit component through which we directly interact to indirectly probe the qubit state. We will commence by delineating the microwave cavity in its most abstract form, as an LCR circuit, and gradually escalate the complexity to encompass crucial findings of wave propagation theory, ultimately simplifying this model to a lossless transmission line.

Subsequently, we will delve into the Josephson equations, essential components for fabricating superconducting qubits. From there, we will broaden the discussion to encompass superconducting qubits and the elucidation of the qubit-cavity interaction mediated by the Jaynes-Cummings Hamiltonian. We will then elucidate how these concepts manifest as components in cavity quantum electrodynamics (CQED).

2.1 One-Dimensional Microwave Cavities

Quantum information is extracted from experiments through classical probing. The classical signals are reduced to a quantum regime before interacting with our sample. The physical devices used in our experiments are micro-metric thin film strip-lines, with parallel grounding. We will begin by describing the microwave cavity as an LCR oscillator lumped element circuit.

2.1.1 Lumped Element Electrical Harmonic Oscillator

In its simplest form the electromagnetic cavity can be reduced the lumped element parallel LCR circuit, Figure 2.1a. By using the first and second law of Kirchhoff, one finds the equation governing the charge on a capacitor in a parallel LCR oscillator. Having the currents summing up to zero and equal voltages, is given by:

$$\frac{d^2q}{dt^2} - \frac{1}{RC}\frac{dq}{dt} + \frac{q}{LC} = 0 \tag{2.1}$$

The solution to this differential equation is:

$$q(t) = q_0 e^{i(\omega_0 + i\frac{\kappa}{2})t+\phi} \tag{2.2}$$

This equation describes the charge oscillation with frequency $\omega_0 = 1/\sqrt{LC}$ and decay rate $\kappa = 2/RC$. It is useful from our perspective to describe the circuit in terms of its impedance $Z(\omega)$.

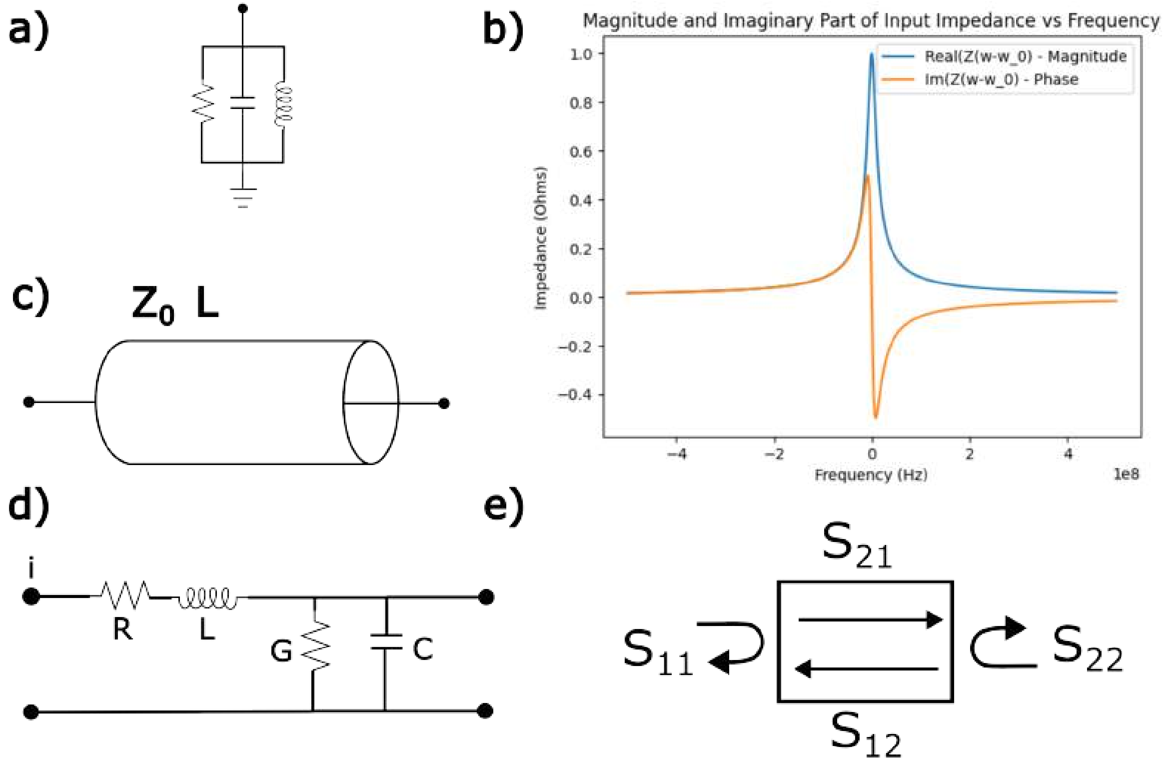

Figure 2.1: Diagrams for three levels of abstraction of microwave cavivity. a) Cavity modeled by lumped elements. b) Plot of the real and imaginary parts of the impedance of an oscillator. c) Cavity modeled as impedance per length. d) Cavity modeled as infinite series of resistors, inductors, conductance and capacitance lumped elements. e) S parameter model diagram.

The imaginary and real parts of equation $Z_{LC}(\omega) = \frac{1}{2j(\omega-\omega_0)C}$ is plotted on Figure 2.1, represents the impedance of a parallel LC circuit, where C is the capacitance and ω is the angular frequency. The characteristic impedance, Z_0, of a transmission line is defined as $Z_0 = R + j\omega L$, where R is the series resistance per unit length and L is the series inductance per unit length of both conductors. The propagation constant, γ, is given by $\gamma = \sqrt{(R + j\omega L)(G + j\omega C)}$, where G is the shunt conductance per unit length of the line. The equation $Z = \sqrt{\frac{R+j\omega L}{G+j\omega C}}$ describes the characteristic impedance of the transmission line, which is the ratio of voltage to current along the line.

In these equations Z is the impedance measured in ohms (Ω), R is the series resistance per unit length, measured in ohms per meter (Ω/m), L is the series inductance per unit length, measured in henries per

meter (H/m). G is the shunt conductance per unit length, measured in siemens per meter (S/m), C is the shunt capacitance per unit length, measured in farads per meter (F/m) and ω is the angular frequency of the signal, measured in radians per second (rad/s).

2.1.2 The Lossless Line

The above solution is for a general transmission line, including loss effects, and it was seen that the propagation constant and characteristic impedance were complex. In our case for superconductors, however, the loss can be neglected, resulting in a simplification of the results. Setting $R = G = 0$ gives the propagation constant as

$$\gamma = \alpha + j\beta = j\omega\sqrt{LC},$$

or

$$\beta = \omega\sqrt{LC},$$

$$\alpha = 0.$$

As expected for a lossless line, the attenuation constant α is zero. The characteristic impedance reduces to

$$Z_0 = \sqrt{\frac{L}{C}},$$

which is now a real number. The general solutions for voltage and current on a lossless transmission line can then be written as

$$V(z) = V_0^+ e^{-j\beta z} + V_0^- e^{j\beta z},$$

$$I(z) = \frac{V_0^+}{Z_0} e^{-j\beta z} - \frac{V_0^-}{Z_0} e^{j\beta z}.$$

The wavelength is

$$\lambda = \frac{2\pi}{\beta} = \frac{2\pi}{\omega\sqrt{LC}},$$

and the phase velocity is

$$v_p = \frac{\omega}{\beta} = \frac{1}{\sqrt{LC}}.$$

2.1.3 S-parameter

S-parameters describe the relationship between the incident and reflected waves at the ports of a two-port network. For a two-port network with ports 1 and 2, the S-parameter matrix is given by:

$$\begin{bmatrix} b_1 \\ b_2 \end{bmatrix} = \begin{bmatrix} S_{11} & S_{12} \\ S_{21} & S_{22} \end{bmatrix} \begin{bmatrix} a_1 \\ a_2 \end{bmatrix}$$

where: - a_1 and a_2 are the incident waves at ports 1 and 2 respectively, - b_1 and b_2 are the reflected waves at ports 1 and 2 respectively, and - S_{ij} are the S-parameters.

For a resonant transmission line, the S-parameters can be calculated based on the transmission line theory. At resonance, the transmission line behaves as a pure resistance and its input impedance becomes purely real. The S-parameters for a lossless transmission line terminated by an impedance Z_L at its end can be expressed as:

$$S_{11} = S_{22} = \frac{Z_L - Z_0}{Z_L + Z_0}$$

$$S_{12} = S_{21} = \frac{2Z_0}{Z_L + Z_0}$$

where: - Z_0 is the characteristic impedance of the transmission line, - Z_L is the load impedance.

At resonance, Z_L equals the characteristic impedance of the transmission line Z_0, resulting in S_{11} and S_{22} being 0, and S_{12} and S_{21} being 1. This indicates that all the incident power is absorbed by the transmission line and there is no reflection.

In complete abstraction our experiment is simplified to sending in microwave signals and measuring an output. RF (Radio Frequency) microwave measurements are used to characterize the behavior of microwave devices and circuits. Two key parameters in these measurements are S11 and S21, which are part of the S-parameter matrix used to describe the behavior of linear electrical networks. S11 represents the reflection coefficient, which measures how much of an incident signal is reflected back from a device or circuit. It is expressed as a complex number, with magnitude indicating the amount of reflection and phase indicating the phase shift of the reflected signal. S21 represents the transmission coefficient, which measures how much of an incident signal is transmitted through a device or circuit. Like S11, it is also expressed as a complex number, with magnitude indicating the amount of transmission and phase indicating the phase shift of the transmitted signal.

A microwave cavity is a resonant chamber used to contain and control electromagnetic fields at microwave frequencies. It is often used in microwave devices such as filters, oscillators, and amplifiers. When measuring a microwave cavity, S11 and S21 are used to characterize its behavior. To measure S11 of a microwave cavity, one would typically connect a network analyzer to the cavity and measure the reflection coefficient. This measurement helps determine how much power is reflected back from the cavity, which is important for understanding its resonant behavior and impedance matching. Measuring S21 on the other hand is useful for calculating the transmission coefficient. This measurement helps determine how much power is transmitted through the cavity, which is important for understanding its transmission properties and losses. By measuring S11 and S21 of a microwave cavity, one can characterize its resonant frequencies, quality factor (Q), and other important parameters that are crucial for designing and optimizing microwave devices and circuits.

2.2 Coupled Resonator

Resonators can be either $\lambda/4$ or $\lambda/2$. These types refer to the length of the resonator in relation to the wavelength of the signal it is designed to work with. A quarter-wavelength ($\lambda/4$) resonator has a length equal to one-fourth of the wavelength of the signal. It is typically used in applications where impedance transformation is required. This type of resonator is often employed in RF and microwave circuits as a

stub or filter. The open or shorted end of the $\lambda/4$ resonator can create specific boundary conditions that result in standing wave patterns, enabling certain frequencies to be selectively passed or blocked.

$\lambda/2$ resonators: A half-wavelength resonator is half the length of the wavelength of the signal. It tends to have nodes at both ends and an antinode at the center, creating a standing wave pattern. These resonators are commonly used in antennas, filters, and oscillators. They can support stronger resonances and are often preferred for applications requiring high quality factors (Q-factors).

In both cases, the physical size of the resonator and the properties of the materials used can significantly impact its performance. The design choice between $\lambda/2$ resonators depends on the specific requirements of the application, such as the desired frequency response, size constraints, and impedance characteristics. Resonators can be either $\lambda/4$ or $\lambda/2$. The resonant frequency of a waveguide resonator is determined by the wavelength of the standing wave that fits within the physical structure of the resonator. For a resonator with length l, the wavelength λ is related to the length by:

$$\lambda = 2l. \tag{2.3}$$

The speed of light in a medium with permittivity ϵ_{eff} is given by:

$$v = \frac{c}{\sqrt{\epsilon_{\text{eff}}}}. \tag{2.4}$$

The frequency f is then related to the speed of light and the wavelength by:

$$f = \frac{v}{\lambda}. \tag{2.5}$$

The design and analysis of these resonators rely heavily on the relationship between the resonant frequency and the physical parameters of the system. Substituting $\lambda = 2l$ and $v = \frac{c}{\sqrt{\epsilon_{\text{eff}}}}$, we obtain the frequency formula:

$$f = \frac{c}{\sqrt{\epsilon_{\text{eff}}}} \frac{1}{2l}, \tag{2.6}$$

Where f is the resonant frequency, ϵ_{eff} is the effective permittivity of the medium and l is the physical length of the resonator. The frequency formula for superconducting waveguide microwave resonators provides a fundamental understanding of the relationship between resonant frequency, physical length, and effective permittivity.

2.3 Josephson Equations

The behavior of a Josephson junction is governed by the Josephson effect, which describes the tunneling of Cooper pairs of electrons through the junction[51]. This effect leads to two fundamental equations that govern the dynamics of a Josephson junction: the Josephson relations. These equations describe the current-voltage characteristics of the junction and are essential for understanding its behavior.

The first Josephson equation relates the supercurrent I flowing through the junction to the phase difference δ across the junction:

$$I = I_c \sin(\delta).$$

where I_c is the critical current of the junction, which is the maximum current that can flow without inducing a voltage across the junction.

The second Josephson equation describes the time evolution of the phase difference δ across the junction:

$$\frac{d\delta}{dt} = \frac{2eV}{\hbar}.$$

where V is the voltage across the junction, e is the elementary charge, and $\hbar$ is the reduced Planck's constant.

These equations are crucial for understanding the behavior of Josephson junctions in various applications. They form the basis for superconducting quantum interference devices (SQUIDs), which are used for extremely sensitive measurements of magnetic fields, and for superconducting qubits, the building blocks of quantum computers.

2.3.1 Superconducting Quantum Interference Devices

Superconducting Quantum Interference Devices (SQUIDs) are highly sensitive devices used to measure magnetic fields. They consist of one or more Josephson junctions in a loop configuration. The magnetic flux Φ threading through the SQUID loop is quantized in units of the flux quantum Φ_0, where $\Phi_0 = \frac{h}{2e}$ is the magnetic flux quantum and h is the Planck constant.

$$\Phi = n\Phi_0,$$

where n is an integer. Furthermore we have that the Josephson current-phase relationship is given by the current I flowing through a SQUID loop is relation to the phase difference δ across the junctions by the Josephson junction equation for I_c. SQUIDs demonstrate a magnetic flux sensitivity able to measure a unitary quantum of flux. Additionally, magnetic flux is given by the derivative of the current with respect to the flux, known as the flux-to-voltage transfer function:

$$\frac{dI}{d\Phi} = \frac{2\pi I_c}{\Phi_0} \cos(\delta).$$

As for the voltage to flux relationship it is given by the voltage V across the SQUID in relation to the rate of change of the phase difference:

$$V = \frac{\hbar}{2e} \frac{d\delta}{dt}.$$

Combining these equations allows for the understanding and analysis of SQUID behavior, which is essential for their use in sensitive magnetic field measurements and various other applications in physics and technology.

2.4 Cavity Quantum Electrodynamics

Superconducting qubits are artificial atoms created from Josephson junctions. Essentially a Josephson Junction is a weak link between two superconductors, which allows for tunneling of a superconducting current. Therefore once a material which posses a weak link is cooled below its critical temperature T_c, it becomes an artificial atom. Superconducting qubits are usually 2-8 GHz, which means they have to be cooled down to tens of mK to be naturally found in their ground state. Temperature is used in quantum computing as means of always resetting qubits to their ground state, therefore offering means of control via microwave photons. By means of temperature and anharmonicity the qubit is kept between ground and the first excited state effectively making it a qubit. populates the electromagnetic cavity in which the qubit is embedded Josephson Junctions as can be shunted by a capacitor to form what is known as a charge qubit.

Josephson junctions serve as crucial components in superconducting electronics, particularly in quantum computing, enabling the mesoscopic manifestation of quantum properties through meticulously engineered devices. They allow for complete control over the Hamiltonian, thus facilitating the manipulation of quantum mechanics to an unprecedented degree. The unique nonlinear behavior of Josephson junctions has catalyzed the emergence of a new field of physics known as cavity quantum electrodynamics (cQED)[52, 2, 53]. This behavior, akin to that of a nonlinear quantum inductor, allows for the creation of systems that mimic nonlinear harmonic oscillators, leading to the development of a wide array of artificial atoms. Although these systems are inherently limited compared to real atoms, which can be isolated from the universe using cold traps for use in quantum computing, the ability to engineer hamiltonians has provided superconducting qubits with a distinct advantage over alternative methods.

It should not be understated that while much of the potential is still a promise, Josephson junctions already contribute on a fundamental basis to physics. They are instruments of incredible precision, used for metrology and sensing. For instance Josephson junctions are used as the (NIST) Volt standard[54], which is a testimony of their significance to science.

2.4.1 Superconducting Qubits

At the core of this new area of physics is the Josephson Junction, its anharmonic features enable a new frontier of physics. These artificial atoms are truly fascinating, they allow for a new type of artificial periodic table. Surely incredibly limited, it needs to be grown on a wafer, and fabrication techniques are limited as compared to for instance the semiconductor industry, which is now working on stacking nano wire transistors in a 3D matrix, very advanced techniques. For superconducting circuits arbitrary structures are difficult to build. And for now superconducting circuits are only spread linearly in 2D plane. Yet Josephson junctions still provide fertile ground for the birth of a promising new technology.

The Hamiltonian for the superconducting qubit is similar to that of a quantum harmonic oscillator (QHO). Here, we will begin with a linear LC resonant circuit and adapt it to describe superconducting qubits. We will start by defining the Lagrangian of the QHO then move on to the Hamiltonian. By arbitrarily associating the electrical energy with the "kinetic energy" and the magnetic energy with the "potential energy" of the oscillator. The instantaneous, time dependent energy in each element is derived from its current and voltage.

We will start with the classical harmonic oscillator shown in Figure 2.2. The cycle begins when the capacitor is fully charged and no energy is flowing. We have that the "kinetic energy" is $E = \frac{1}{2}CV^2$. And the "potential energy" will correspond to the energy stored in the magnetic field around the coil $E = \frac{LI^2}{2}$.

$$E(t) = \int_{-\infty}^{t} V(t')I(t')dt' \tag{2.7}$$

$$\Phi(t) = \int_{-\infty}^{t} V(t')dt' \tag{2.8}$$

Using $V = LdI/dt$, $I = CdV/dt$ and the integration by parts formula $dx = d(uv)/dx = udv/dx + vdu/dx$. We obtain the Lagrangian seen in Equation 2.9

$$L = T_c - U_L = \frac{1}{2}C\dot{\Phi}^2 - \frac{1}{2L}\Phi^2 \tag{2.9}$$

$$Q = \frac{\partial L}{\partial \dot{\Phi}} = C\dot{\Phi} \tag{2.10}$$

The Hamiltonian of the system is now defined as

$$H = Q\dot{\Phi} - L = \frac{Q^2}{2C} + \frac{\Phi^2}{2L} \equiv \frac{1}{2}CV^2 + \frac{LI^2}{2} \tag{2.11}$$

Notice that this Hamiltonian is analogous to the mechanical harmonic oscillator expressed in momentum p and position x. By making $m = C$ and $\omega = 1/\sqrt{LC}$, we recover $H = p^2/2m + m\omega^2 x^2/2$. In order to go from a classical description to a quantum mechanical one the Poisson brackets must be verified.

$$\left\{ f \ , \ g \right\} = \frac{\delta f}{\delta \Phi}\frac{\delta g}{\delta Q} - \frac{\delta g}{\delta \Phi}\frac{\delta f}{\delta Q} \tag{2.12}$$

$$\left\{ Q \ , \ \Phi \right\} = \frac{\delta g}{\delta \Phi}\frac{\delta f}{\delta Q} - \frac{\delta f}{\delta \Phi}\frac{\delta g}{\delta Q} = 1 - 0 = 1 \tag{2.13}$$

The quantum operators also satisfy the commutation relationship.

$$[\hat{\phi}, \hat{Q}] = \hat{\phi}\hat{Q} - \hat{Q}\hat{\phi} = i\hbar \tag{2.14}$$

Therefore we can make the canonical transformation and arrive at the Hamiltonian of the quantum harmonic oscillator by defining $\phi \equiv 2\pi\Phi/\phi_0$ and $n = Q/2e$. To simplify the expression we have the charging energy $E_C = e^2/(2C)$ and the Josephson energy $E_J = (\Phi_0/2\pi)^2/L$.

$$H = E_C n^2 + \frac{1}{2}E_J\phi^2 \tag{2.15}$$

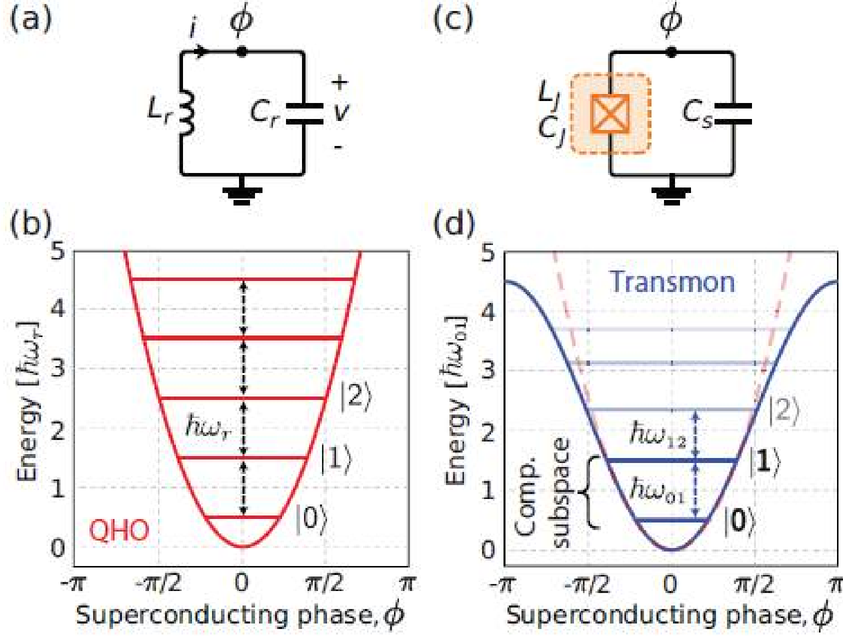

Figure 2.2: On the left we have a quantum harmonic oscillator with fixed capacitance C and Inductance L, on the right is the anharmonic oscillator produced by the nonlinear Josephson Junction in the circuit (box with x inside).

Quantum mechanically, the solution to $H\left|\psi(t)\right\rangle$ yields a discrete infinite eingenvector series $\left|k\right\rangle = \{\left|0\right\rangle, \left|1\right\rangle, \left|2\right\rangle, ...\}$ The eigenenergies are all evenly spaced $E_{k+1} - E_k = \hbar\omega_r$ where $\omega_r = \sqrt{8E_L E_C}/\hbar = 1/\sqrt{LC}$. Taking this solution into consideration a second quantization can be made.

$$H = \hbar\omega_r\left(a^\dagger a + \frac{1}{2}\right) \tag{2.16}$$

The original number and phase operators can be expressed as $n = [E_L/(32E_C)]^{1/4} \times i(\hat{a} - \hat{a}^\dagger)$ and $\phi = (2E_C/E_L)^{1/4} \times (\hat{a} + \hat{a}^\dagger)$.

These evenly spaced energy levels makes them indistinguishable as seen on the left side of Figure 2.2. The physical quantity that solves this problem is nonlinear Josephson inductance. Named this way after Brian Josephson, however the non linearity comes from the fact that superconducting particles do not interact with the atomic lattice and therefore have significant kinetic inductance. In theory the larger anharmonicity the better, but increasing anharmonicity also increases sources of noise [55]. On the right side of Figure 2.2, we see the energy potential of the transmon qubit, which gives rise to distinct energy levels. This is achieved by introducing the nonlinear phase dependent Josephson inductance. The Hamiltonian becomes:

$$H = E_C n^2 + E_J\, cos(\phi). \tag{2.17}$$

Here $E_J = I_c \Phi_0 / 2\pi$ is the Josephson energy, where Ic is the critical current, and $E_C = e^2/(2C_s + C_J)$, which means E_C is a combination of the junction capacitance C_J and shunt capacitance C_S.

The E_C/E_J ratio plays an important role in noise reduction, there is noise associated with the charging of the qubit. In the transmon regime, $E_J >> E_C$ thus the noise attributed to E_C reduces exponentially. However the anharmonicity also decreases as E_J is increased but only linearly.

The charge qubit, specifically the transmon qubit, is a type of superconducting qubit that is capacitively shunted to suppress charge noise. It operates in a regime where the energy levels are anharmonic, allowing for longer coherence times compared to other types of charge qubits. Transmons are widely used in quantum computing due to their relative insensitivity to charge noise[56].

2.4.2 Atom-Cavity Coupling

A fundamental system for investigating the interaction between matter and light involves a two-level atom coupled to a cavity, where the cavity's excitations correspond to photons [49, 55]. This system's coherent behavior is governed by the Jaynes-Cummings Hamiltonian:

$$H_{JC} = \omega_r (a^\dagger a + \frac{1}{2}) + \omega_a \frac{\sigma_z}{2} + g(a^\dagger \sigma^- + a\sigma^+),$$

where the terms represent the energy of the electromagnetic field, the atom's energy as a spin-1/2 system, and the dipole interaction, respectively. Besides atoms and photons, this Hamiltonian can also describe other systems such as circuits, quantum dots, and nanomechanical systems.

Decoherence processes, including the photon decay rate (κ), atom decay rate ($\gamma_\perp$), and the photon leaving the cavity rate ($1/T$), influence the system's dynamics. The interplay between coherent and incoherent processes is particularly significant when the atom resonates with the cavity, enabling free energy exchange between the two systems. The system reaches the strong coupling limit of cavity quantum electrodynamics (QED) when the interaction strength exceeds the decoherence rates ($g > \kappa, \gamma_\perp, 1/T$).

Dispersive Limit

In the resonant limit ($\omega_a - \omega_r \approx g$), the atom and photon can exchange energy, leading to a strongly coupled system. However, in many cases, it is preferable to operate in a dispersive regime, where no actual photons are absorbed by the atom. This can be achieved by detuning the atom and cavity by $\Delta = \omega_a - \omega_r$ such that $g \ll \Delta$. In this dispersive limit, the dipole interaction's effect can be modeled using perturbation theory. Expanding to second order in g/Δ yields the approximate Hamiltonian:

$$H \approx \omega_r a^\dagger a + \frac{g^2}{\Delta} \sigma_z a^\dagger a + \frac{1}{2} + \frac{\omega_a \sigma_z}{2}$$

The dispersive shift term (g^2/Δ) describes the interaction's effect without changing the photon number or the atom's state but alters their energies. This shift, dependent on the atom's state, can be utilized for a Quantum Non-Demolition (QND) measurement of the atom's state.

The interaction can also be expressed to emphasize its effect on the atom:

$$H \approx \omega_r a^\dagger a + \frac{1}{2} + \frac{\omega_a}{2} + \frac{2g^2}{\Delta} a^\dagger a + \frac{g^2}{\Delta}\sigma_z$$

This form shows that the interaction gives the atom a "light" shift, comprising a photon number-dependent "Stark" shift ($2ng^2/\Delta$) and a vacuum noise-induced "Lamb" shift (g^2/Δ). This atom-photon symmetry in the dispersive interaction is a manifestation of the Heisenberg uncertainty principle's required backaction. It implies that photons used for measuring the atom's state will also modify its frequency, allowing for a QND measurement on the photon number.

The Jaynes-Cummings Hamiltonian, connecting states with the same number of excitations, allows for exact diagonalization to calculate energy levels and eigenstates. In the dispersive coupling regime ($\Delta > 0$), the $|\pm\rangle$ states resemble qubit states but with a photon component. This overlap implies that the qubit excitation can exist as a photon in the cavity, enabling the creation of an "entanglement" bus with multiple qubits strongly coupled to the same cavity. This non-local gate effect could occur even when the qubits are centimeters apart. The photonic aspect of the qubit also introduces a new decay channel, where the qubit can decay as a photon emitted from the cavity.

$$\gamma_\kappa \approx \left(\frac{g}{\Delta}\right)^2 \kappa \quad \text{and} \quad \kappa_\gamma \approx \left(\frac{g}{\Delta}\right)^2 \gamma$$

For instance, an atom coupled to an infinite transmission line would radiatively decay at a rate g^2/ω. In contrast, inside a cavity, the atom's decay rate is $g^2\kappa/\Delta$. This discussion sets the stage for a more modular view of the circuit components.

2.5 Quantum Processing Unit

A superconducting quantum processing unit (QPU) represents a cutting-edge advancement in the field of quantum computing. Essentially it consists of microwave waveguides to manipulate and control the superconducting qubits, a set of control electronics and microwave pulses are employed. Magnetic fields are also employed for tuning the energy levels of the qubits, enabling precise control over their states. Moreover, microwave resonators and cavity modes are integrated into the system to facilitate the transfer of information between qubits. The ability to apply coherent microwave pulses and control the system's parameters is crucial for executing quantum gates and maintaining the delicate superposition states of qubits.

The superconducting QPU is believed to be suitable for scaling the number of qubits which can be entangled. Quantum gates, analogous to classical logic gates, are applied to the qubits to perform quantum computations. The entanglement of qubits enables the creation of quantum circuits that can execute complex algorithms with unique properties inaccessible to classical computers. Which has been shown to be useful for certain problems, such as factoring, algorithm elaborated by Peter Shor [57] which takes advantage of quantum mechanics interference properties to have the time which takes to factor a number

increase only linearly with time. As opposed to classical computers which for this same task the time increases exponentially. Simulating quantum systems is another task which classical computer struggles. However QPUs are currently in the NISQ era where quantum error correction protocols, often involving additional qubits known as ancilla qubits, are implemented to mitigate the impact of decoherence and errors, in an attempt to enhance the reliability of the computations performed.

While QPU are in the embryonic stage there is much room for growth. With advancements in materials science, cryogenics, and control electronics, researchers continue to refine and scale up superconducting QPUs, bringing the promise of quantum advantage closer to realization. The intricate interplay of Josephson junctions, control mechanisms, and quantum gates forms the foundation of this remarkable technology. As the field progresses, ongoing research and development will likely push the boundaries of superconducting qubits, making quantum computing a transformative force in computational capabilities and scientific discovery.

2.5.1 Architecture

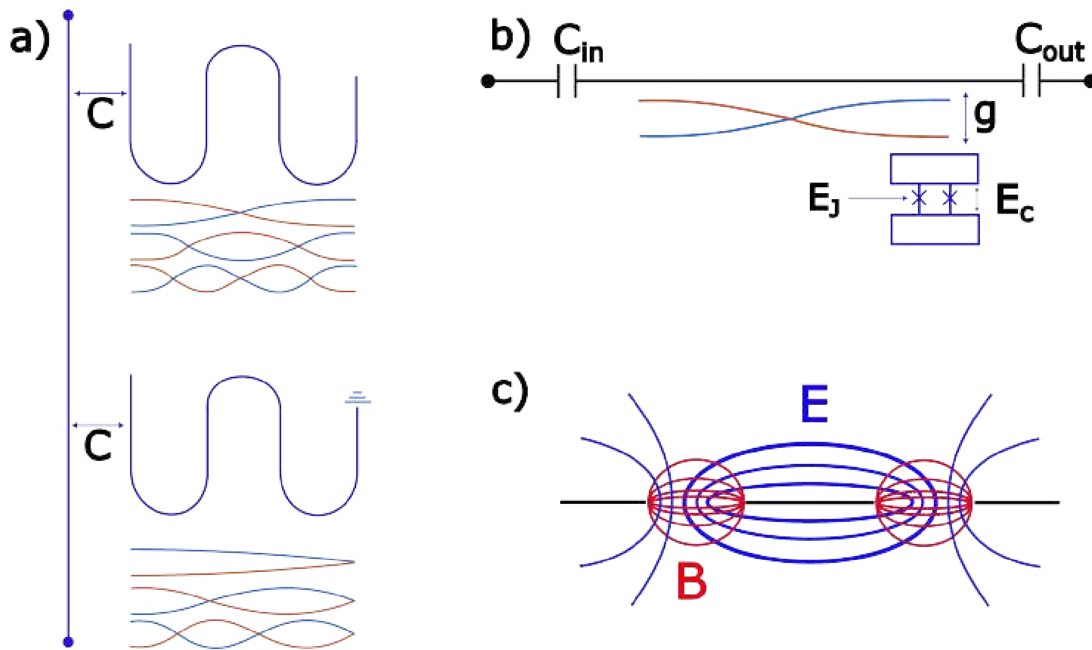

Figure 2.3: a) Two multiplexed waveguides coupled to a feed line, the top one is $\lambda/2$ while the bottom one is a $\lambda/4$ waveguide due to one end being shorted. The first four harmonics are displayed for each variant. The capacitors are referred to as hang capacitors. To the left hanger type capacitor, to the right interdigitaded capacitor. b) Waveguide capacitively coupled on both sides, transmon diagram is placed near indicating interaction with standing waves generated by the oscillator.

Cavity Quantum Electrodynamics (cQED) devices typically consist of various components such as couplers, waveguides, fluxlines, and superconducting qubits. One dimensional microwave cavities, can be categorized as quarter wave resonators or half wave resonators. Quarter wave resonators are grounded on one end,

resulting cavity having a node at one end and antinode in the other. A diagram of a quarter wave resonator is shown Figure 2.3 a (bottom). Half-wave cavities on the other hand, result in a fixed node in the middle and antinodes at both ends and can be coupled on both ends which enable a photon to interact in the cavity and be detected on the other side Figure 2.3 b.

Multiplexing is using one feed line to measure more than one microwave cavity. As seen on Figure 2.3 a, both quarter and half wave resonators can be coupled to a single feed line. This process is useful because it reduces the cabling needed. Allowing many microwave cavities to be probed with one measurement line [58]. This allows signals to be sent through a wire in the circuit, which is coupled to quarter wave resonators, with each resonator being coupled to its respective qubit.

In addition to the aforementioned components, cQED devices may also include other important elements such as cryogenic amplifiers for signal amplification, circulators for routing microwave signals, and cryogenic isolators for protecting qubits from reflected microwave signals. These components play crucial roles in the overall performance and functionality of cQED devices, ensuring their optimal operation.

Coaxmon qubits are a type of superconducting qubit that utilize a coaxial transmission line resonator for readout and manipulation. This design offers advantages such as improved coherence times and scalability. Coaxmon qubits have shown promise for quantum computing applications [59].

Unimon qubits are a type of superconducting qubit that combines features of both charge and flux qubits. They utilize a single Josephson junction and a loop with an inductance to create a hybrid qubit design. Unimon qubits offer advantages in terms of tunability and coherence times, making them a promising candidate for quantum computing applications [60].

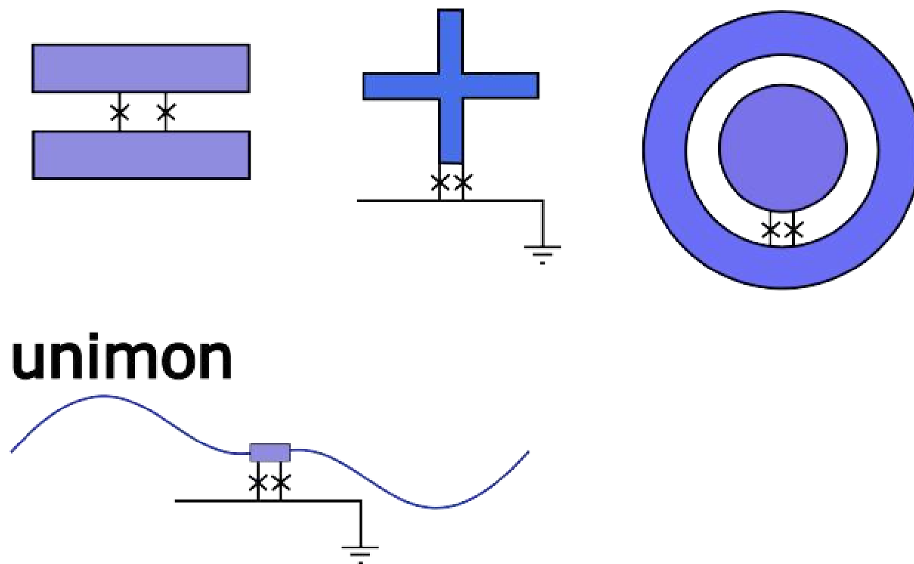

Figure 2.4: Variations of the transmon qubit: transmon, X transmon, concentric transmon, unimon qubits. The x indicates position of Josephson junctions.

On Chip Components

Qubits are the fundamental building blocks of superconducting QPUs, representing the quantum bits that encode and process quantum information. Superconducting qubits have been the technology of choice by major players [11, 61, 62]. Various types of superconducting qubits, including transmon qubits, flux qubits, and phase qubits, have been developed and integrated into QPU architectures. The coherent manipulation and control of qubits, facilitated by on-chip components such as waveguides, capacitors, flux lines, and feed lines, are essential for realizing scalable and fault-tolerant quantum computation.

Central to the functionality of superconducting QPUs are on-chip components that enable the manipulation and control of quantum information. This section focuses on the key on-chip components including waveguides, capacitors, flux lines, feed lines, and qubits, elucidating their roles and importance in the operation of superconducting QPUs.

Waveguides serve as conduits for guiding microwave signals, which are utilized for controlling and readout operations in superconducting QPUs. These waveguides are typically fabricated using superconducting materials such as niobium or aluminum to minimize losses and maintain coherence of quantum states. By carefully engineering the dimensions and geometries of waveguides, efficient transmission and manipulation of microwave signals can be achieved, enabling coherent qubit operations.

Capacitors play a crucial role in superconducting QPUs by effecting controling the quality factor of the cavity. The quality factor must be carefully tuned to allow for high fidelity readout while having high enough Q, for the photon to stay in the cavity long enough for qubit and cavity to interact.

Flux lines, also known as magnetic flux lines, are used to control the magnetic flux through superconducting qubits, thereby modulating their energy levels and enabling manipulation of qubit states. By applying magnetic flux pulses through these on-chip flux lines, qubits can be initialized, manipulated, and measured with high fidelity. The precise control of flux lines is essential for implementing high-fidelity quantum gates and mitigating errors in quantum computations.

Feed lines are employed to deliver microwave signals to superconducting qubits for coherent manipulation and readout operations. These feed lines are designed to efficiently couple microwave photons to the qubits, ensuring high-fidelity qubit control and measurement. Moreover, feed lines are utilized for implementing microwave pulse shaping techniques, enabling precise control over qubit operations and enhancing the performance of superconducting QPUs.

Flux and feed lines are designed to have lower capacitance to the qubit then the readout cavity. In this way stimulation sginals come in, however the interaction is not strong enough for it to be a significant means of decoherence or relaxation.

On-chip components play a critical role in the operation of superconducting QPUs by enabling the manipulation, control, and readout of quantum information encoded in qubits. Waveguides, capacitors, flux lines, feed lines, and qubits collectively form the building blocks of superconducting QPU architectures, the interaction between these components can be described through the capacitance between them[63]. Which essentially translates to a coupling strength among components, and careful consideration is necessary to build QPUs.

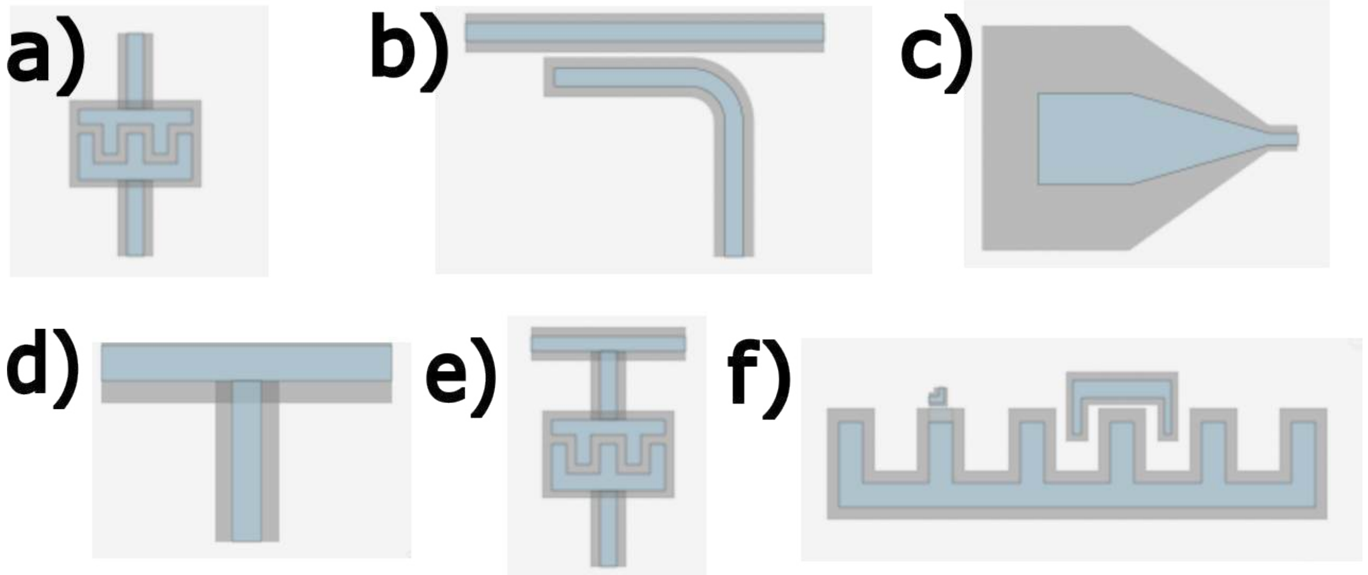

Figure 2.5: Qistkit Metal components, they can be used to put together CQED circuits. Components include: a) capacitors , b) hanger coupler, c) wirebond pads, d) line tee, e) line tee couplers, f) qubits and others.

Waveguides used for quantum computing usually take two forms, transmission and hanger mode. Transmission waveguides are coupled on both ends, hanger modes only have one coupling point to the feed port. In both cases, coupling is mediated capacitively. Optimal coupling can be described at midpoint between loosing too many inserted photons in a very high Q cavity and receiving every photon being sent due to an overcoupled low Q cavity. The optimal regime is known as critical coupling, to the photon staying the cavity and leaving is at equal probabilities [64].

The design of these circuits can be done using open-source software such as Qiskit Metal which will be discussed further on Section 3.1.2. On figure 2.5 several ready to be used circuit elements are ready to be put together to build complex circuits.

Chapter 3

Simulation

3.1 Simulation Methodology

To perform electromagnetic simulations of high-frequency capacitance and resonance using ANSYS, the process typically begins with creating the 3D geometry of the capacitor or resonant structure using ANSYS Design Modeler or another CAD software. This geometry should be detailed and accurate to ensure the simulation captures the desired effects. Next, a mesh is generated for the geometry using ANSYS Meshing, with a density sufficient to accurately capture high-frequency effects. Material properties are then assigned to the components of the model, such as dielectric properties for capacitors or conductor properties for resonant structures.

Boundary conditions are defined for the simulation, including voltage or charge boundary conditions for capacitors and excitation conditions for resonant structures. The ANSYS HFSS solver is used for high-frequency electromagnetic simulations, and the solver settings are configured for the desired accuracy and performance. The simulation is run, and the progress is monitored, with complex geometries and high-frequency simulations often requiring significant computational resources and time. After the simulation is complete, the results are analyzed using ANSYS Post-Processing tools. This analysis includes visualizing field distributions, capacitance values, resonance frequencies, and other relevant quantities. If necessary, optimization studies can be performed to optimize the design for desired performance metrics. Finally, the simulation results are validated by comparing them with experimental data or analytical solutions, and adjustments are made to the simulation setup as needed to improve agreement.

Superconducting transmission lines are the means of controlling these superconducting circuits containing Josephson junctions. For this, the software ANSYS was chosen due to its pratical integration with open source tool Qiskit Metal from IBM as the tool for achieving the objective. In Section 3.1 there is a brief discussion about Numerical Analysis via The Finite Element Method. An attempt here is made to show that the Radio Frequency Module (Frequency Domain) can be used as a tool to aid the production of qubits. The Radio Frequency Module will be looked at in Section 3.2. Once a transmission line is created and mapped, the goal then became to study how can the interactions with qubits could be modeled. The basic interaction is of the vacuum state energy produced by the resonator and the qubit dipole moment.

3.1.1 Circuit Analysis and Simulation

FEM is a the mathematical technique used to solve differential equations. It works by dividing a certain geometry in discrete small partitions which are easier to solve. Then an overall solution is found if the solver can minimize an associated error function. ANSYS solves a particular set of Maxwell equations in the frequency domain. Consider the following Maxwell's equations:

$$\begin{aligned} \frac{\partial \mathcal{D}}{\partial t} &= \nabla \times \vec{H}, && \text{(Faraday's Law)} \\ \frac{\partial \mathcal{B}}{\partial t} &= -\nabla \times \vec{E}, && \text{(Ampère's Law)} \\ \nabla \cdot \mathcal{B} &= 0, && \text{(Gauss' Law)} \\ \nabla \cdot \mathcal{D} &= 0. && \text{(Colomb's Law)} \end{aligned} \tag{3.1}$$

Taking Maxwell's equations and considering harmonic fields of the type: $E = E_0\ e^{iwt-k\vec{r}}$ and $H = H_0\ e^{iwt-k\vec{r}}$

$$\begin{aligned} \vec{J} + i\omega\vec{D} &= \nabla \times \vec{H}, && \text{(Faraday's Law)} \\ -i\omega\vec{B} &= \nabla \times \vec{E}, && \text{(Ampère's Law)} \end{aligned} \tag{3.2}$$

Using : $\vec{J} = \sigma\vec{E}$, $\vec{B} = \mu\vec{H}$ and $\vec{D} = \epsilon\vec{E}$. Ampère's Law and Faraday's Law come out to:

$$\begin{aligned} \sigma\vec{E} + i\omega\epsilon\vec{E} &= \nabla \times \vec{H}, && \text{(Faraday's Law)} \\ \vec{H} &= \frac{\nabla \times \vec{E}}{-i\omega\mu}, && \text{(Ampère's Law)} \end{aligned} \tag{3.3}$$

Now combining these two equations

$$\sigma\vec{E} + i\omega\epsilon_r\vec{E} = \nabla \times \frac{\nabla \times \vec{E}}{-i\omega\mu_r} \tag{3.4}$$

Rearranging the variables

$$\vec{\nabla} \times \mu_r^{-1}(\vec{\nabla} \times \vec{E}) - k_0^2(\epsilon_r - \frac{i\sigma}{\omega\epsilon_0})\vec{E} = \vec{0} \tag{3.5}$$

This equation yields the Electric field $\vec{E}$ for a frequency ω applied to the system. Each domain needs to be attributed a material, whose properties of interest are the material's relative permittivity ϵ_r, permeability μ_r and conductivity σ.

Perfect Electric Conductor - PEC The PEC boundary condition was applied to simulate the properties of superconducting surfaces. This condition is applied via $\vec{n} \times \vec{E} = \vec{0}$. This equation sets the tangential vector of the Electric field to zero, confining the electric field instead of scattering it. In other words this represents a lossless surface which is suitable for representing superconductors.

3.1.2 Qiskit Metal

Qiskit Metal is a powerful tool for computer aided design applied to superconducting circuits, because it allows for modifying and rendering into analysis software seamlessly. While this could be done by hand, re-editing CAD models is a tedious task. While it is possible to estimate dimensions on simple calculations. The actual values for capacitance depend on the model's specific design. For instance, it relatively straight forward to calculate the capacitance between qubit and cavity, when approximating the cavity to an infinite wire, however waveguides are usually winded in order to fit within the circuits, therefore this approximations break down and Finite Elements Simulation Methods are necessary. Clearly the necessity to simulate indicates reiterations will be made to the circuit, this can be done in an automated manner using Qiskit Metal. Essentially making it possible to create and optimize circuits in a very fast pace.

There are some notable opensource python library for cQED design and simulation, in my opinion Qiskit Metal is the most well developed with the biggest supporting community. All of the circuits which require microwave cavities were designed using Qiskit Metal. We will now briefly describe how the quantization takes place. Qiskit Metal, can simulate and quantify classical circuits in three different ways. The methods are lumped oscillator model, energy participation ratio, and scattering model using impedance. Here we will describe the two mains methods used in this Thesis.

HFSS ansys renderer Qiskit Metal comes equipped with a convenient rendering feature that simplifies the process of simulating and fine-tuning. With one line of code the entire circuit is rendered into ANSYS HFSS, simulation parameters are loaded and simulation begins. This can also be put in a loop to solve for multiple configurations at once.

Lumped Oscilator Model Analysis

[65] The paper describes a method for analyzing and designing superconducting quantum processors, which are critical for quantum information processing. These processors use macroscopic, lithographically-defined devices that can be configured for various quantum operations. However, designing these devices is challenging due to parameter variability, complex design space, and the difficulty of engineering their

non-linear interactions. The method proposed in the paper aims to address these challenges by providing a precise, modular approach that operates at the physical-device level.

The method involves partitioning the physical layout of the quantum device into disjoint cells, which are physical blocks of the device that can be independently simulated to extract their electromagnetic parameters. The effective circuit of the device is also partitioned into non-dynamical coupler elements and nodes, as well as subsystem building blocks. These subsystems are selected based on their parameter flexibility and ability to constitute a well-understood, basic system in isolation. The larger device model is then stitched together from the results of the cell simulations and reduced according to the subsystem partitions, accounting for dressing of the systems and their interactions due to coupling structures.

The method is applied to large-scale superconducting quantum processors with transmon qubits and co-planar wave guide (CPW) structures. Experimental tests show significant renormalizations of subsystem Hamiltonian parameters due to coupling dressing and other effects. The method provides a factor of two improvement in experimental agreement compared to standard approximations. It is applicable to a broad class of quantum processors and has been automated in the open-source project Qiskit Metal for quantum device design.

3.1.3 Qutip

Qutip [66, 67] is a comprehensive Python library designed for simulating the dynamics of open quantum systems. It is particularly well-suited for applications in quantum mechanics, quantum optics, quantum information theory, and quantum control. At the core of Qutip are its quantum objects, represented by 'Qobj' instances, which encapsulate quantum states and operators. These objects enable a wide range of quantum operations and calculations to be performed efficiently within the library.

One of the key capabilities of Qutip is its ability to simulate the time evolution of quantum systems under various Hamiltonians. This includes the simulation of systems with time-dependent Hamiltonians, allowing for the modeling of complex quantum dynamics. Additionally, Qutip supports the simulation of quantum measurements. Furthermore, Qutip provides tools for simulating quantum gates, which are fundamental building blocks for quantum algorithms. This enables researchers and practitioners to explore quantum teleportation, quantum error correction, and other quantum information processing tasks. Moreover, Qutip includes functionality for simulating quantum optics experiments, such as cavity quantum electrodynamics (QED) and photon counting, making it a versatile tool for researchers in quantum optics. This includes visualization methods such as Bloch sphere representations for qubits .

Chapter 4

Results

4.1 Nanofabrication Procedures

This section will discuss the fabrication steps for Josephson junctions and superconducting circuits. These being lithography, thin film deposition and etching. The E-beam Lithography, Optical Lithography etching and imaging were done within the LABNANO laboratory complex within CBPF. As for the AJA deposition system used in this study, it is a part of the LFDQ laboratory, located in the Glebb Wataghin Physics Institute. Equipment used displayed on Figures 4.1 and 4.13.

4.1.1 Physical Vapor Deposition

Physical vapor deposition (PVD) techniques play a crucial role in the fabrication of thin films with precise thickness, composition, and properties. These techniques involve the physical transport of material from a source to a substrate under vacuum or low-pressure conditions, without involving a chemical reaction. PVD methods are widely used in industries such as semiconductor manufacturing, optical coatings, and decorative coatings due to their ability to produce high-quality thin films with a wide range of applications.

One of the most common PVD techniques is evaporation, where material is heated in a vacuum chamber until it evaporates and then condenses onto the substrate. Evaporation can be carried out using electron beam heating, as is in our case and this method often used for depositing metals and dielectric materials. Sputtering is another widely used PVD technique, where ions bombard a target material, causing atoms to be ejected and deposited onto the substrate. Sputtering is versatile and can be used for depositing metals, alloys, and compound materials.

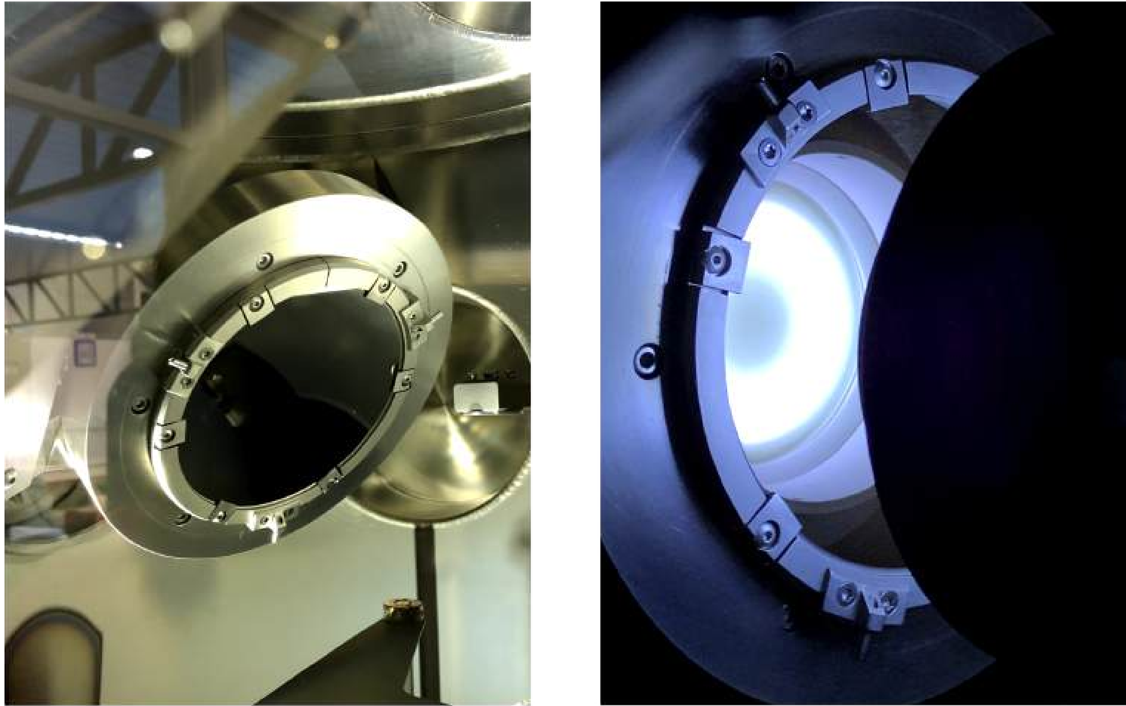

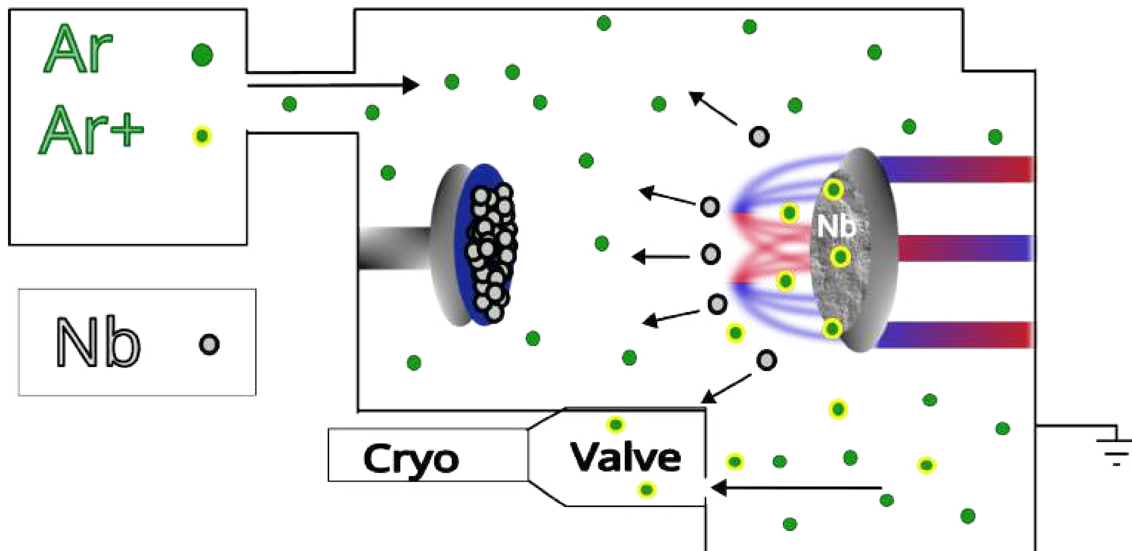

Figure 4.2: Top left: Argon Magnetron Sputtering, Wafer mounted ready for thin film deposition. Top right: Magnetron sputtering of Nb film onto wafer, 2 cm distance from target to wafer and the sample is spinning through the entire process to ensure an even deposition. Bottom: Magnetron Sputtering diagram showing magnetic field lines trapping nearby argon atoms, which become ionized and trapped by magnetic fields near the sputtering target. Ions are repeatedly bombarded against the target metal, this case Nb. Atoms which are dislodged make their way to the target, the pressure in the deposition chamber is raised to 3 mTorr, in order to have enough argon to keep the plasma on.

Magnetron sputtering is a widely employed physical vapor deposition (PVD) technique utilized for depositing thin films in a controlled manner. The process involves a vacuum chamber containing a target material (the material to be deposited) and a substrate (the surface onto which the material will be deposited). Inside the chamber, a magnetic field is applied to create a plasma discharge. This plasma consists of positively charged ions (Ar+) and free electrons. The magnetic field causes the electrons to spiral along the magnetic field lines, increasing their path length and, consequently, their energy. These high-energy electrons collide with gas atoms, creating more ions. The positively charged ions are then accelerated towards the negatively charged target material (an anode) due to the electric field created by a separate cathode.

When these ions strike the target surface, they dislodge atoms from the target through a process called sputtering. These sputtered atoms are then deposited onto the substrate, where they condense to form a thin film. The process is highly controlled, allowing for precise control over the film's thickness, composition, and structure. Magnetron sputtering is preferred for its ability to deposit a wide range of materials, including metals, oxides, and nitrides, with high purity and uniformity.

This process is done in High Vacuum, the target is usually placed no further than 20 cm. However its inefficient for long distances as the mean free path is not high enough. This implies deposition will be isotropic, which is fine for circuit fabrication but incompatible with double angle shadow deposition. In our fabriaction process the first step in superconducting circuit fabrication is depositing a 100 nm Nb coating. This is done at pressure of 3 mTorr, and flux of Argon gas at 100 sccm.

E-beam Physical Vapor Deposition

Electron beam PVD is a high-energy, high-vacuum deposition technique used to deposit thin films with excellent purity and uniformity. In e-beam PVD, a material (usually a metal or semiconductor) is heated in a vacuum chamber to create a vapor. An electron beam gun is used to generate a focused beam of high-energy electrons that are directed at the heated material, causing it to evaporate. The evaporated material then condenses on a substrate, forming a thin film. The process is highly controllable, allowing for precise control over the film's thickness and composition. One of the key advantages of e-beam PVD is its ability to deposit materials with high melting points, such as refractory metals, which are difficult to deposit using other techniques. Additionally, the high vacuum environment ensures that the deposited films are free from contaminants, resulting in high-purity films. Our deposition systems have the sample placed a meter away from the allowing for anisotropic deposition.

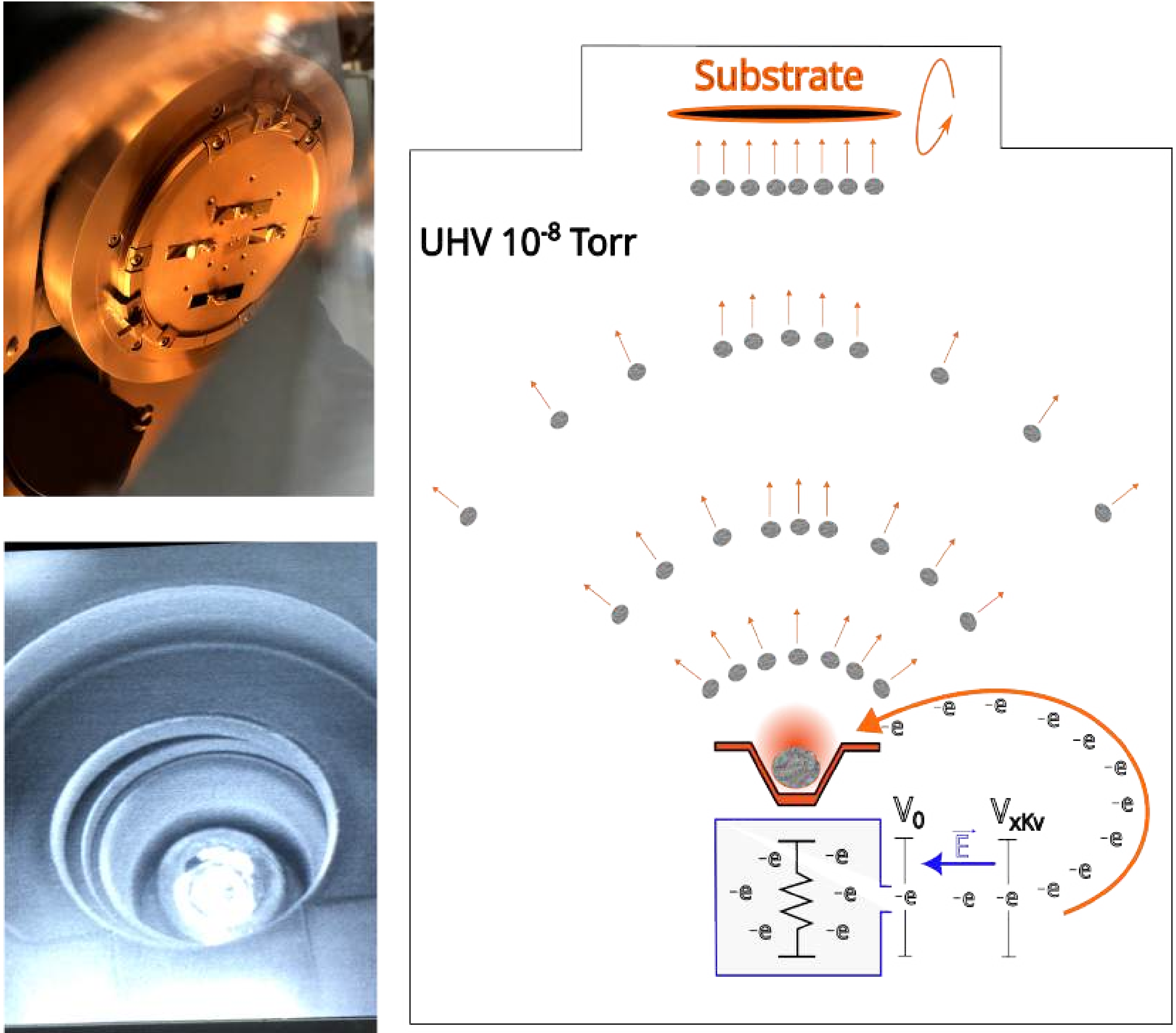

Figure 4.3: Bottom left: Aluminum metal in the e-beam crucible, brightness in the bottom of the image indicates the source of electron beam. The beam is deflected on to the aluminum, which melts and begins to evaporate on the samples above (Top Left). Right: E-beam deposition diagram, electrons are created by heated filament and accelerated towards a target material, heating the material until it boils and evaporates. The substrate has angle adjustment and is placed about a meter away from the crucible, enabling anisotropic deposition.

4.1.2 Lithography Overview

Nanolithography and microlithography are crucial techniques in both research and industry for fabricating structures at the micro- and nanoscale. These techniques enable the creation of intricate patterns and devices essential for semiconductor manufacturing, MEMS (Microelectromechanical Systems), optics, and

nanotechnology research.

Photolithography, the most widely used technique, utilizes light to transfer a geometric pattern to a light-sensitive chemical "photoresist" on the substrate. E-beam lithography (EBL) employs a focused beam of electrons to create patterns on an electron-sensitive resist. Nanoimprint lithography (NIL) involves pressing a template into a polymer resist to create patterns, similar to using a stamp. Soft lithography uses elastomeric stamps to transfer ink or molecules to a substrate, creating patterns.

Other techniques include scanning probe lithography (SPL), which uses a sharp probe to directly write patterns on a surface, and focused ion beam (FIB) lithography, which employs a focused beam of ions to remove or deposit material to create patterns. The galium ion FIB technique contaminates the samples it interacts with, making it incompatible with our purposes. However it would be possible to use argon ion FIB to avoid contamination. EUV lithography uses extreme ultraviolet light with a wavelength of around 13.5 nm to achieve sub-10 nm resolution, enabling the production of smaller and more efficient semiconductor devices. However this is generally not available to institutions and have exclusive industrial applications. It is a critical technology for the semiconductor industry, allowing for the high-volume production of advanced integrated circuits with increased device density and performance.

Each lithography technique has its own set of advantages and limitations, including factors like resolution, speed, cost, and complexity. These techniques are fundamental to the advancement of technology, enabling the production of smaller, faster, and more efficient devices. We employed techniques of photolithography to create all circuit components with the exception of the Josephson junctions, which are fabricated using EBL. Photolithography is fast and our system reaches resolutions up to 300 nm however to create reliable 3D bridge structures, EBL is the most widely used.

4.1.3 Photolithography

Photolithography is done using a Heilderber DWL 66+ system. Making a four inch wafer in high resolution, yielding around 80 × (0.5 cm^2) samples with micrometer resolution in about 24 hours. This resist is sensitive to the visible light spectrum, the whole process must be done within a yellow light environment. The photolithography step will create all features in our circuit down to 1 micrometer. The resist used for all circuits was AR-3120 (positive) which has up to 400 nm resolution and showed to be resistant to wet and dry etching of SF_6 and acids. On Figure 4.4 a 1 micron capacitor is displayed after it was written on to the resist, which was the smallest element in the superconducting circuits.

The main recipes used are shown on Table 4.1 and 4.2. The first recipe is spun at 4000 RPM yielding a thinner layer than the second recipe. If resist does not withstand etching processes, setting a thicker layer might be enough to withstand the process. It should also be noted that dose depends on the reflectivity or absorption of the surface material. Niobium has a darker tone then aluminum, it will therefore require a higher dose. It should also be noted that if exposed to weather the tone will change and the dose will also. Time between processes should be kept short and constant.

Step	Description
AR-3120	Spin - 4000 RPM, Bake: 100°C for 1 min
Resist thickness	500 nm (product datasheet)
Laser Power	Nb 64 mW - Al 60 mW
Developer	AR 300-47, gently stir for 1 min at room temperature.
Stopper	H2O, gently stir for 30s at room temperature.
Lift off	Acetone bath at 70°C for 5 min, ultrasound for 3 min, IPA bath with ultrasound for 3 min, spin dry or use N_2.

Table 4.1: Recipe 1.

Step	Description
AR-3120	Spin - 3500 RPM, Bake: 100°C for 1 min
Resist thickness	600 nm (product datasheet)
Laser Power	Al 62 mW
Developer	AR 300-47, gently stir for 1 min at room temperature.
Stopper	H_2O, gently stir for 30s at room temperature.
Lift off	Acetone bath at 70°C for 5 min, ultrasound for 3 min, IPA bath with ultrasound for 3 min, spin dry or use N_2.

Table 4.2: Recipe 2.

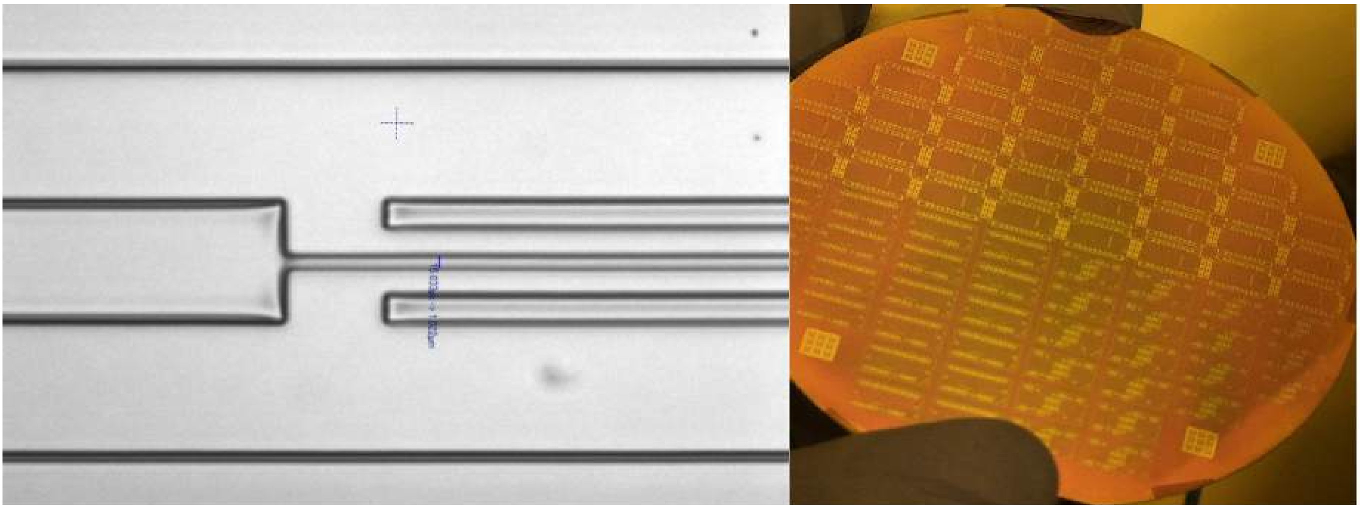

Figure 4.4: On the left we have a measurement of an 1 micrometer capacitor finger made of resist, on a optical microscope. Right: wafer after developing and heat treatment to harden resist for the etching procedure.

Wafer preparation Resist Deposition

To produce samples with reliable reproducibility, one must ensure to always follow the same steps. Take note of air moisture content, and temperature. For best results humidity should be between 40-60% and temperature 20-24C°, make sure to measure these values inside the film-hood where resist will be deposited. It is critical to reproducibility for the resist to be exposed to constant environment conditions during processing. It is important to have all tools laid out and rehearse movements to avoid subjecting the sample to varying procedures. Be aware that placing sample near a hot plate to rest for instance, is in someways tempering with it, therefore samples which are not being processed should remain in the a sample holder. Additionally planning procedures is also important to avoid accidents with hazardous chemicals.

With regard to resist deposition it is important to note that when applying resist, the size of the sample is also a factor. Furthermore, when using small pieces there are frequent border effects, which alter the height of the resist. Whole wafers however do not have edges, therefore the border effects are minimal. Working with full size wafer requires greater control of fabrication techniques, however the throughput increases dramatically. Furthermore working with full sized wafers offers less human error. When all samples are handled at once, they are more or less subject to the same conditions. When handling one sample at a time through all steps, adds an increasing amount of variations to the overall process. In the clean room the presence of the operator is detrimental to the process, therefore a good operator must attempt to leave no traces of his actions. Handling samples is tricky, tongs will damage circuit components, scratches to resist will cause unwanted etching or deposition. Therefore handling in itself should be minimal and mechanic.

The steps described here are general and will apply to wafers that have been contaminated and need to be cleaned or wafers with resist to be removed. Before starting any process in the clean room always start by washing the glassware unless it has already been done. The steps to prepare and clean the wafer are:

Step	**Description**
Acetone Bath	Place wafer in 70°C acetone bath for 3 min, make sure film hood is on and venting. (In case there was resist on the wafer, replace acetone and repeat.)
Ultrasound	Place wafer in ultrasound for 3 min.
IPA Bath	Rinse acetone with (IPA). Place wafer in IPA bath ultrasound 30s.
Dry	Dry the wafer off. The drying should start at the center ideally using Nitrogen, rotating to push out the IPA evenly towards the edges, this way contaminants will be pushed away.
Inspection	In the event that by looking towards the wafer at different angles and specs of dust are visible, it may be necessary to mechanically remove them using ultrafine lab-grade wipes. In this case, wipe then blow with Nitrogen.
Hot Plate	Place wafer in 100°C hot plate, to remove humidity from the surface.
Cold Plate	Place wafer in cold plate for 30 seconds.
Resist	Place wafer in spinner, apply resist evenly with a disposable pipette, 2ml should be enough for a 100 mm wafer. It may vary depending on resist viscosity. Make sure the wafer is evenly covered before starting the program, an example can be seen in the image below.
Spin	Run program.
Clean	Clean off excess resist from the bottom of the wafer using a qtip and acetone.
Heat Treatment	Place on a hot plate for heat treatment if necessary.

Considerations on Developers for Photo-lithography

Developers can sometimes react with the metal layer below. In this study three developers were tested 'AR 300-47', 'AR 300-35' and 'AR 300-26'. Particularly troublesome is Al because it reacts with both AR 300-26 and AR 300-47. Two routes can be taken, 300-35 can be used, then etch away Al by wet etching. Or use AR 300-26, the trouble here is that this stage must be optimized for feature size. Therefore there may or not be residue after developing is over, depends on a number of factors: Total area exposed, how homogeneous the exposure is, developer temperature, the atmosphere resist was exposed too, shelf life etc. This introduces room for error, so a second step of wet etching must be introduced when using 300-26. It should be noted that using AR 300-47 is not an option for Al samples as it causes a reaction which disables wet etching procedures described in this study. Furthermore while developing, some agitation is needed, however agitation will affect results. This can be a source for human error, and special care must be taken.

Double Exposure

Double exposure can be useful in many ways. Global alignment marks can be etched on to the substrate, so that a a especial reference will be available during the entire process on that wafer. For example we have Aluminum which can be hard to work with, using SEM alignment procedures for EBL. By etching away deep trenches in the substrate itself, aluminum circuits can be used on Si substrate. This comes at a compromise for alignment resolution but makes a process viable. Furthermore this allows for the use of a wafer multiple times. When testing new recipes or features.

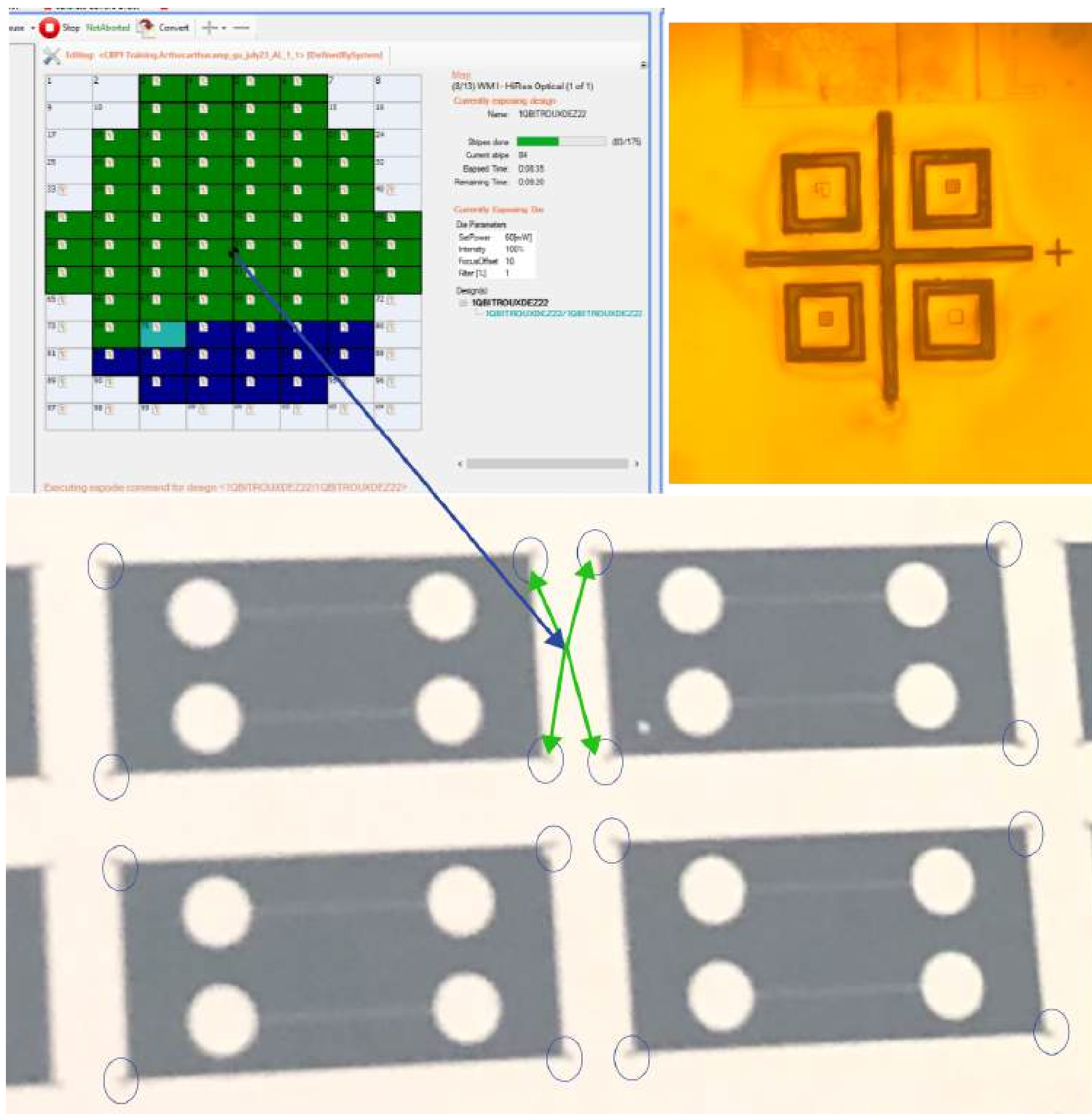

Figure 4.6: Wafer map, Displacement measurement cross. Image of wafer with circle pointing out blurry alignment marks. The blue arrow indicate where centering the wafer would probably land accoding to the wafermap. The user should then use one of the green arrow paths to find a cross and align the wafer.

The procedure for double exposure starts by deciding on die size and room for cutting. Die size should be large enough for the design and few microns for alignment marks on each corner. A new GDS file with marks must be made right within the die area however they should be placed within the region to be cut or a special designated area within the sample. Place the wafer and run wafer measurement to centralize it. Run focus alignment procedure and run exposure, which should take only a few minutes, perform etching or deposition to pattern the wafer permanently. Clean the wafer as explained earlier within this section. Next load the wafer in precisely as it was done before, a small rotation of .0005 radian is tolerated and made up for, but higher than this and the wafer will need to be removed from the chuck replaced. A hint would be to pay attention to what pressure is being used by what fingers to repeat the precise movement. It is frustrating to have to handle the wafer multiple times as dust is sure to be seen on it.

Once wafer is loaded properly, centralize the wafer and it should be near to where the first centralization was. Find the nearest cross to the middle, it will in one of the 4 dies near the center for the configuration on Figure 4.6. After finding one of the crosses, it must be speculated what die the sample was moved to and calculate the distance from the center of the wafer. Use return to center, next put in the calculated values for displacement on the chuck, and make sure it leads to the same mark. If this is confirmed, some displacement is noticed and can be fixed for by defining a new center for the wafer using the precise calculated distance. This being because it is virtually impossible to place the wafer perfectly the same way. Therefore the user will now centralize camera on the cross, and then use the step function to travel exactly back to the calculated wafer center. Now the user uses defines this spot as the new center, and the new exposures will be aligned to the old ones.

The alignment marks serve also as metric for how aligned the new exposures are, providing a basis for calculating the respective offset of the current exposure from the original mapping marks. As shown on Figure 4.6b, the inner squares which in this case are 10μm by 10μm are placed in the 40μm by 40μm area of the larger square should be exactly in the center. The distance it deviates from the center can be measured and used to achieve better aligned masks as further lithography steps occur. A very useful feature for circuit fabrication.

4.1.4 Etching

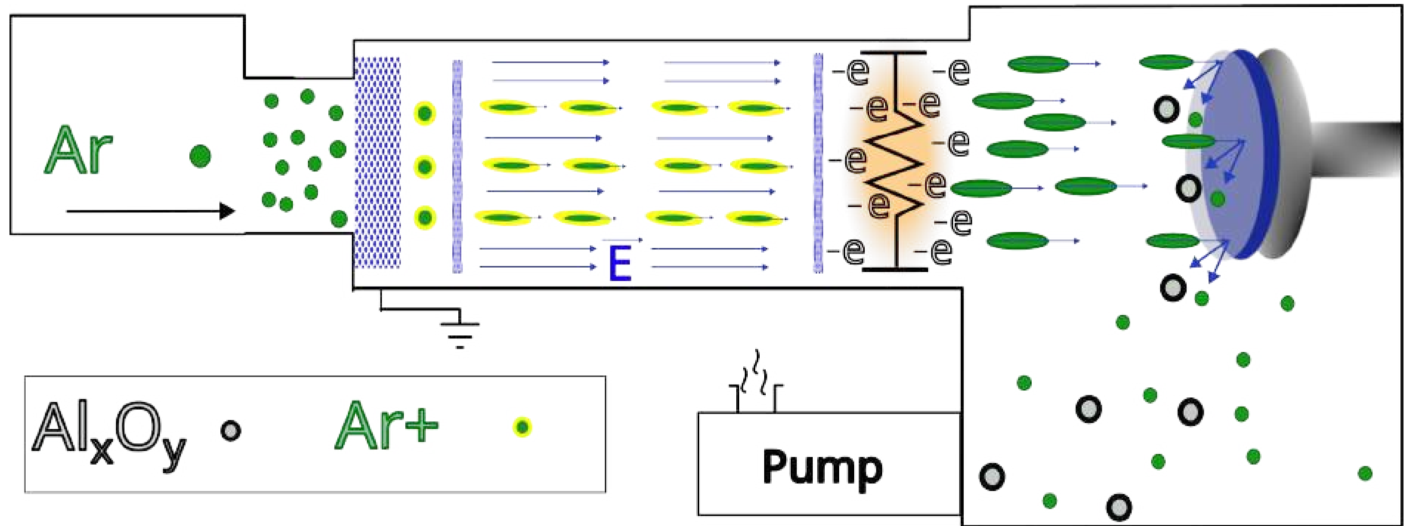

Figure 4.7: Diagram of ion milling system. Argon gas is stripped of its electrons, then subjected to an electric field. After acceleration it passes by a heated tungsten filament, and is neutralized by the free electrons. It then makes its way to mechanically remove atoms from the surface. Al_xO_y is easily removed by this method.

Wet and dry etching are essential processes in nanofabrication used to pattern or selectively remove materials from a substrate. Essentially transferring lithography patterns to the thin film on the substrate. Wet etching involves immersing a substrate in a liquid etchant that selectively reacts with the material being removed. This process is isotropic, meaning it etches in all directions, which can lead to undercutting of the mask if not controlled. Wet etching is relatively simple, inexpensive, and can be highly selective if the etchant is chosen carefully. Dry etching involves removing material using gas-phase chemicals or plasma. Dry etching can be either isotropic or anisotropic, depending on the process used. Anisotropic dry etching, such as reactive ion etching (RIE), etches vertically downward, resulting in high etch resolution and less undercutting compared to wet etching. Dry etching is highly controllable and allows for precise patterning, making it ideal for nanofabrication. Both wet and dry etching are used in nanofabrication for various purposes, including creating nano-structures, removing layers to expose underlying structures, and defining patterns for integrated circuits and other nano-devices. Each method has its advantages and limitations, and the choice between them depends on the specific requirements of the fabrication process.

Ion Milling

Ion milling is process used to remove oxide prior to thin film deposition. Argon atoms are stripped of their electrons accelerated and projected at the rotating sample. On their way they pass by a heated tungsten filament which provides electrons to neutralize the argon atoms before they make their way to the sample. They physically sputter away the target material as can be seen on Figure 4.7, depending on argon energy

and material hardness. We use ion milling before depositing the first layer of aluminum during shadow evaporation to clean contacts. We also perform ion milling before depositing the initial layer of metallic film on a wafer.

Resist related defects

During our analyses we encountered defects of the type "veil of death", term coined in [49]. Resist can be seen still attached to the junction (Fig. 4.8, plasma ashing allows for selective removal of organic compounds. A common process to remove this organic residue is called plasma Ashing or 'descum'. This process consists of heating the sample and subjecting it to a plasma of O_2 at low pressures. This is an important step to make pristine samples free from contaminants. Unfortunately this process was not included in our process, due to it being unavailable in our facilities.

Reactive Ion Etching Niobium Thin Film over Silicone or Aluminum

Reactive Ion Etching is a predominantly chemical process, in which a sample is exposed to a plasma surface treatment. This plasma will have distinct properties depending on the elemental composition of the gas in the chamber, furthermore there are controllable variables such as chamber pressure, inflow of gas, and total power used. A general rule to make processes more repeatable is to try to use low pressures and power. The recipe which yielded best results for our procedure used SF_6 gas at 10 sccm flow, 100W power and 30 mTorr chamber pressure.

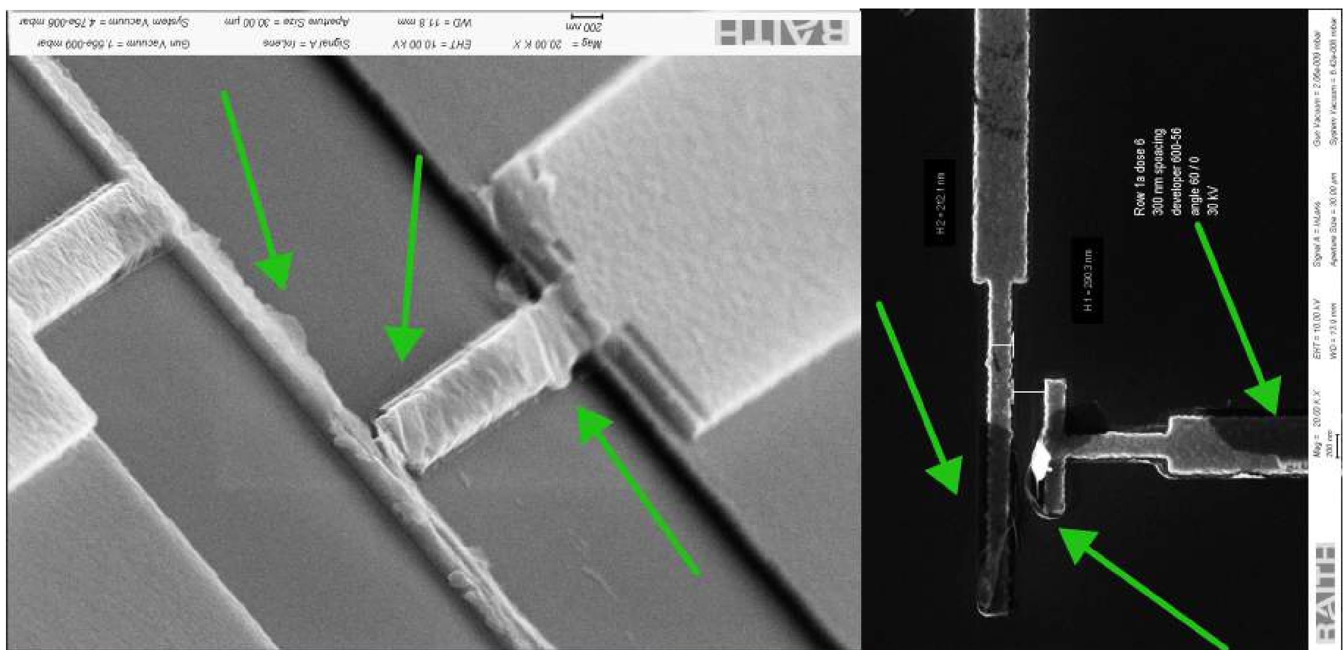

Figure 4.8: SEM image showing left over resist on Josephson junctions. Green arrows indicate polymer leftovers.

For the etching of Nb using a mixture of SF_6 and Ar results were highly unreliable, leading us to argue against the use of SF_6 to etch away Nb from Si substrate, because simply it is not a selective process. Frequent problems such as uneven etching or sputtering damage to the Si for extended exposures these can be seen at the top of Figure 4.10.

In addition it is possible to increase success yield, if the plasma etching equipment has a built in gas spectrometer. This way Si will start to be detected once Nb is etched away. Yet another option is to use Nb over AlO_3 substrate [68], or use commercially available wet enchants for Nb. This was not our case and efforts to optimize this recipe were fruitless. The best results were achieved with recipe of: 5 sccm SF6, 3.5 sccm Ar, 30 W, 30 mTorr.

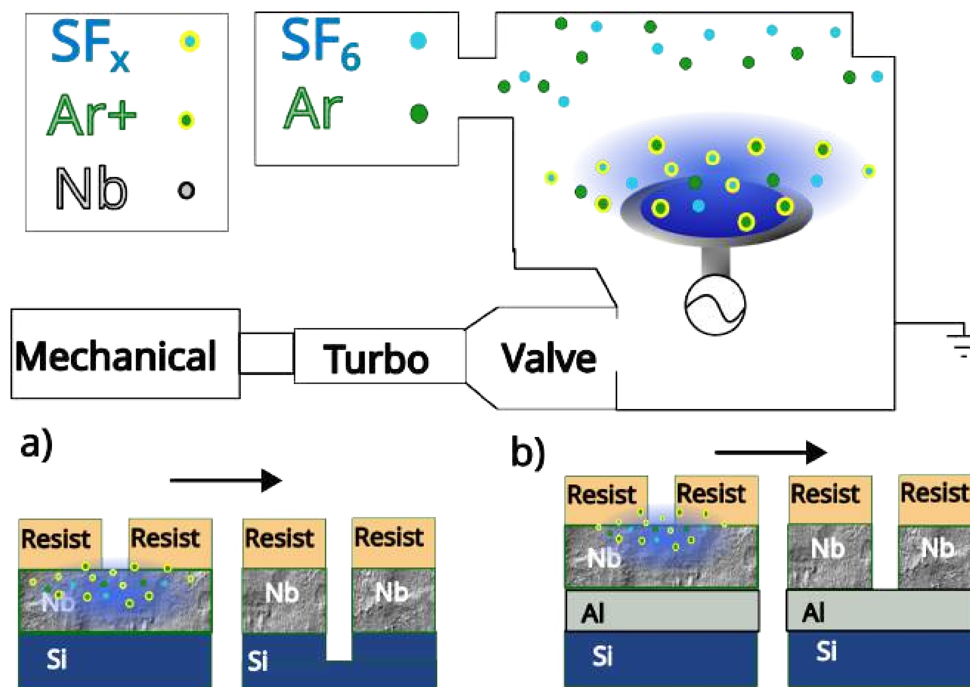

Figure 4.9: Reactive ion etching of Nb with SF_6 and Ar plasma diagram. A diagram shows the interaction of the particles with the RF field, creating a plasma over the sample. a) Etching of Nb over Si with SF_6. b)Etching of Nb over a passive layer of Al with SF_6.

There were frequent problems such as inhomogeneous etching through out the wafer as shown on Figure 4.10. Furthermore we observed that while some parts of the wafer had deep trenches others would still have remains of Nb, yielding a very low amount of good samples. The SEM images show contact pad features for testing Josephson junctions. The thin niobium layer has 100 nm, however in the two different contacts there is from 600-800 nm of Si substrate etched away. Therefore any junction deposited on these contacts would yield an open circuit measurement. Following guidance found on book [69], one should opt for selective recipes. This logic guided us to creating a passive Al layer between the substrate and the Nb film seen on Figure 4.10.

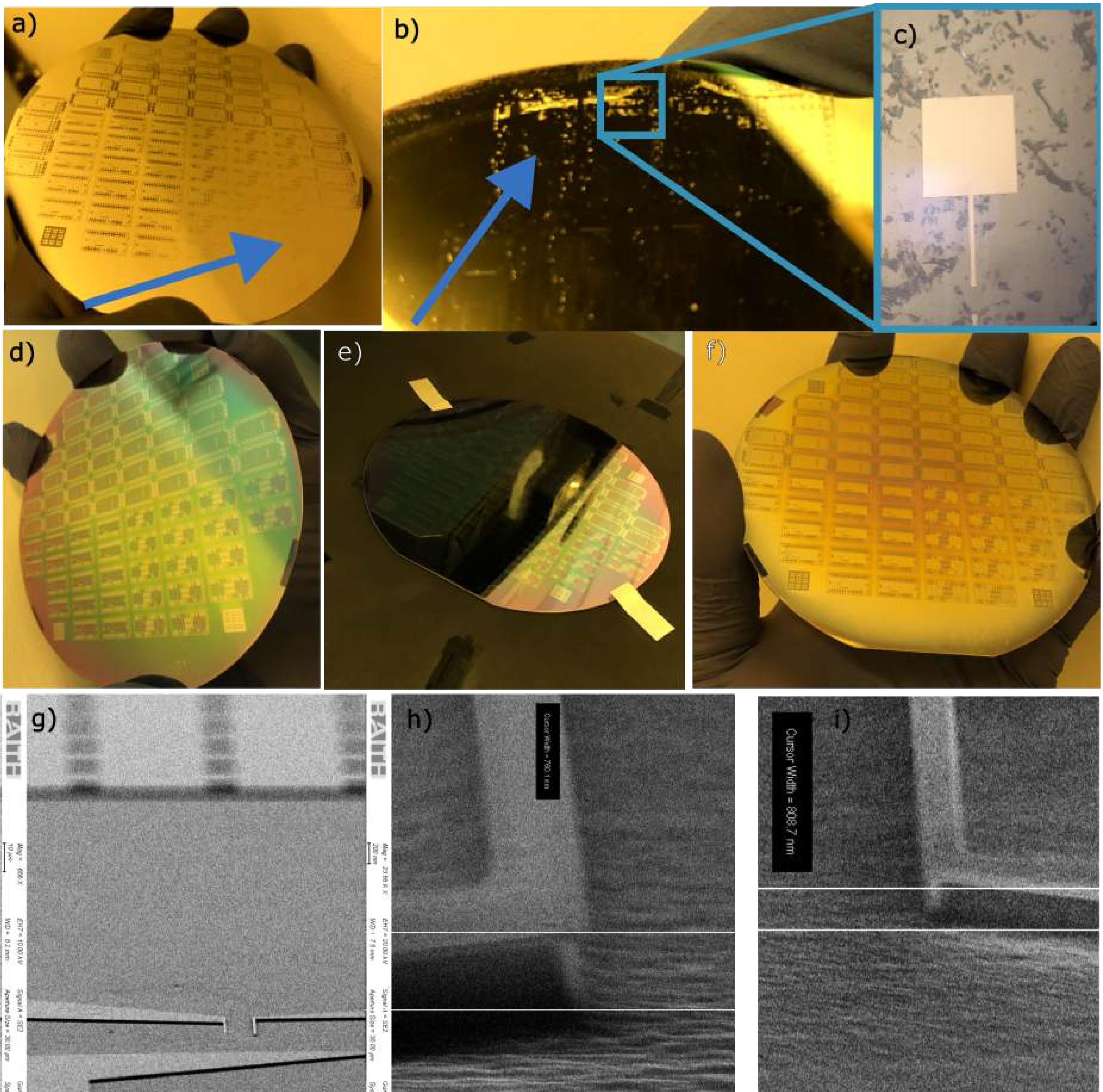

Figure 4.10: a)Wafer showing uneven etching, b) wafer with damaged substrate, c) close up of damaged region in optical microscope. d,e)Etching of Si/Nb Wafer, goes from dark silvery color to dark grey (f). g-i) SEM images demonstrating overetching of up to 800 nm (measurements are not exact as the sample is clearly at a very high angle $> 80°$, however there is still some distortion.SF_6 is a powerful Si etchant, once the Nb layer is etched away it begins to fiercely remove the Si. Proving difficult to optimize reproducible recipes.g) two contact structures for deposition of Josephson junctions. h,i) Close up shows overetched substrate.

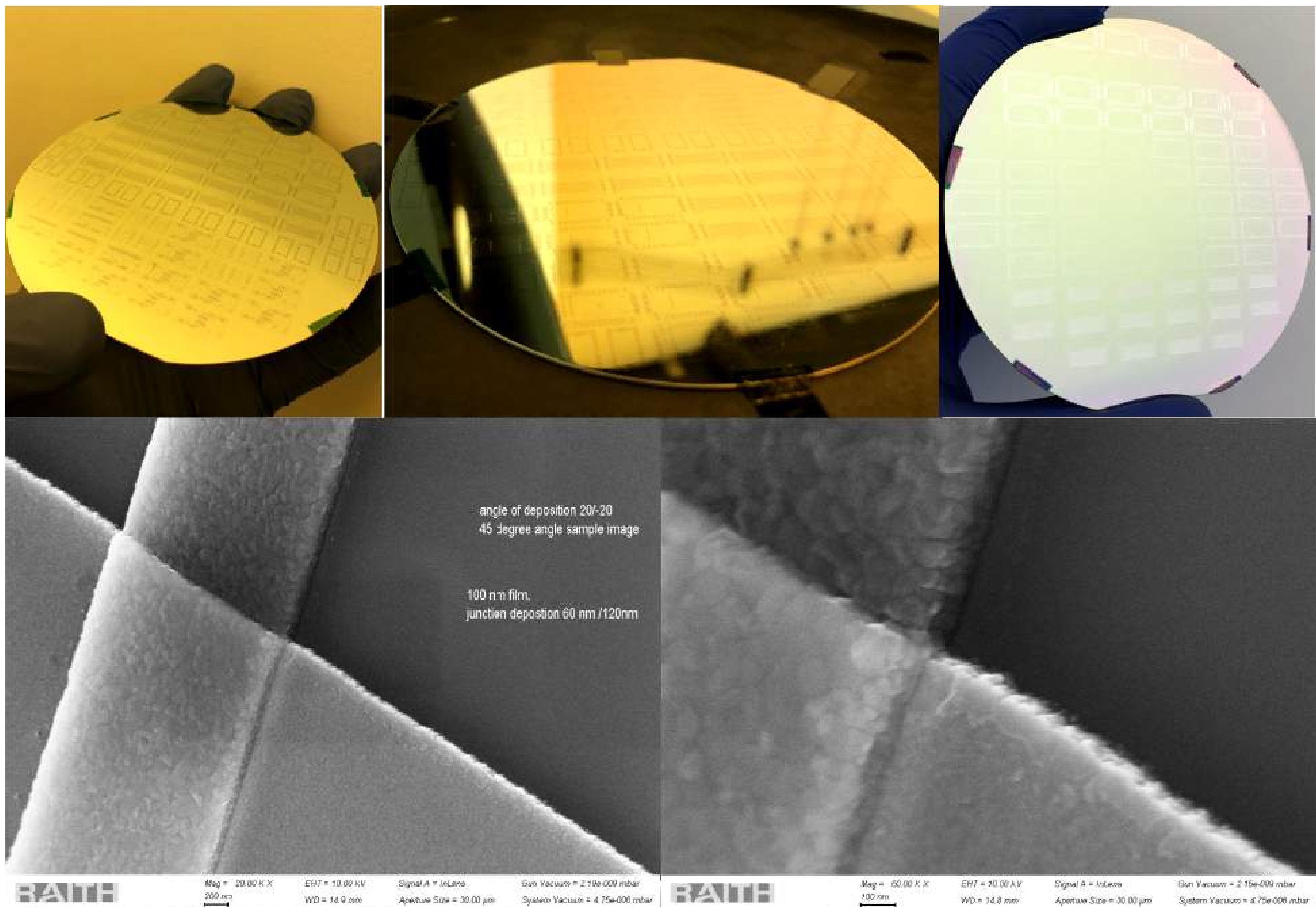

Figure 4.11: Top : Images of patterned trilayer wafer Al (20 nm)/ Nb (80nm) / Al (20 nm) before and after dry etching. At this point only two layers Nb (80nm) / Al (20 nm) are left on the substrate. Starting from the top left, patterned wafer after wet etching. Center image shows wafer positioned on the RIE carbon chuck in the etching chamber, Since Al is etched at much slower rate, it protects the substrate. The Al can be easily removed with wet etching procedures. Top Right shows wafer after etching the dark silvery color transforms into very light and reflective metalic color with only a thin film of Al 20 nm patterned region. Bottom: Two SEM images (20k mag and 60k mag) of Josephson Junction intersection with previously fabricated pads on trilayer Si/Al/Nb/Al Wafer. This angled image shows good contact, and that the Si wafer was preserved during etching.

Aluminum can be used as a passive layer to stop Niobium etching. This enables Nb to be etched by Sf6 plasma while still using a Si substrate. While there are selective plasmas for Nb/Si they involve hazardous chemicals. We used 20 nm of Al as a passive layer and this yielded reproducible results. SEM images showing no over etching can be seen on Figure 4.11.

Aluminum Wet Etching

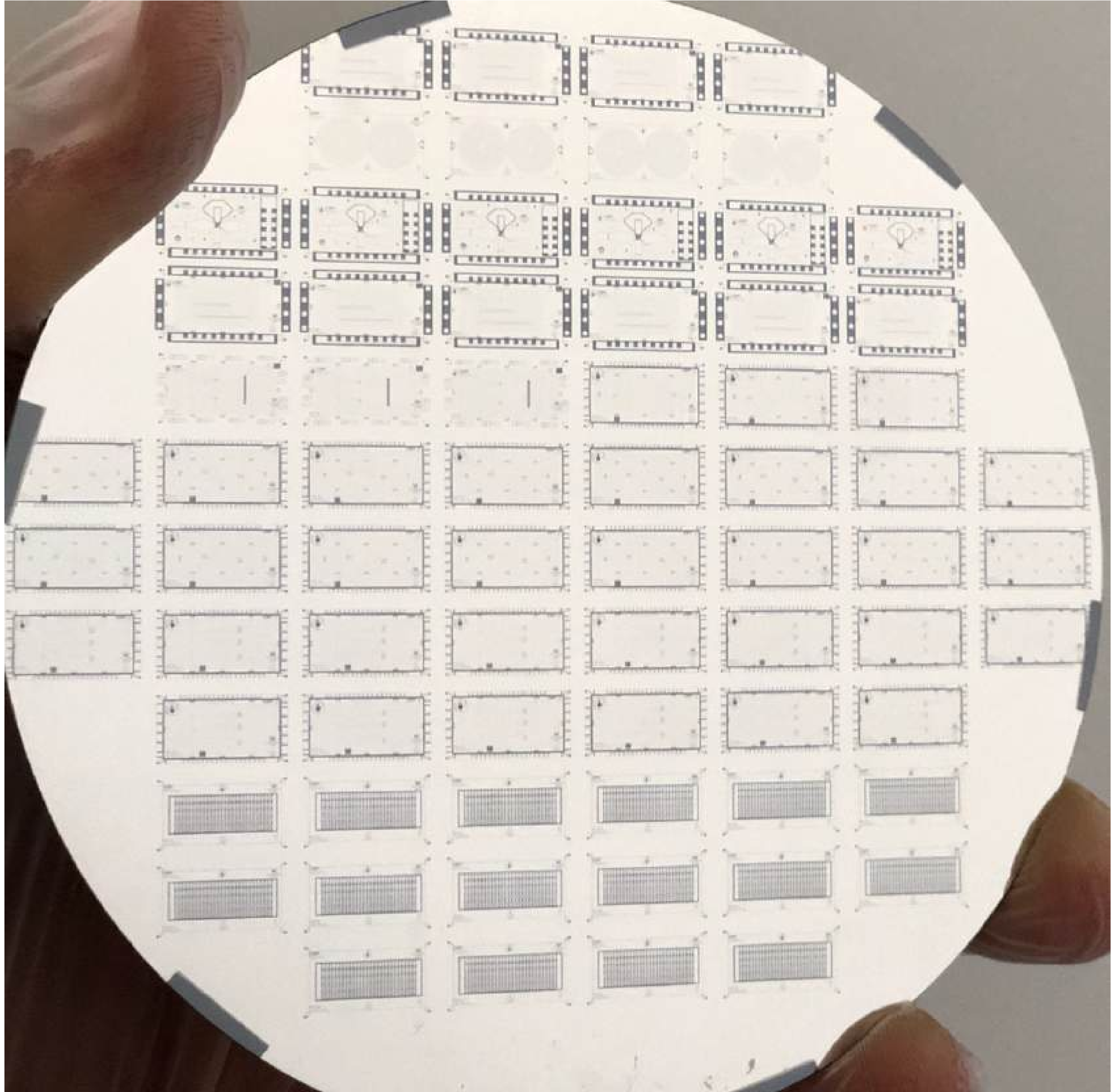

Figure 4.12: In the image a trilayer film Al (20 nm)/ Nb (80nm) / Al (20 nm) Si wafer is seen, a particularly pristine sample with a very high yield.

Aluminum can be etched away using a mixture of acids (Phosphoric acid: Acetic acid: Nitric acid: Water (73:3:3:21)). This mixture is easily prepared, providing a practical means to etch Aluminum. Phosphoric acid reacts with aluminum to form aluminum phosphate and hydrogen gas. The reaction is typically slower

compared to other acids like hydrochloric acid, which can rapidly dissolve aluminum. Nevertheless this process is much safer.

Wet etching can be enhanced if subjected to higher temperatures or ultrasound. However a 10 seconds in ultrasound is enough to see damage to features with edges of a 1-3 micrometers. Therefore a careful balance between etching time and resist thickness to preserve small features while being able to etch away every small exposed feature. Essentially smaller lithographic features need more time to be etched, however small features which are near large exposed areas start to be removed, components that suffer first are isolation between pad and capacitors. Special care is needed to make sure the small structures make it through the etching steps. When etching is too aggressive one turns to raising the resist height, as means to increase film protection. However the recipe needs to be optimized for a new dose, and thicker resists offer lower resolutions.

4.1.5 Superconducting Circuits

The fabrication of superconducting circuits using thin films of materials like Niobium (Nb) and Aluminum (Al) presents challenges for fabrication and functionality. In this work we explore a tri-layer alternative, to overcome hurdles naturally imposed by superconducting Nb and Al films.

In the following Table 4.3, we display all recipes which were optimized during the course of this thesis. We were able to map out their characteristics, discussed their advantages a disadvantages. Here we take into considerations durability, because samples often took weeks to be processed. Alignment scale, necessary element for fabrication of Josephson junctions. Selectivity of the material. This is very important, it is a waste of time to try to optimize a non selective recipe.

Substrate	Durability (hours)	Alignment scale (MEV)	Selective Etching (acid)	Unwanted Si etching (SF_6)
Si/Nb	High	<200	yes	yes
Si/Nb/Al	High	<100 nm	unreactive	yes
Si/Al	High	Not visible	yes	no
Si/Al (Si etched)	High	< micron	yes	no
Si/Al/Nb	High	<200	yes	no
Si/Al/Nb/Al	High	<100 nm	yes	no

Table 4.3: Table showing recipes we optimized: advantages and disadvantages to be considered. Here we show problems associated with pure Al and Nb films and address solutions to both cases. Al can have a prior step where alignment marks can be etched onto the wafer itself using SF_6. While Nb can be used with passive layers of Al in multiple configurations.

4.1.6 Scanning Electron Microscope

The scanning electron microscope (SEM) is a fundamental tool in the nanofabrication process. Its ability to provide high-resolution images and detailed surface information of nanometric structures. The SEM operates on the principle of scanning a focused electron beam across a specimen's surface. When the beam

interacts with the specimen, various signals are emitted, including secondary electrons, backscattered electrons, and characteristic X-rays. These signals are then detected and used to create images and gather information about the specimen's composition and topography.

The electron source in an SEM is typically a tungsten filament or a field emission gun (FEG). The tungsten filament emits electrons when heated, while the FEG produces a more coherent and intense electron beam, resulting in higher resolution images. The electron beam is focused and controlled by a series of electromagnetic lenses. These lenses ensure that the beam remains narrow and focused as it scans across the specimen's surface. The specimen chamber holds the specimen and provides a controlled environment for imaging. Several detectors are used in an SEM to capture different signals emitted from the specimen. The most common detectors are the secondary electron detector, which captures low-energy electrons, and the backscattered electron detector, which captures high-energy electrons. The imaging system in an SEM includes the electron beam scanning system and the detectors. The scanning system controls the position of the electron beam, while the detectors capture the emitted signals to create images of the specimen's surface. The control system of an SEM includes the computer and software used to control the instrument's operation. It allows the user to adjust imaging parameters, such as beam intensity and scan speed, and to acquire and analyze images and data.

SEMs can be equipped with additional to detectors to provide other analysis options such as Energy Dispersive X-ray Spectroscopy (EDS) and Electron Backscatter Diffraction (EBSD) which are two important techniques often used in conjunction with scanning electron microscopes (SEMs) for materials analysis. EDS detects characteristic X-rays emitted by a specimen when it is bombarded with a focused electron beam in an SEM. The energy of the X-rays corresponds to the elemental composition of the specimen, allowing for qualitative and quantitative elemental analysis. EDS is used to determine the chemical composition of materials, identify unknown elements, map the distribution of elements within a sample, and study elemental changes in response to external stimuli. This is usefull to see the quality of superconducting circuits or identify impurities, assuring samples meet desired specifications. EBSD measures the diffraction pattern of backscattered electrons from a crystalline sample in an SEM. By analyzing the diffraction pattern, EBSD can determine crystal orientation, grain size, and phase information of the sample. EBSD is used in materials science to study micro structures, texture, and deformation mechanisms in materials. It is valuable for understanding the properties and behavior of materials at the microscopic level. In summary, EDS and EBSD are complementary techniques to SEM imaging, providing valuable information about the composition, structure, and properties of materials. In conclusion, the scanning electron microscope is a powerful tool with a wide range of applications in scientific research, due to its ability to provide high-resolution images and detailed surface information.

4.1.7 Nanolithography EBL

Electron beam nanolithography (EBL) is an advanced manufacturing technique used to create nanometric structures. Electron beam nanolithography uses a highly focused beam of electrons to write patterns on a surface. EBL is considered a slow process, this is mostly because electrons are fermions and can not be made to occupy the same space. Therefore EBL is used for experimental purposes more than industry. The semiconductor industry uses lithography processes using the extreme ultraviolet spectrum. This process achieves throughput necessary for industry standards while also achieving nanometric resolutions.

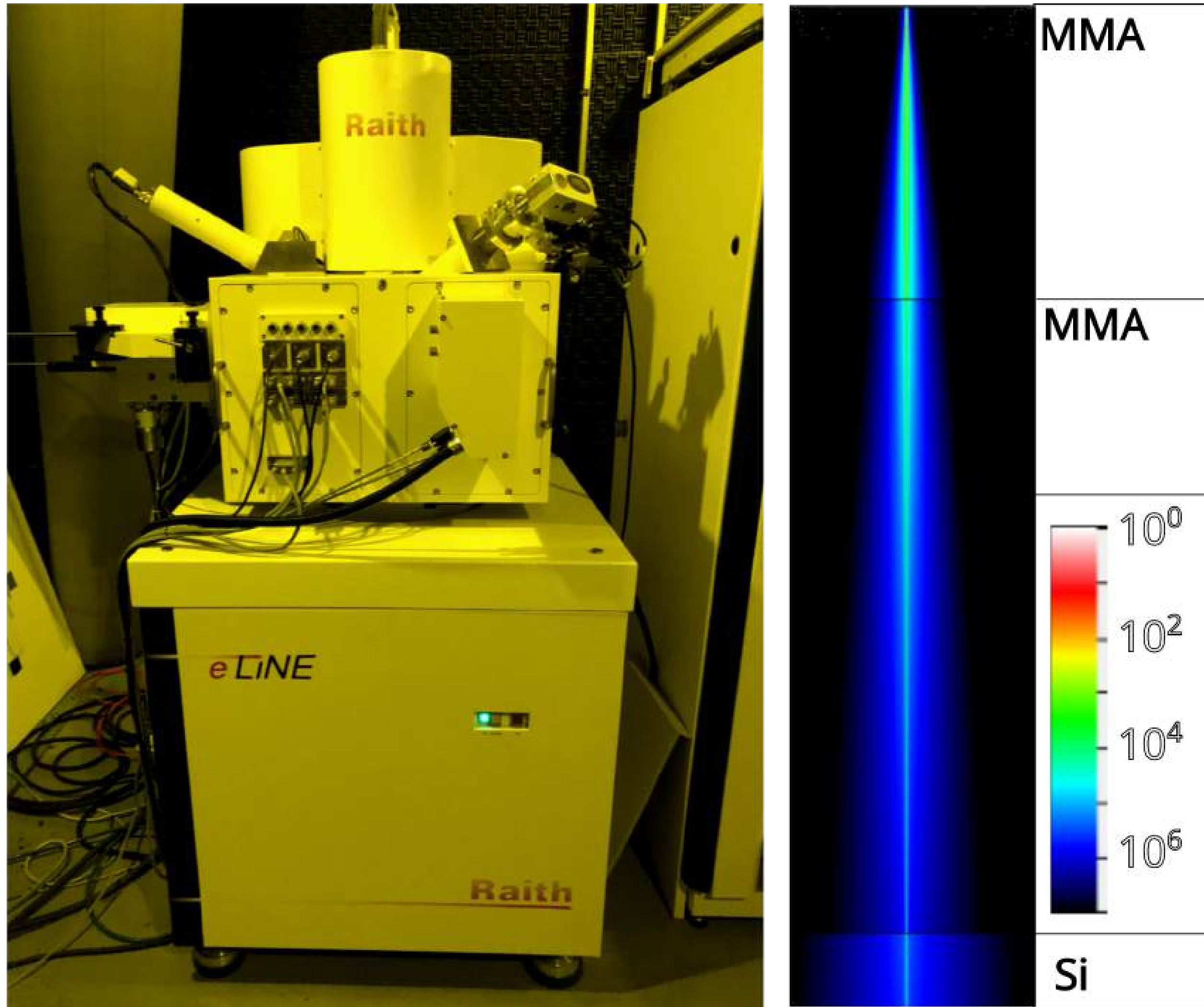

Figure 4.13: LABNANO CBPF Raith e-Line 30 kV field emission electron beam lithography system on the left, device capable of nanometric patterning on ultra flat surfaces such as Silicon or Saphire wafers. On the right simulation of deposited energy by e-beam for the specific resist stack explored in this study to fabricate Josephson Junctions.

There are two categories of sources in electron microscopes: conventional sources and field emission (FE) sources. Conventional sources include tungsten filaments and lanthanum hexaboride (LaB6) single-crystal tips. FE sources use a cold cathode or a Schottky emitter. FE sources offer better imaging and better lithography, but are more expensive. In the past SEMs were adapted into lithography systems, to achieve higher resolution higher accelerating voltage must be used. However these systems are much more expensive and not widely available from a global perspective.

Nano lithography electron beam is a versatile tool in nanofabrication research. Here we employ it to fabricate bridge structures for Josephson Junctions. The system used in this thesis is a Raith e-line 30

kV system. In this study we discuss challenges and methodology for Josephson junction fabrication using this system. Thinner resist stacks offer far greater resolution than thicker ones. For our applications we require a high resist stack. This implicated in finding creative ways to improve low energy EBL resolution for thick resist stacks.

The system used to conduct this research is was generously provided by LABNANO CBPF, a Raith e-Line 30 kV field emission electron beam lithography system. Which has accelerating Voltage: 0.5-30kV, min linewidth 8nm. Overlay accuracy of 40 nm and a travel range of 100x100 mm^2. The system is shown on image 4.13. This system was used both to routinely capture SEM images and perform nanolithography. It can not be understaded the importance of having this system directly available for this project, it enabled dynamic inspection and continuos trials. While this technology is decades old and far too slow for industry applications, it is and will be a very powerful tool for research.

Nanolithography recipes require optimization of various parameters such as exposure time, dose, resists, developers, process time/temperature/humidity, sample lifetime, storage procedure and others. It consists of a very delicate process and for this reason recipes need to be carefully optimized. Simply changing the agitation rate during development will alter results. The procedure should be developed to minimize human induced error as much as possible.

One parameter is system calibration. The beam must be finely tuned before lithography procedures commence. The electron optics system of the lithography tool is typically calibrated for a specific range of beam voltages. Adapting to a lower voltage may necessitate recalibration of the entire system to ensure accurate and reliable performance.

In summary, creating a nano lithography electron beam recipe requires a comprehensive understanding of the interactions between the electron beam and the material, as well as thorough optimization of process parameters to maintain or improve the quality of the lithographic results. It often involves a combination of experimental testing, simulation, and careful adjustments to achieve the desired outcomes.

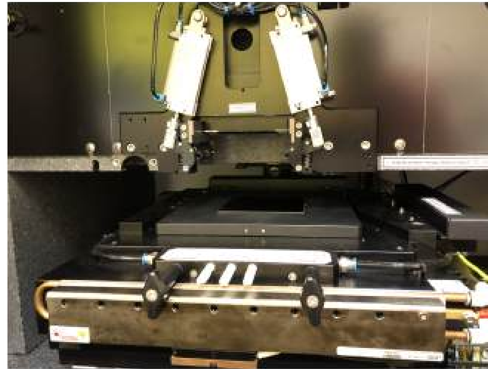

Figure 4.1: Top) LABNANO CBPF, photo lithography system Heilderberg DWL 66+. Bottom) LFDQ IFGW AJA Magnetron sputtering and angled e-beam deposition system.

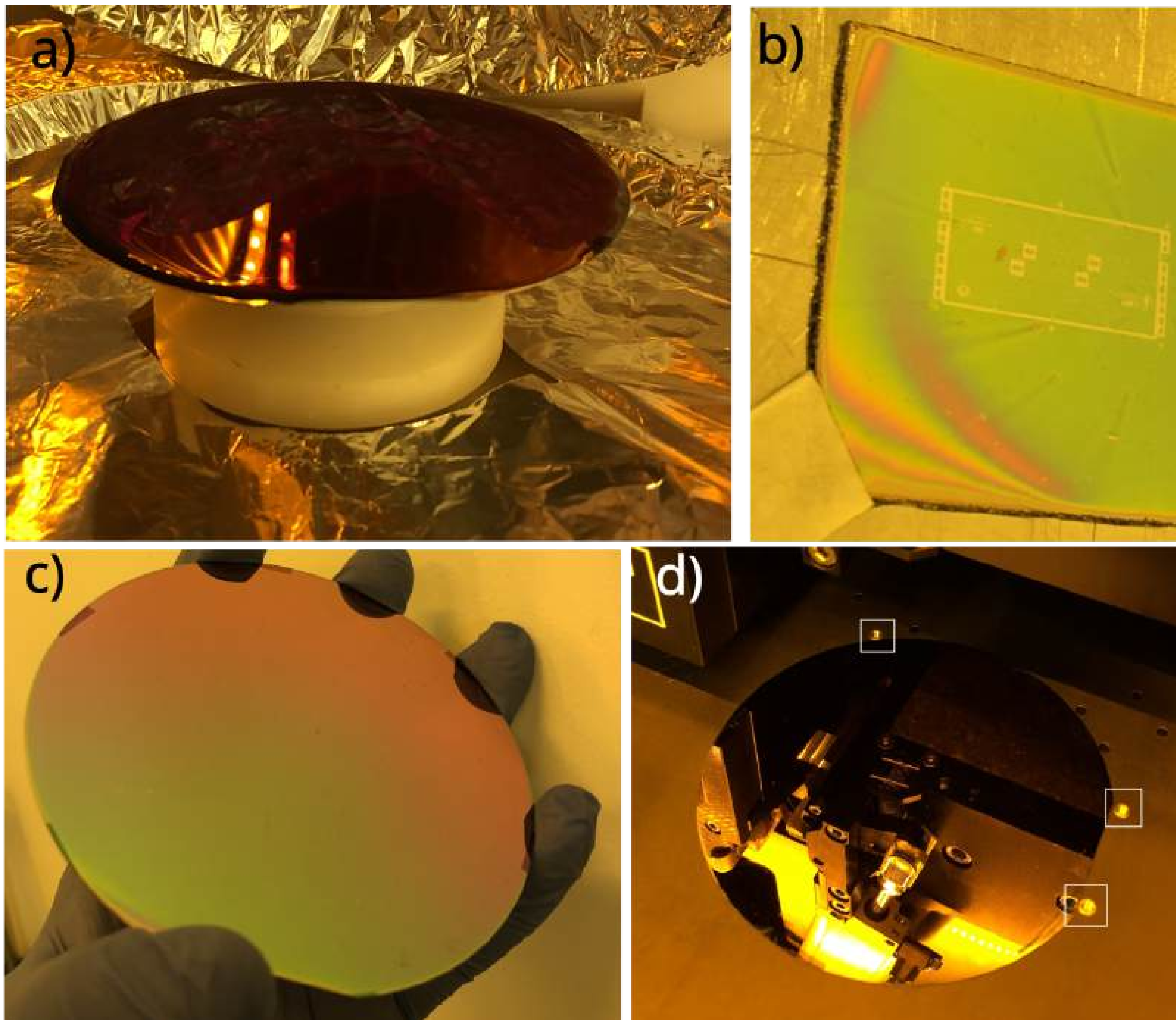

Figure 4.5: a) The first image shows the wafer positioned within the spinner covered with resist. b) Resist defects: shooting star and edge fringes. c) Perfect resist deposition, no visible shooting stars, the coating is evenly spread with out contaminants. d) This image shows how the wafer is properly aligned. It is critical that the drawing is oriented according to the crystallography of the wafer for cutting purposes. By setting the wafer chanfer flat on the positioning screws, then pushing towards the back screw, guarantees less variation between exposures.

4.2 Josephson Junctions Fabrication Modeling

Fundamentally, the objective is to pattern the resist to form a bridge, as illustrated in Figure 4.14a-d. As depicted, the challenge involves employing a straight electron beam to intricately sculpt sideways beneath the resist's top layer. This process is feasible because the electron beam generates backscattered electrons along its path and it penetrates several micrometers into the substrate, implying backscattered can travel a long distance from point of incidence. Backscattered electrons are highlighted in Figure 4.14g with red trajectories. A critical aspect of enhancing the fabrication process quality is understanding the impact of these backscattered electrons and acknowledging the variability in the sensitivity of the resist layers employed, specifically PMMA (230 nm) over MMA (500 nm).

The challenge in electron beam lithography (EBL) processes traditionally lies in optimizing to achieve the best matching feature dimensions. For any given exposure area, a portion of the incident dose is inevitably distributed to surrounding regions, resulting in variations in the deposited dose near the beam. This phenomenon, known as the proximity effect, is mitigated using PEC techniques, which modify the dose distribution across the features to achieve a constant deposition dose within the exposed area [46]. However, these techniques primarily aim to establish a uniform dose for a given design. Here, we endeavour to advance further by examining how undercuts can be engineered to preserve the design structures of the upper resist layer. The challenge emerges from the discrepancy between the dose required to pattern the design and the dose from backscattered electrons needed to sensitize the lower resist layer, all while maintaining the integrity of the top resist layer. Given that patterning the top resist layer usually does not deposit enough dose to open the undercut in the bottom layer, an increased base dose is necessary. This adjustment, however, leads to overdosing in both the top and bottom resist layers, potentially causing deformation, weakening, and deviation from designed dimensions. While PEC helps prevent damage to the bridge structure, it is often insufficient for 30 kV applications in fully address these issues. Thus, as demonstrated in our study, a careful selection of geometric features is also crucial. We show that this approach is of uttermost importance in creating reproducible structures for the fabrication of Josephson junctions.

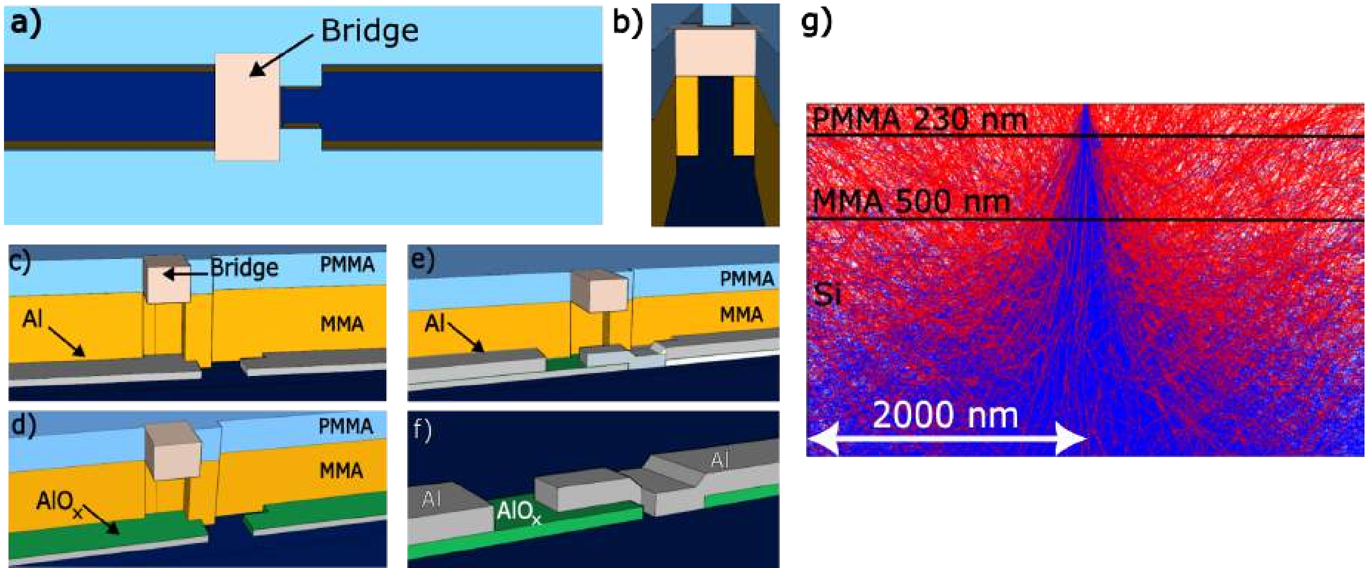

Figure 4.14: Schematic representation of the pattern transferred onto a double-layer resist stack followed by aluminium deposition process, delineating the steps involved in fabricating Josephson junctions, alongside electron trajectory simulation within the resist layers. a) Dolan Josephson junction scheme showcasing the exposed area (in dark blue) and the central bridge region (in grey). b) Bird's-eye perspective of the anticipated Josephson junction bridge structure. c) Initial 30° angle deposition, d) oxidation phase, e) subsequent -30° angle deposition. f) Representation of the Josephson junction post-lift-off process, with the green coating symbolizing the AlO_x layer. g) Visualization of electron dispersion trajectories in a 230 nm PMMA layer (top) and a 500 nm MMA Co-polymer layer (bottom), both situated on a silicon substrate, under the influence of a 30 kV electron beam. The trajectories of the primary electrons from the incident beam are depicted in blue, whereas the backscattered electrons are illustrated in red.

The test structures were meticulously designed as 10 rows of 27 pads, intended to be interconnected by a Josephson junction. Each pad consists of rectangular sections measuring $200 \times 200\,\mu m^2$, with a separation of $100\,\mu m$ between them. These structures were fabricated by initially depositing a 100 nm thick layer of Nb or Al onto high-resistivity silicon wafers ($\rho > 10k\Omega, cm$). The patterning of the design was achieved using optical lithography on a Heidelberg DWL 66+, followed by the selective removal of materials through wet etching for Aluminum or SF_6 reactive ion etching (RIE) for Niobium.

For the fabrication of the Josephson junctions, electron beam lithography was employed, utilizing a 30 kV electron beam and the Dolan technique on a Raith E-Line Plus. The chosen bottom resist was a co-polymer, specifically AR-P 617.08 (MMA), known for its sensitivity being 3 to 4 times greater than that of PMMA resists. It was applied as a 500 nm coating by spin-coating at 4000 rpm. The top e-beam resist selected was PMMA 950k; the optimal thickness, achieved by selecting 672.045, resulted in a 230 nm thick layer when also spun at 4000 rpm. Each resist layer was subjected to a baking process— the first at 200°C and the second at 180°C, each for 10 minutes— to ensure the integrity of the resist structure for Josephson junction. For room temperature measurements, we employed a Lock-In amplifier coupled with contact needle probing. Measurements in the millikelvin range were performed using a BlueFors DL400 Dilution Refrigerator.

The Josephson junctions were fabricated through a standard Dolan-bridge double-angle evaporation of aluminium in a dedicated ultra-high vacuum (UHV) deposition system [41]. This system, crucial for finely adjusting the tunnelling barrier and preventing contamination, operates under conditions that significantly enhance the quality and reproducibility of the junctions. A detailed description of sample fabrication and techniques used is provided in the appendix. Briefly, the fabrication process begins with e-beam exposure, followed by development in MIBK:IPA 1:3 and rinsing in isopropyl alcohol (IPA) to stop the development process, then gently drying with N_2. The samples are subsequently placed in the deposition chamber for thin film deposition and oxidation. The first step involves depositing ultrapure (99.999%) Al at a 30° angle relative to the sample's normal (Figure 4.14c), using e-beam vapour deposition in a UHV environment (10^{-9} Torr) to minimize impurities and achieve anisotropic deposition by positioning the sample approximately a meter away from the crucible. Following the first deposition, the sample is moved to a separate chamber and exposed to an O_2 atmosphere at 5.7 Torr to form a controlled oxide barrier (Figure 4.14d). Finally, the sample is returned to the main chamber for a second Al deposition at an angle of -30° (Figure 4.14e), completing the fabrication process.

Following the deposition process, the sample is subjected to a lift-off procedure, uncovering the structures depicted in Figure 4.14f. The thin oxide barrier formed during deposition exhibits a notable variation in characteristic resistance at room temperature, which can range from a few Ohms to tens of kOhms, depending on the junction's area and size. This variation in room temperature resistance is directly proportional to the critical current value below the superconductor's critical temperature. By optimizing this resistance, it is possible to finely adjust the performance of these devices, enhancing their functionality and efficiency in superconducting circuits.

Achieving consistent resistance measurements for multiple junctions at room temperature necessitates adherence to a meticulously optimized fabrication protocol. Despite such rigorous optimization, the inherent physical variations on the fabrication process can still lead to fluctuations in resistance measurements [42], highlighting the fragile nature of this method and underscoring the imperative need for solutions aimed at enhancing reproducibility, emphasizing the importance of both precision in the fabrication process and the pursuit of innovative strategies to ensure the reliability of Josephson junctions.

Having delineated the fabrication process, we now turn our attention to the optimization of electron beam lithography (EBL) through the simulation of electron trajectories. To elucidate the interaction between the electron beam and our sample, we employed Casino [70, 71] software for simulating the trajectories of electrons. Utilizing the Monte Carlo method for these simulations allows us to integrate the findings directly into our fabrication strategy. In the software, we define a bi-layer resist over a Si substrate and their respective material properties. The initial layer is composed of an MMA co-polymer, with a density of 0.80 g/cm^3 and a thickness of 500 nm, followed by a second layer of PMMA, having a density of 1.14 g/cm^3 and a thickness of 230 nm. The chosen substrate is silicon (Si), with a density of 2.33 g/cm^3. Data was gathered through the simulation of 2 million electron trajectories, employing a beam radius of 10 nm and beam energy of 30 kV.

4.2.1 Point Spread Function

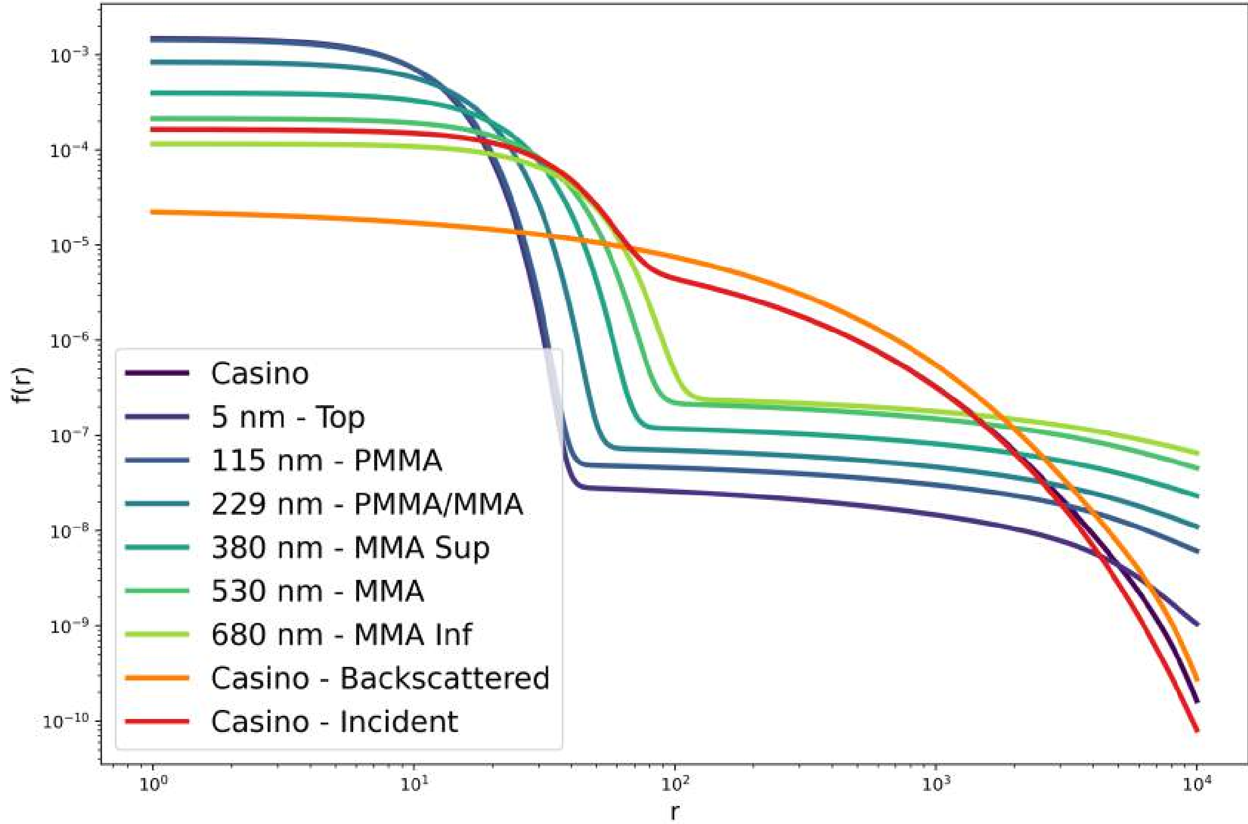

Figure 4.15: Point spread functions calculated via Casino and Urpec or Raith e-line commercial software. The Casino simulation resulted in three PSF (Full, only backscattered, only incident). The raith software allows for the PSF to be calculated at any height within the resist stack.

The point spread function[72] (PSF) is calculated by fitting spatial distribution of the electron beam intensity as it is focused onto the sample surface. This spatial distribution is calculated using Monte Carlo simulations of electron trajectory. The electrons are given a starting energy and random poisition within the specified beam radius. We used a beam radius of 10 nm, and 30kV electron energy in our simulations. The PSF also takes into account sample composition, by indicating chemical makeup and density of resist(s) and substrate. The PSF describes how the beam intensity is distributed around a point on the sample, and it is crucial for determining the achievable resolution and pattern fidelity in the nanolithography process. Understanding the PSF helps in optimizing the system parameters to achieve the desired lithographic features.

The equation is given by :

$$PSF(r) = \frac{1}{\pi(1+\eta_1+\eta_2)}\left(\frac{1}{\alpha^2}e^{-\frac{r^2}{\alpha^2}} + \frac{\eta_1}{\beta^2}e^{-\frac{r^2}{\beta^2}} + \frac{\eta_2}{24\gamma^2}e^{-\sqrt{\frac{r}{\gamma}}}\right) \tag{4.1}$$

Here, α represents the reach factor of incident electrons, which determines the extent to which incident electrons interact with the sample. β is the reach factor of backscattered electrons, indicating how far backscattered electrons can travel within the sample. η_1 is the ratio between backscattered electrons and incident electrons, providing insights into the scattering behavior. The parameters γ and η_2 are introduced to account for phenomena not adequately described by the double Gaussian method typically used to model electron beam scattering.Understanding these parameters is crucial for optimizing electron beam lithography processes and improving the resolution and fidelity of pattern transfer onto the sample.

Based on the results of the Monte Carlo simulations, parameters such as the reach factors (α and β), the ratio of backscattered to incident electrons (η_1), and additional parameters to account for other scattering phenomena (γ and η_2) are estimated. These parameters are used to develop a mathematical model for the PSF. Using the estimated parameters, a combination of two Gaussian distributions and to account for the spread of the electron

We calculated the PSF function for our specific resist stack (Si - 500 nm MMA - 230 nm PMMA) in two different ways. One using open source Casino [70, 71] simulation software which outputs a .dat file which can then be used by Urpec [73] matlab package to calculate the PSF. Another way is to use commercial proximity correction software provided by Raith with the e-line system. The Casino simulation calculates the dose distribution on the substrate, the e-beam software however calculates this for a specific height within the resist stack. It is important to note these curves are normalized. For the Casino simulation we also calculated the difference between incident and backscattered distributions. On the Raith software we calculated the energy distribution in 6 points thought out the resist stack. The results agree to some extent, as the Casino simulation would be equivalent to the raith simulation near the substrate. These curves are normalized and the Casino simulations have a wider range and different number of bins. Therefore some difference is expected, nonetheless the Raith simulation and Casino simulations agree for the first one hundred nanometers as seen on the Figure 4.15.

4.2.2 Proximity Effect Correction

The electron beam proximity effect refers to the distortion of patterns created by an electron beam lithography system due to the interaction of the electron beam with the substrate and previously exposed areas. This effect can lead to a blurring or widening of features, reducing the resolution and fidelity of the lithographic process.

Proximity effect correction (PEC) techniques are used to mitigate these distortions and improve the accuracy of pattern transfer. One common approach is to model the electron scattering and secondary electron generation in the substrate, then apply corrections to the exposure dose based on this model. PEC algorithms aim to optimize the exposure dose for each point on the substrate to compensate for the proximity effect, resulting in sharper and more accurate pattern transfer.

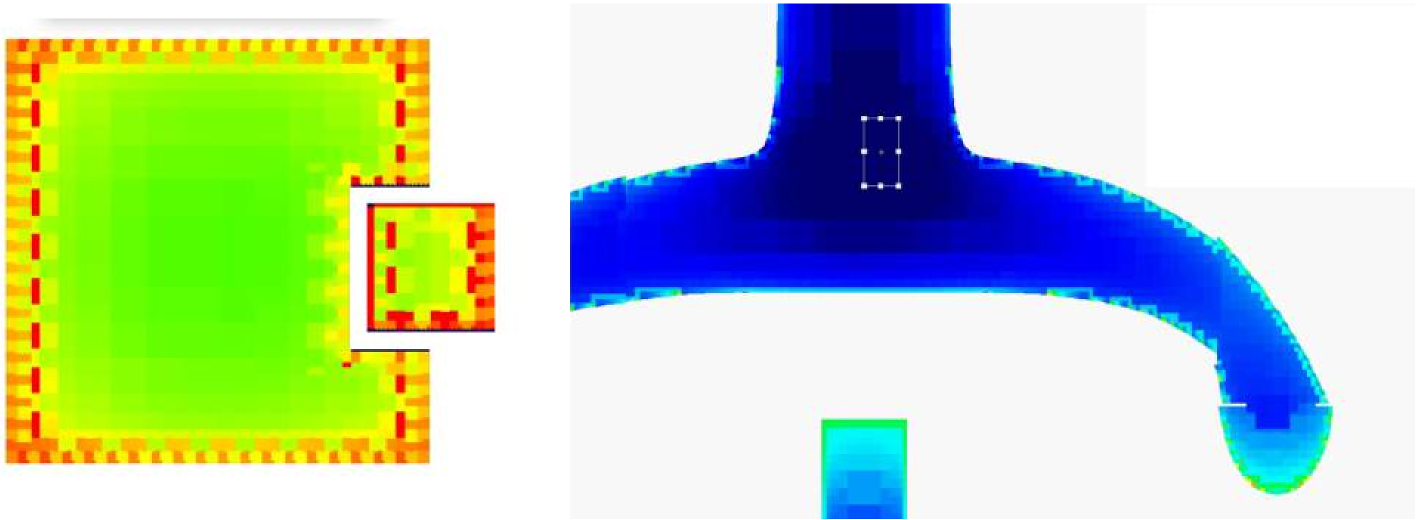

Figure 4.16: On the left a square next to a bigger polygon, and it is noticeable how the small feature affects the big one and vice versa. The dose distribution is aimed at making up for this issue and making the dose more homogeneous throughout the geometry. On the right PEC applied to horseshoe junction pattern. This distribution is created to minimize pattern distortion.

4.2.3 Integrating the PSF Over Josephson Junction Lithography Patterns

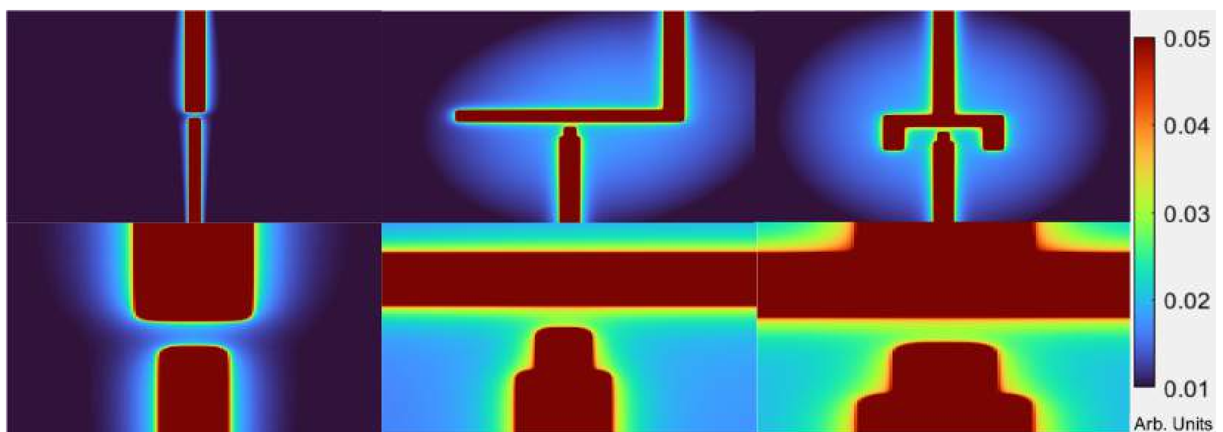

Figure 4.17: E-beam Pattern integrated with the PSF, and a 10 nm step size. From left to right: thin Dolan, L and horseshoe patterns. The color diagram is with respect to dose intensity in arbitrary units. Exposed regions received the same dose for all patterns, furthermore integration was done over an area of 10 μm x 10 μm, with a respective step size of 10 nm for all geometries.

As discussed on section 4.3 here we show additional results from the PSF integration. We integrated the dose distribution described by the PSF over distinct geometries resulting and the dose distribution maps seen on 4.17. Here we see the thin Dolan L and horseshoe junction, with a zoomed in view of each junctions unexposed area. It strikes the viewer immediately that both the horseshoe and L junction have

a large circular dose distribution over the central parts of its geometry. It is important to note that the applied dose over each geometry was the same, however the exposed region causes a background dose effect. Which we attribute to holding special significance in the outcome of the process. We believe that this should be optimized to be specifically covering the Josephson junction area instead of larger regions, where this background dose serves no purpose.

We start by showing our main results, on the fabrication of josephson junctions, a paper published in the Nanomaterials Journal.

4.3 Nanofabrication results on Josephson Junctions

To elucidate the role of backscattered electrons, the distribution of energy was analyzed with respect to both the scattering angle, as depicted in Figure 4.18a, and the radius of energy distribution, as shown in Figure 4.18b. The analysis revealed that the scattering angle's energy deposition is best modeled by a normal distribution, with the most probable scattering angle centered around $\mu \approx 43 \pm 17°$. However, electron scattering occurs throughout the beam's path, necessitating an examination of the cumulative effect of this scattering, represented by the radius of the backscattered energy surface. Through fitting the data to a power-law decay, described by the relationship Energy = $a \cdot \text{Radius}^{-b}$, we derived the equation $\text{E(r)} = 1.13 \times 10^{-4} \cdot r^{-0.77}$ to characterize the energy distribution's decay. The analysis of this distribution indicates that while incident electrons exhibit a well-defined resolution, backscattered electrons influence a broader region. This observation aligns with expectations, as the electron beam is being focused down to a 10 nm radius and is subsequently dispersed in all directions upon scattering giving origin to the backscattered electrons.

The observed decay profile stems from longer wavelengths inherent in low-energy electron beam lithography, leading to superficial scattering effects. The implications on patterning can be determined through comparison of this decay profile with the dimensions of the features targeted for patterning. Farther from the beam, distribution becomes approximately constant. We show this effect plotting the backscattered energy surface distribution in three dimensions as a simplified model, aligning it with the cross-section of the exposure pattern diagram. This method qualitatively displays the cumulative energy distribution's decay along the junction area, as shown in Figure 2c.

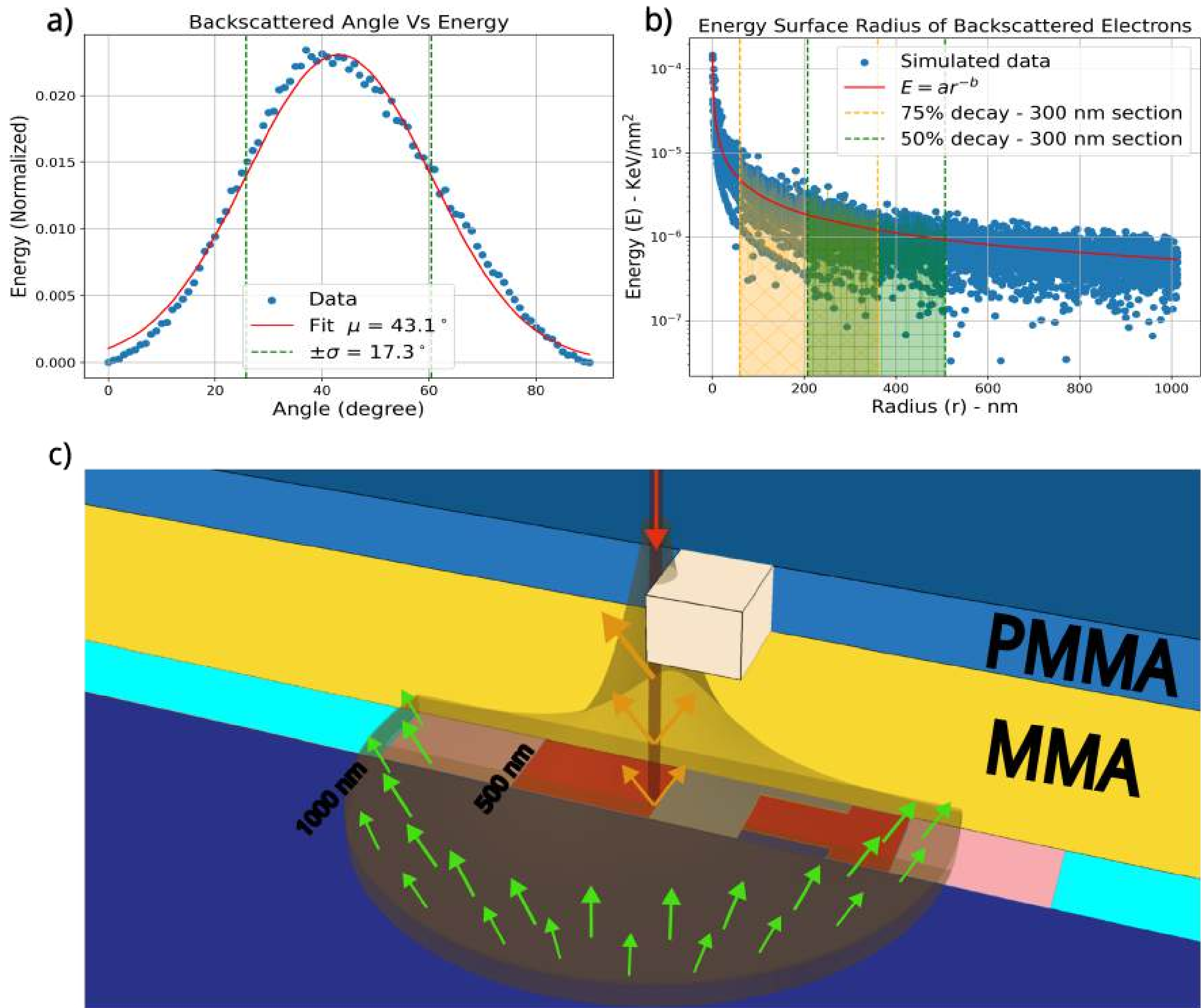

Figure 4.18: Statistical analysis of simulated backscattered electron trajectories illustrating the correlation with angle and radius, accompanied by a schematic representation of the energy surface. a) Simulated backscattered energy versus angle, with the green dashed line indicating the 2σ confidence region. b) Radius of the deposited energy surface for backscattered electrons as determined by simulation. First 300 nm section to be within resist material selectivity threshold is from 60 to 360 nm where the fitted backscattered energy will decay 75% from start to end, region is shaded in orange. Comparative 50% decay region in shaded in green. c) The energy surface of backscattered electrons (orange shade) surrounding the incident beam (red), integrated into a cross-sectional diagram of the bridge region. The pattern areas within 500 nm of the bridge section are highlighted in red, and areas within 1000 nm are shown in light red. Red arrow depicts the beam incident direction, orange arrow shows electrons backscattered within the resist stack, green arrows indicate backscattered electrons permeating from within the substrate.

The analysis of dose deposition by backscattered electrons provides crucial insights into the challenges associated with applying doses near the unexposed bridge region, which can lead to significant deformation due to the uneven spread of the applied dose. To mitigate the need for large doses in the vicinity of the junction area, it is essential to design geometries that strategically enhance the incidence of backscattered electrons. This approach aims to administer smaller, yet more uniform doses to the resist stack in the junction area from distributed regions. By comparing different geometries, we demonstrate how achieving a uniform dose distribution, or "saddle homogeneity," is key to enhancing the robustness of the process against variations.

To establish a reference for tolerance to variations in the fabrication process, we selected three different geometries to evaluate the dose-dependent room temperature resistance. The tested geometries are illustrated in Figure 4.19a. We fabricated multiple samples with doses varying progressively from underdose to overdose, adjusting the design using proximity correction software. Standard test pads were created to minimize variations in process parameters, ensuring all junctions are produced within the same chip, subject to the same conditions. We applied a varying dose from 350 to 870 μC/cm^2, at 20 μC/cm^2 intervals. Each geometry started with a dose low enough to reveal the exposure pattern, but not high enough for the bridge structure to form, resulting in measured resistance equivalent to an open circuit. As we proceed to measure junctions exposed at higher doses, the bridge structure begins to form, and a measurable resistance emerges. At first resistance is very high because the bridge gap is small. This indicates the first junction measurements begin with the highest possible resistance and smallest junction area. As the dose increases it wears down both the PMMA and MMA, increasing the dose in unexposed area and widening the gap, leading to a decrease in measured resistance. Once the dose deposited in the bridge region is high enough to compromise the PMMA bridge structure, it breaks and ceases to cast a shadow, allowing the top aluminum layer to form a closed circuit, culminating in a short measurement. In this manner we defined dose window starting from the first junction which resulted in a measurable resistance to the last.

To analyze the results, we present in Table 4.4 the dose window within which measurable resistance was obtained for each analyzed geometry. For these geometries, the dose range for which a bridge structure forms is 260 ± 10 μC/cm^2 for the horseshoe and 160 ± 10 μC/cm^2 for the L junction. In contrast, the thin Dolan structure exhibits stability within a narrower span of only 20 ± 10 μC/cm^2 implying only one dose resulted a measurable resistance. Such a limited dose window for the thin Dolan design significantly reduces the process's success rate. Minor changes in temperature or development time could render the samples unusable. Furthermore we see that Horseshoe reproducibibility is at 96% while the L junction 83%. Although there is a notable difference in the standard deviation, the process was repeated in different facilities with similar reproducibility. We attribute this difference to the properties of the local EBL systems.

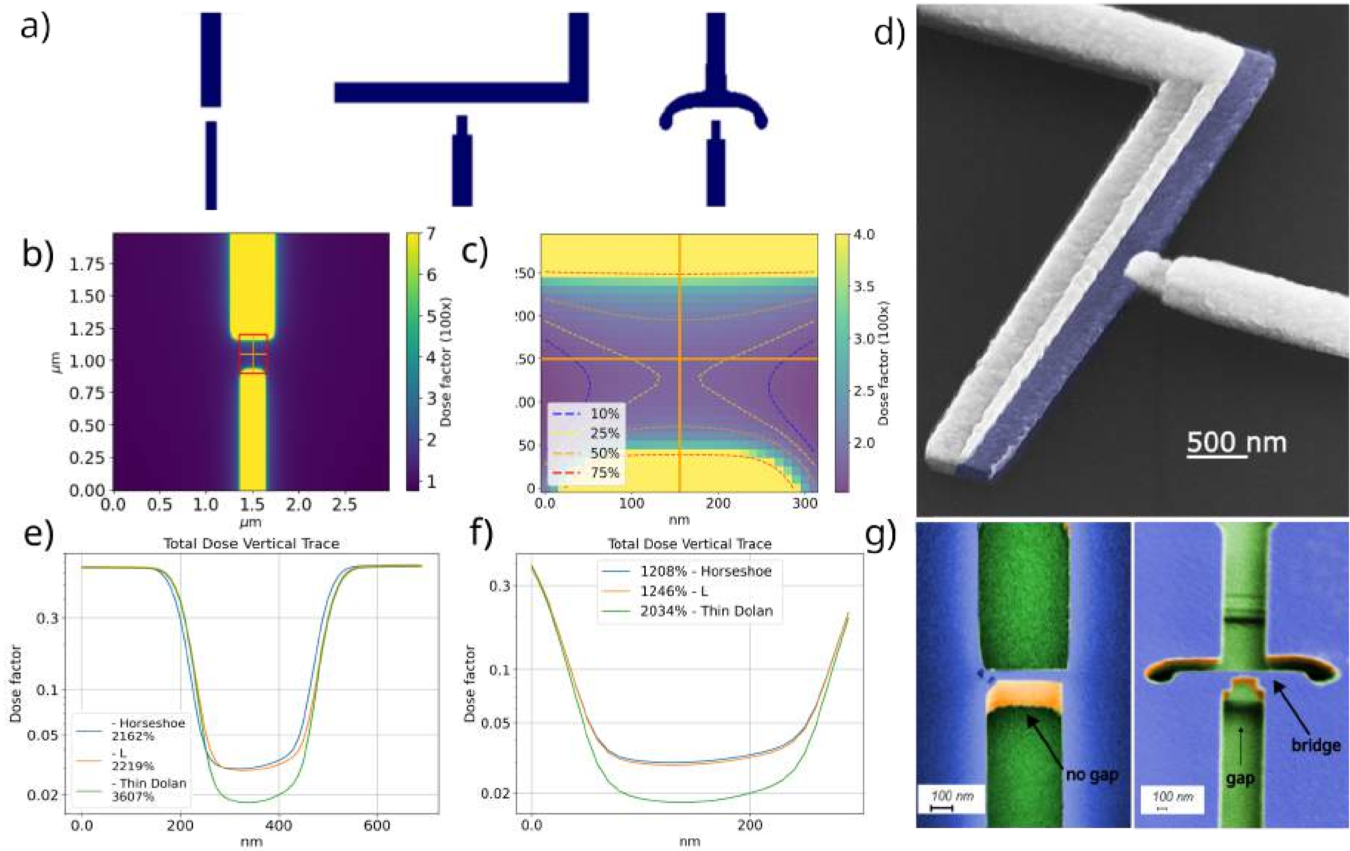

Figure 4.19: a) Designs employed to investigate the effects of backscattered electrons across different geometries, identified from left to right as: thin Dolan, L, and horseshoe junction designs; b) Resulting dose map from the integration of the Point Spread Function (PSF) over the thin geometry, with detailed analysis presented in panels (e) and (f). c) Detailed view of the unexposed bridge region, with percentiles marking the total deposited dose per region; (d) Colored scanning electron microscope (SEM) image of an L-shaped Josephson junction, where the blue region indicates the first deposited aluminium layer, and the AlO_x tunnelling barrier is highlighted in the center; e) Total dose distribution profiles along vertical trace, including some of exposed region (200 nm on each side), f) only 300 nm unexposed section, for horseshoe, L and Thin Dolan geometry - percentiles here denote the range of maximum dose variation; the percentages on the legend in (e) and (f) are ratio of energy deposited in the directly exposed areas to the indirectly exposed gap. (g) Angled coloured SEM images showcasing the resist stack; on the left, the Thin Dolan pattern is inscribed without bridge formation, whereas on the right, the horseshoe pattern is exposed, clearly displaying the bridge structure. Green indicates Si substrate, blue PMMA resist surface and orange for resist side walls seen at an angle.

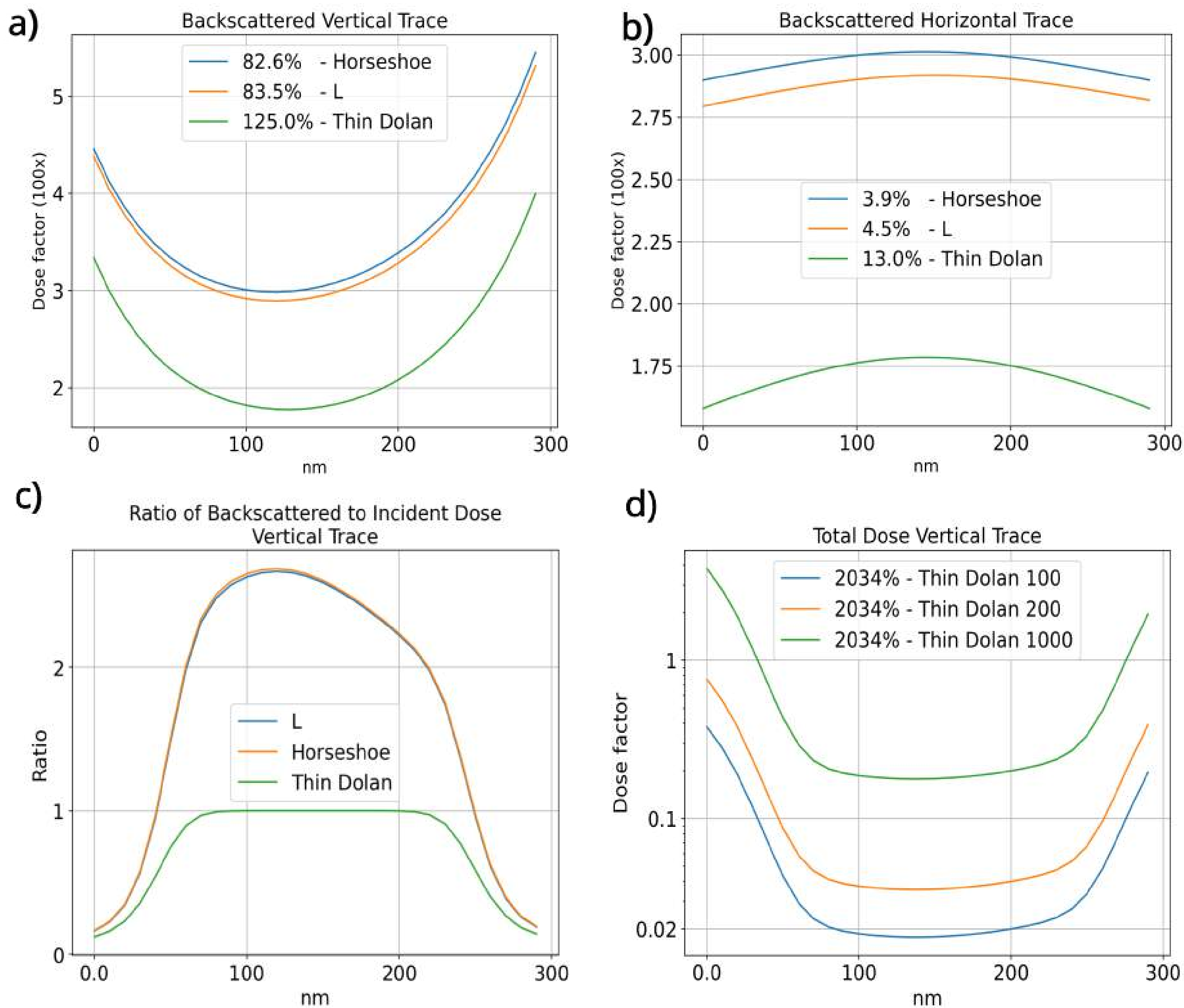

Figure 4.20: Analysis of dose factors and the ratio of backscattered to total incident dose for various geometries investigated in this study. a) Distribution of backscattered electrons along a vertical trace; b) Distribution along a horizontal trace; c) Ratio of backscattered to incident dose over the vertical trace. d) Dose variation observed in a thin Dolan geometry.

To gain insight into the dose distribution across the junction area, we employed the Point Spread Function (PSF) [72], by using the distributions derived from Monte Carlo simulations (Casino) and applying a MATLAB open source package Urpec [73]. We then integrated PSF over the exposed geometries using a step size of 10 nm, we calculated the deposited dose within a 10x10 μm area, a close up is depicted in the dose distribution plot in Figure 4.19b. A detailed examination of the unexposed bridge region is showcased in Figure 4.19c, where orange lines represent vertical and horizontal traces without exposure.

Table 4.4: Experimentally defined reference for process tolerance per geometry. Reproducibility standards for geometries which have been thoroughly tested. Standard deviation for room temperature resistance.

Junction Type	Supported dose variation($\mu C/cm^2$)	Reproducibility (Yield)	Std Deviation
Thin Dolan	20 ± 10	Not reproducible	-
L shape	160 ± 10	83 % (20/24)	3.2 %
horseshoe	260 ± 10	96.3% (26/27)	31.7%

Further analysis of these traces enabled us to characterize the distribution of the total applied dose across various geometries and conditions. The noted asymmetry in the saddle-shaped energy distribution can be ascribed to one side of the junction being wider, facilitating a seamless contact between the upper and the oxidized (purple) lower layers of the Josephson junction, as demonstrated in the SEM angled image of the L-type junction (Figure 4.19d), where the upper layer is observed making a clean and smooth contact with the lower layer.

To understand why the L and horseshoe are reproducible while the Thin Dolan design is not, we begin by examining the ratio of energy deposited in the directly exposed areas to the indirectly exposed gap, shown in Figure 4.19e. From this graph we can see that the exposed regions are subject to the same dose, however a sharp decrease in total deposited dose from 0.6 to less than 10% of this value for all geometries. A more detailed examination of the unexposed region, shown in Figure 4.19f, indicates the total dose within 300 nm of the bridge section changes approximately 12 times for the most effective geometries, the horseshoe and L, and 20 times for the thin Dolan, which exhibits a lower success rate. Assuming the same dose is necessary for gap formation, the thin Dolan structure necessitates a higher geometry dose factor to modify the solubility the MMA layer, leading to pattern formation before the bridge structure, it is noticeable in the SEM image on Figure 4.19g (left). This implies that a higher dose will also be deposited on the top PMMA layer, which is undesirable, as it weakens the bridge structure, causing some to break while others become narrower, thus reducing the reproducibility of Josephson junctions. To mitigate this issue, we investigate geometry-dependent designs to explore how the backscattered electron distribution to selectively modify the solubility the MMA resist.

Taking a closer look at the disposition of only the backscattered electrons for the 3 geometries (Figure 4.20a-b), we show that the Horse and L geometries have more homogeneous backscattered electron distribution than the Thin Dolan geometry. Furthermore, it can be noted that the Horse and L junction have over 50% more dose deposited over the bridge area. Showing that a smaller dose near the junction area is needed to form the bridge structure, preserving the PMMA structure for the reasons stated previously. This can be seen in Figure 4.19g (right) where patterned resist for the horseshoe junction has a clear gap formed.

To further understand the impact of the incident electrons which may undergo forward scattering and drift from their point of incidence, we integrated the Point Spread Function (PSF) excluding the backscattered terms to analyze the distribution of incident energy and calculated the ratio of deposited dose between incident and backscattered electrons, denoted as E_b/E_i.

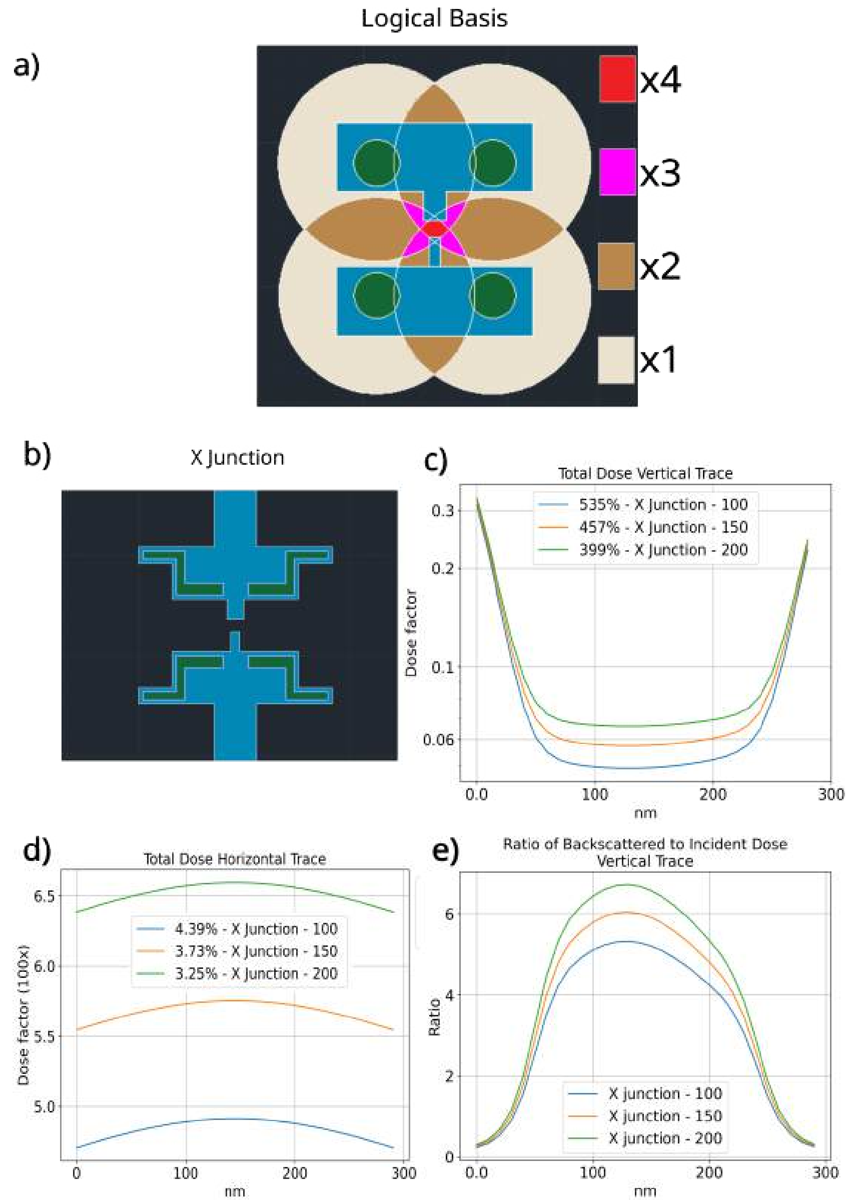

Figure 4.21: Analysis of dose factors and the ratio of backscattered to total incident dose for proposed geometry designed to utilize backscattered electrons for undercut definition. a) The logical basis to create a new geometry, specifically conceived to tailor the distribution of backscattered electrons, thereby minimizing variance across the junction area. The blue region is intended to receive the minimal necessary dose to develop the top resist layer, with backscattered electrons being generated within the green circle region by a higher dose factor. The larger circles represent a simplified model for the overlap of backscattered regions, assuming point sources, with different colours indicating the degree of overlap. b) X junction Geometry designed with features to retain geometric resolution while achieving the (4:1) ratio for the c) total deposited dose over the vertical trace. d) Horizontal profile of the total deposited dose. e) Ratio of backscattered to incident dose for the X junction.

Figure 4.20c illustrates this ratio along the vertical orange line traversing the bridge area, as shown in Figure 4.19c. From the behaviour of E_b/E_i in the bridge region for the three geometries observed, the contribution of backscattered electrons is at least twice as much as the dose deposited by incident electrons alone in the central part of the bridge region for the horseshoe and L-shaped designs. While, for the thin-Dolan design, this ratio in the vicinity of the bridge's central part exhibits a comparable effect.

Table 4.5: Table displaying simulated dose variation, in the unexposed horizontal and vertical traces of the junction area. Variations along traces are calculated dividing maximum by minimum dose value. Max ratio is defined by comparing backscattered to incident dose along the vertical trace.

	Total Vertical	Total Horizontal	Backscattered Vertical	Backscattered Horizontal	Max Ratio
Thin Dolan	2034%	13.0%	125.0%	13.0%	1
L	1246%	11.1%	83.5%	4.5%	2.7
Horseshoe	1208%	3.9%	82.6%	3.9%	2.7
X Junction (100)	535%	4.4%	37.3%	4.7%	5.3
X Junction (150)	457%	3.7%	32.0%	3.7%	6.1
X Junction (200)	399%	3.3%	28.1%	3.3%	6.7

Figure 4.20d displays the total dose deposited by the incident beam in the bridge region for different base doses within the thin Dolan geometry. An increase in the base dose outside the bridge region elevates the total deposited dose within the bridge area as anticipated but does not alter the dose ratio between the regions outside the bridge and its central area. Consequently, a higher base dose intensifies the dose deposited throughout the entire resist stack, diminishing the bridge's stability.

Simulations indicate that an optimized geometry should have enough exposed area within a 4 μm radius of the junction area to eliminate the need of increased dose around the region of the bridge, which can cause the PMMA bridge structure to deteriorate. As a means to elucidate our findings pragmatically, we propose a innovative e-beam lithography technique in two steps. We suggest geometry should be optimized in resolution first rather than undercut. Once a a base dose for the geometry is found, strategic places are used to engineer the correct backscattered electron dose. A schematic of such a configuration is depicted on image Figure 4.21a. The blue region receives the constant base dose, while the four green zones receive higher doses to create backscattered electrons. If sources were point-based and equidistant from the junction area, they would overlap with maximum interference over the unexposed junction region. Based on this logic we created four regions, however to avoid extreme doses, we increased the area (Fig. 4.21b). Simulations showed that by raising the dose on the backscattered electron regions, the bottom of the vertical trace is modulated while creating negligible effects on the border, making the whole length of the bridge region maintain a 400% dose variation or less (Fig. 4.21c). It should be noted that this distribution will remain constant for this geometry as long as the dose on the backscattered electron region is twice the base dose. The horizontal trace of the bridge area is plotted (Figure 4.21d,e). The ratio of backscattered to incident dose in Figure 4.21e is significantly higher compared to previous junctions, and this geometry allows control over this ratio, providing an efficient means to precisely control the undercut to increase overall Josephson junction reproducibility. Although it has not been tested we believe designating zones to produce backscattered electrons is a promising means of increasing success rate in junction fabrication. Furthermore a complete description of simulated dose distributions for the unexposed region of the junction are displayed on Table 4.5, where we show total and isolated backscattered dose variation along vertical

and horizontal traces for all simulated results. Information on the contribution of sideways scattered incident electrons, can be inferred from the ratios along the vertical traces. Incident dose is the main source of dose at the very edge of the unexposed regions however it diminishes greatly within the first tens of nanometers, showing that for any geometry the backscattered electrons are the main source of dose deposition at approximately the center of unexposed regions, from where the max ratio value is derived.

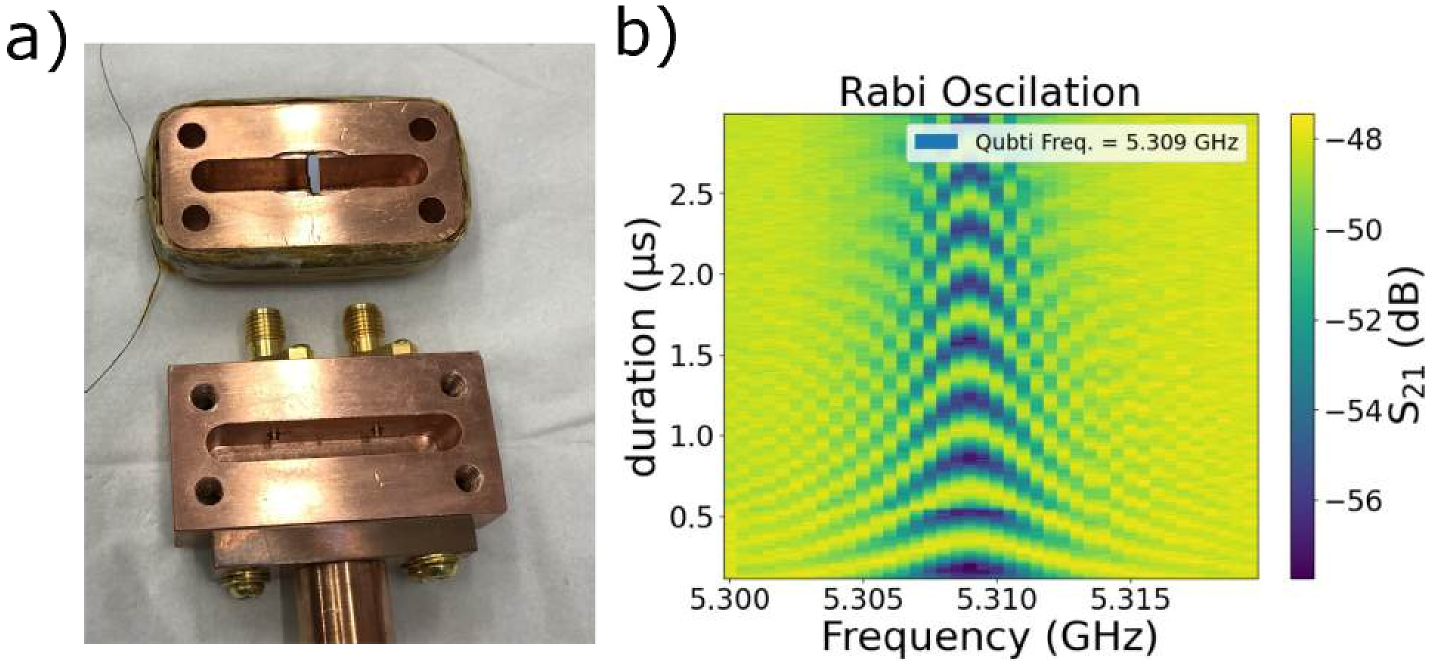

Figure 4.22: a) 3D copper cavity, on the top half a silicone chip is seen where the transmon has been deposited. b) Quantum Rabi Map provides a profile of the dynamic evolution of qubit states in a time-dependent landscape.

As a proof of concept, we successfully fabricated and analyzed a qubit within a (3D) cavity displayed on Figure 4.22a. The qubit construction involved L-shaped junctions, similar to the ones shown in the scanning electron microscope (SEM) image in Figure 4.19d. They were integrated into a SQUID with the rectangular en-looped area of (23x90) μm^2 enclosed by two capacitive plates (300x800) μm^2. This device was placed in a 3D cavity and mounted onto the cold plate of a Dilution refrigerator. The cavity and qubit frequency were measured at 7.389 GHz and 5.309 GHz respectively. In the course of our characterization, we observed Rabi Oscillations displayed on Figure 4.22b and key performance metrics for the qubit. The relaxation time (T_1) was measured at 14.3 ± 0.4 μs and the coherence time (T_{2^*}) was measured using the Ramsey protocol at 1.0 ± 0.1 μs. These characterizations provide evidence of the functionality and quality of the created Josephson junctions composing the qubit within the 3D cavity. This specific sample was fabricated by graduate student Gustavo Moreto as part of his Masters Thesis.

4.3.1 Partial Conclusion and Discussion

This study provides a comprehensive investigation into the fabrication of Josephson junctions using 30 kV e-beam lithography. We address the critical role of backscattered electrons in the fabrication process, emphasizing the importance of controlling their distribution. Our analysis established a parameter to define dose stability, which agreed with the experimentally obtained reproducibility standards of three different lithography patterns. Through simulations we demonstrated that for conventional one-step 30kV EBL for Dolan technique, some geometries achieve more uniform dose deposition than others, affecting junction stability and performance. We developed a systematic means of analyzing simulation results which allowed us to separate incident from backscattered contribution, which underscored the geometric effect on dose distribution.

As our simulations revealed the strategic control of backscattered electrons can indeed lead to a more uniform distribution of dose deposition. Distinctively showing a possible reason for some geometries to yield higher than others. On Table 4.5, geometries are ordered from least to most homogeneous, establishing a pattern to be followed. Enabling us to propose not only a new geometry, with the intent of mitigating the issues raised along the article.

The results made it evident low energy EBL needs especial consideration of backscattered electrons distribution. Simulation techniques, such as those detailed in this study, are instrumental in determining if a given exposure pattern incorporates sufficient backscattered contributions to create controlled undercuts. This technique is not only a notable contribution to Josephson junction fabrication, but also to many other lithography processes which require undercut engineering and control. To highlight our conclusions we provided a geometric example that has built in regions strategically for backscattered electron generation. These zones are used to apply a controlled homogeneous dose over the junction area, mitigating the challenges associated with the fabrication of bridge-like structures. While the effectiveness of this geometry has not been tested, it serves as possible direction for continued research. Josephson junctions are devices with great innovative potential, and our research democratizes their production, making it more accessible to fabricate Josephson junctions reliably using 30 kV EBL systems.

4.4 Further Results on Josephson Junctions

This section of the thesis is focused on presenting and analyzing the results of our study. Specifically, we start by providing an overview of the results achieved through the simulation techniques described in the previous section. These simulations play a crucial role in optimizing the design of the devices under study and provide valuable insights into their performance characteristics.

Next, we provide a detailed account of the fabrication process used to create the devices, including any optimizations that were made along the way. This section will showcase the practical side of our research, highlighting the steps taken to create functional devices that can be used for experimental purposes.

Finally, we dedicate the third part of this section to discussing the experimental results achieved thus far. This includes any data collected through experiments performed on the devices and an analysis of the results obtained. By combining the results from simulations and experiments, we provide a comprehensive view of the performance of the devices and draw meaningful conclusions about their capabilities and potential applications.

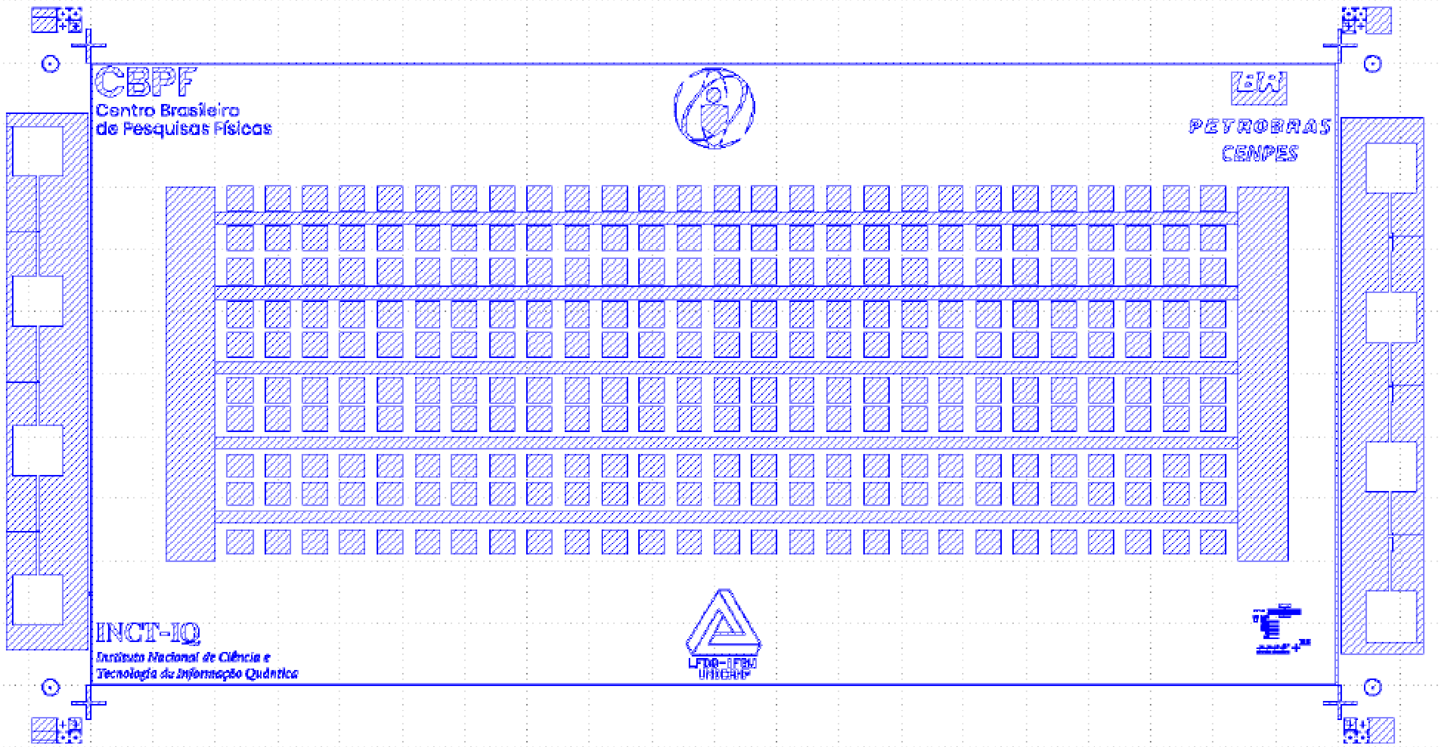

Figure 4.23: Circuit designed to measure 270 Josephson junctions. This enables to minimize variations which change from sample to sample. Isolating the properties of lithography process from the environment of perturbations due to temperature, humidity, process time and human error.

For successful optimization of Josephson junction fabrication process, the process must be isolated from the many parameters that can interfere with the final result. To make this process more efficient we chose to implement a circuit configuration to test a large amount of Josephson junctions. Essentially we could make the sample as large as we wanted, however for it to be conveniently adapted to our production pipeline. Therefore we wanted the circuit to fit within a 10mm by 5mm area. Therefore by placing these pads in the center of this area we managed to fit 27 columns by 10 rows, making a total of 270 pads. They are engineered for one side to be connected to all junctions and 270 isolated pads. Measuring is dynamic on this circuit as only one probe needs to be moved to test the next junction. process time and other variations which occur from sample to sample can mask the effects of variations in other parameters. This circuit enabled fair comparison of different lithography parameters such as, geometry, dose, step size, PEC, shadow dosing, aperture and other patterning properties. Resulting in great advances in our lithography methodology, the circuit described is show in Figure 4.23.

4.4.1 Josephson Junctions Fabrication Procedure

The Josephson junctions in this study are all $Al/AlO_x/Al$ junction, fabricated through the Dolan method. This essentially consists of created a patterned bridge structure on an ultra flat surface, and depositing a thin film anisotropically to cast a shadow. The process can be visualized on the Figure 4.24.

For optimization purposes we fabricate Josephson junctions in test pads which enable dynamic probing to achieve a higher throughput. Conditions during process must be closely monitored, for our system vacuum conditions for the chamber were typically 5-8 x 10^{-6} mbar and gun vacuum 8-15 x 10^{-10} mbar. Junctions were created at 30 kV and typical current measurements were around 10 pico amps. In general room temperature and humidity were kept at 23 C° and 50%.

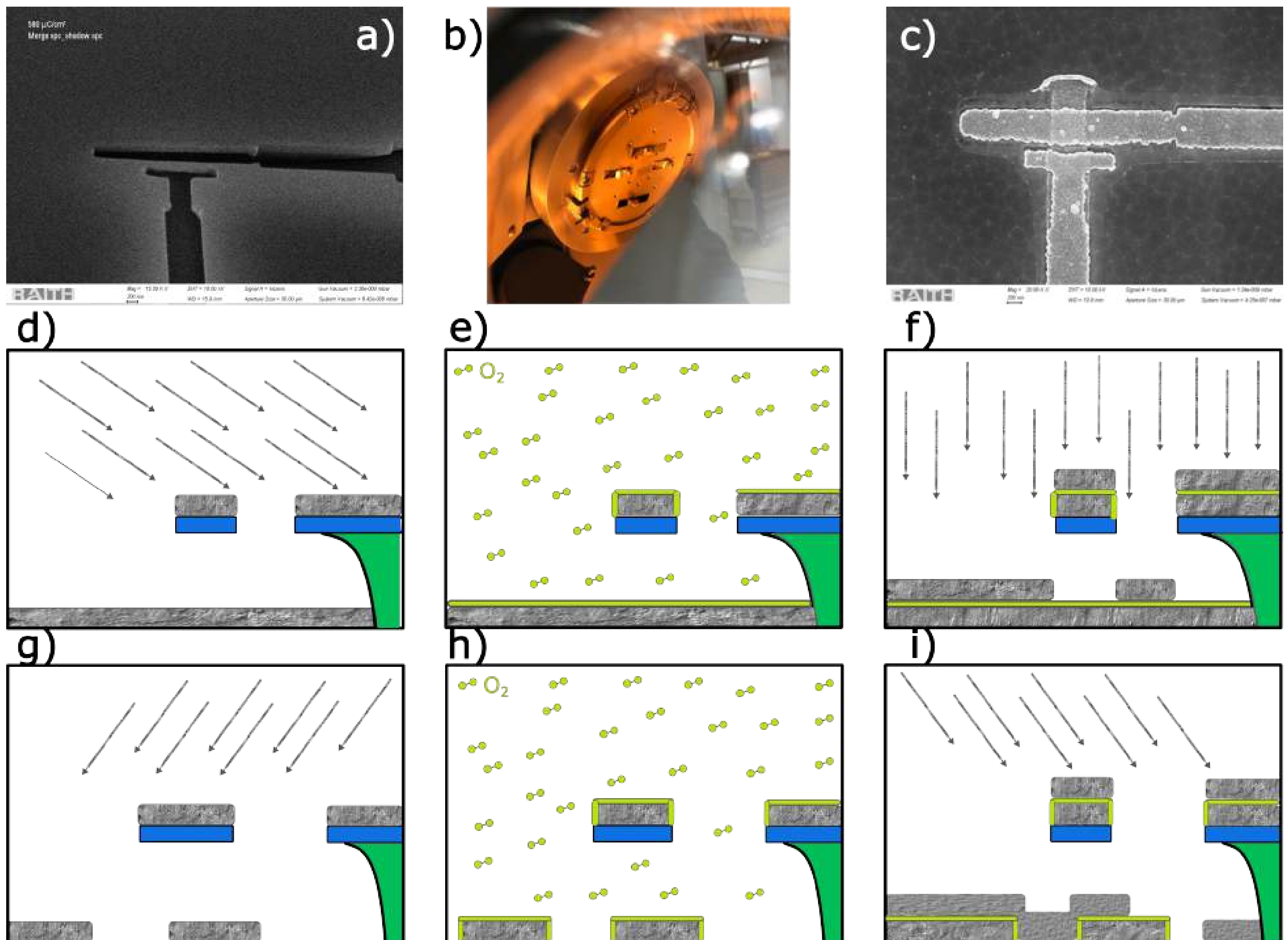

Figure 4.24: a) Angled SEM image of patterned resist with T type L junction prior to Al deposition, dark area in bridge region shows the undercut. b) Al e-beam vapor deposition (LFDQ), samples shown to be in angle, amber glow is seen from melted Al in the crucible below. c) SEM image of junction after double angle shadow deposition with the steps described on d-f. d) First deposition at 45° angle, e) oxidation in controlled atmosphere and f) deposition at 90 degrees to normal. g-i) Shows a small angle deposition of 30° (g), followed by oxidation (h) and finally a -30° depostion to form the contact over the oxide (i).

It should be noted that we tested using cold (17 C°) vs room temp 23 C° MMA and found that cold

resist was harder to remove both for development and lift off. To make resist thicker it can be used colder, or spun at slower speed. However the resist density is higher for colder resist. In all, we feeel this was a mistake and warn that using the speed to control height is a better option. One option to be investigated is spinning the PMMA at colder temperatures than the MMA to improve selectivity.

This paragraph is meant to describe general nano-lithography procedure for overlaying Josephson Junctions, these contribute with the sequential steps and particular settings which should be used.

Step	**Description**
Register Conditions	Register column pressure, chamber pressure, extraction voltage, room humidity, and temperature.
Set Z	Set Z height to 25 mm.
Beam Settings	Beam set to 30 kV, aperture 10 μm.
Beam Alignments	Align focus, astigmatism, aperture iteratively with higher magnification. Once 300,000x zoom is reached, it is possible to produce a contamination dot. Do final alignment procedure until resulting dot is round, even, and less than or equal to 20 nm diameter.
3 Point Alignment	Look for alignment marks and perform 3 point alignment. Repeat this process until you locate a point within your design that is distant from one of your markers and land exactly on it. The deviation from the desired location is proportional to overlay misalignment.
Final 3 Point Alignment	Once the design and chip are successfully matched, put the focus correction into place. This is done by creating a contamination dot at each of the flagged locations, set and save focus for each alignment position.
Write Field Alignment	Pick one of your three markers and perform write field alignment. It is crucial that the 3 point markers are not moved after this step is completed, or it will need to be redone.
Calculate Dose	Measure current and set step size to 4 nm. Calculate dwell time before running exposure.
Inspection	Resist can be inspected by using a thin layer of Au deposition and tilting the sample at 45 degrees. In this manner, the quality of the bridge can be assessed.

4.4.2 Dose Tests

E-beam recipes take into resist deposition parameters and lithography parameters. For resist it is important to take into consideration substrate, resist composition, resist speed and temperature during spinning, prebaking (time and temperature). This depends on the specific purpose of the lithography procedure. If more resolution is needed, thinner resists must be used. For etching, one layer resist will do. For thin film deposition onto a mono-layer of patterned resist, it is better to have double layer, with an undercut as this prevents material build up on the resist walls. Once these parameters have been chosen, the beam parameters must be optimized. These include but are not limited to aperture size, beam energy and beam

calibration. For 30 kV systems, calibration is user dependent and will affect the outcome. Once this is ready there are the patterning parameters to be considered such as: write-field size, beam step-size, patterning dynamics, PEC, beam dwell time and others. Finally the last optimization and arguably one of the most important is the dose test. Practically all parameters affect in some way the necessary dose to correctly transcribe the desired pattern. Therefore the pattern is exposed with a varying dose in order to meet resolution standards, or in case of Josephson junctions, the formation of bridge structures.

Here we analyze dose tests through angled SEM imaging. It is important to note that resist structures are sensitive to the electrons used to form the images, a nanometric layer of Au is deposited through magnetron sputtering, to mitigate charging and also offer some protection to the structures. This effect can be further mitigated by inspecting resist structures in low energy e-beam of 5 kV or less.

Through SEM inspection it is possible to state whether the bridge gap is forming, pattern properties allow imaging analysis to access the degree of deterioration suffered by the PMMA structure. Left over resist and poorly formed structures are indicative of underdosed exposures. While curved and stretched structures indicate overdosing, and deterioration. The desired properties of the lithography process, would be to find very defined undercuts, and very defined bridge structures.

We will start by the analyzing a dose test of the thin Dolan geometry (Fig. 4.25a) which is a particularly unsuccessful geometry. It is clear to see on Figure 4.25b very solid wall of resist is in the junction region. Therefore as we apply higher doses we see outcomes displayed and on Figure 4.25c-d, we see excessive thinning and a rupture point on the PMMA due to stochastic variations. This indicates the geometry does not favor the selectivity between resist layers as extensively explained on the previous section. On the third image, it there is a small visible opening at the bottom. On the next image (Fig. 4.25e) with a bit more dose, the bridge to breaks altogether.

Next we analyze a dose test over the L shaped junction (Fig. 4.26a) patterned resist images. The first SEM image, Figure 4.26b shows a zoomed out birds eye view of the L pattern, a closer view (Fig. 4.26c) shows the bridge has not formed for this dose, at a higher dose on Figure 4.26d it is possible to see the PMMA bridge structure, and at a higher dose still (Fig. 4.26e), it is possible to see the thinning of the bridge structure. The L geometry produces reasonably stable results, however for certain devices such as an Xmon qubit for example it is useful to have a more compact Josephson Junction, in its simplest form a Josephson junction can be a weak link in an otherwise straight wire. We tried many ways to make these 200 nm wide many times, with the best results being similar to what is seen on Figure 4.25. Once the L junction started to yield working Junctions, this raised the question as to why success was geometry dependent. In an attempt to understand this we proposed the horseshoe junction (Fig. 4.27a), which would indicate that success was related to how much area is exposed near the junction and how it is distributed. Here we see the bridge forms quite well as seen in the Figure 4.27b-c. From this view point we see no MMA left behind, however if it is seen from the back side, we can see the distribution is curved (Fig. 4.27d-e). As the dose rises for this pattern the side walls begin to to dissolve until the structure falls apart.

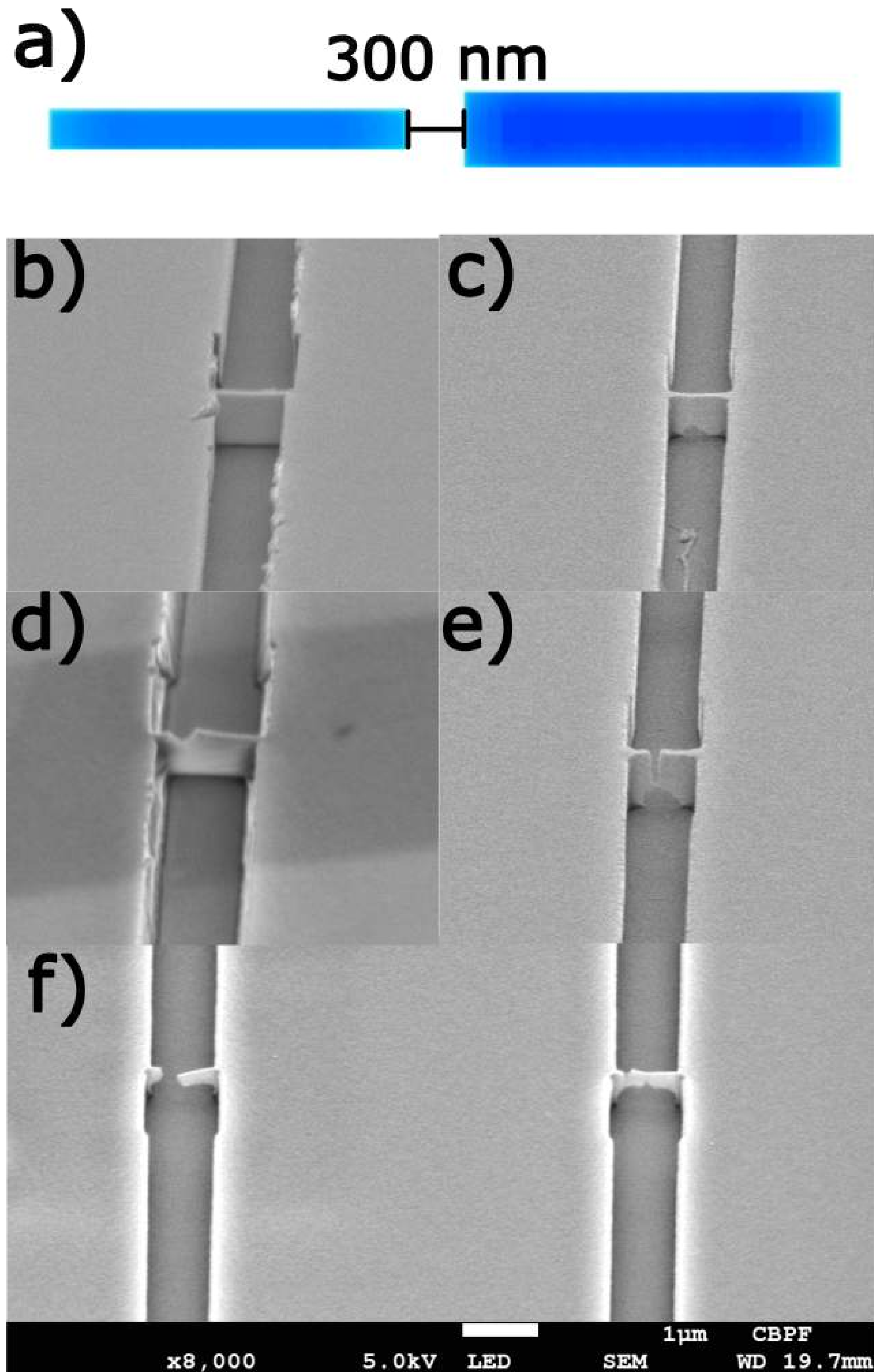

Figure 4.25: a) E-beam Pattern with applied PEC of thin Dolan junction, gap is shown to be 300 nm. b-e) SEM image of patterned resist with the Dolan junction Pattern, clearly shows teh full resist stack deteriorating. f) A particular sample where two dolan junctions were placed near each other ($4\mu m$) causing it to at least form a very brittle bridge pattern.

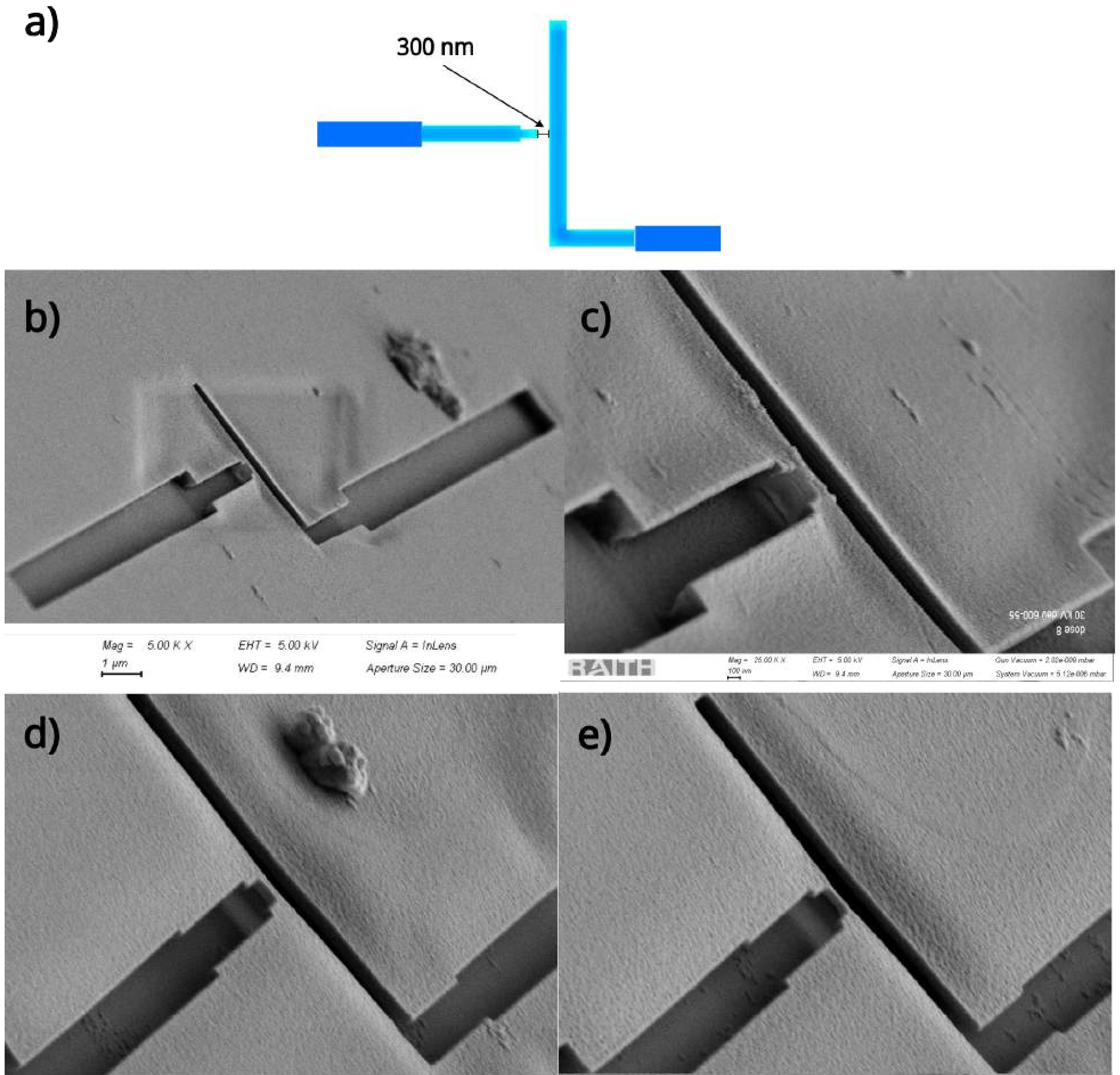

Figure 4.26: a) E-beam Pattern with applied PEC of L junction, gap is shown to be 300 nm. SEM images L junction pattern exposed onto resist, b) zoomed out image of whole exposed area, c) close up to underdosed exposure of the bridge structure. d) Bridge structure formation, e) bridge thinning due to increasing dose.

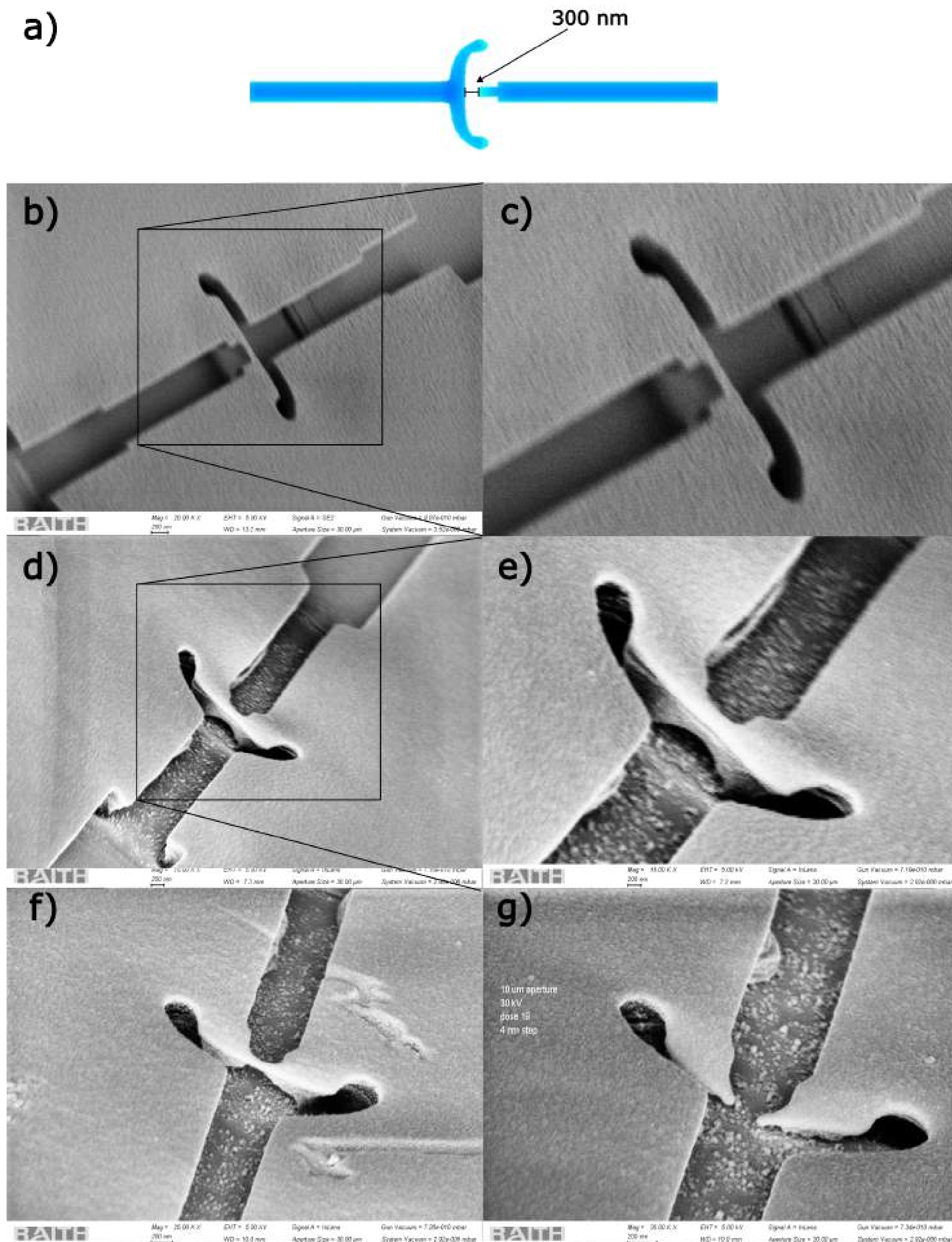

Figure 4.27: a) E-beam Pattern with applied PEC of horseshoe junction, gap is shown to be 300 nm. SEM images of patterned resist with the horseshoe junction pattern. b) Horseshoe junction from the contacting side, a clear gap is shown, with no MMA in the bridge region (c). Image (d) shows the view from the opposite side, here we see that the opening is has a curved shape (e). Now we look at how the opening widens as the dose is raised (f) until PMMA deteriorates (g).

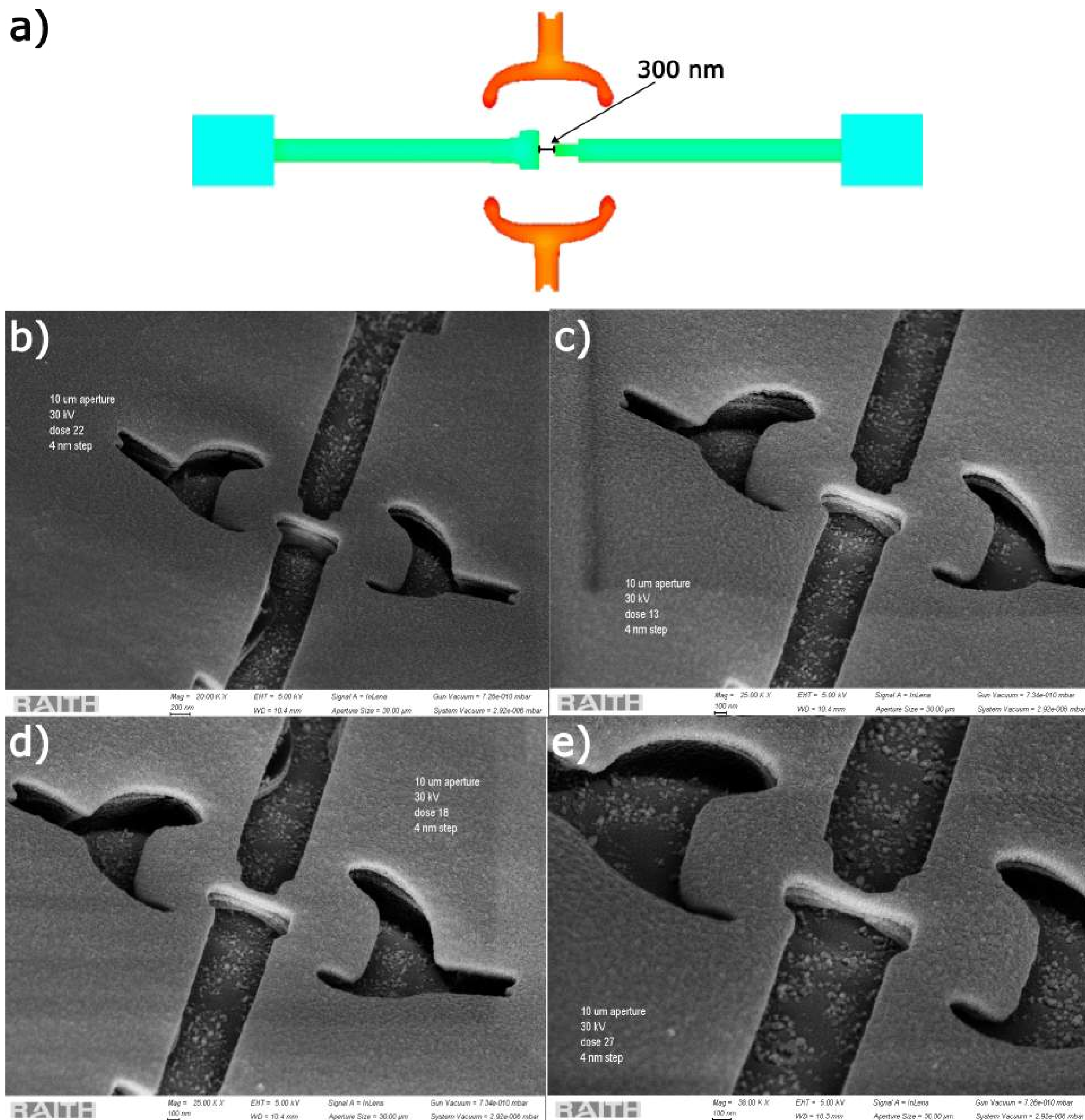

Figure 4.28: a) E-beam Pattern with applied PEC conceived to create backscattered electrons, from the sides. This geometry was intended to test the effect of nearby expositions to bridge gap formation. Here we keep the dose of the contacting geometries constant, while varying the dose of the side structures, progressively diminishing the MMA.b-e) SEM images of progressively higher doses being applied to the side structures.It is noticeable the technique causes bridge side walls to collapse, nevertheless proves that it is possible to produced backscattered electrons in regions far (up to 4 μm) from bridge structure.

Nevertheless to show full control over the fabrication process we are still investigating a reliable way to fabricate Josephson junction in its simplest form, a straight wire with an oxide barrier, without the side arms (horseshoe) or turns(L). To achieve this we attempted to add structures near the junction to provide enough backscattered electrons. While it did work in parts as shown on Figure 4.28, the side walls were affected. On the first image, a small gap can be seen however there is a large amount of MMA. By the last image it is entirely removed, unfortunately the whole surrounding structure which holds up the PMMA was also made soluble and was dissolved during development. This exposes the need of delicate engineering of backscattered electrons, which from this attempt we conclude that these regions must be strategically placed in front of or behind the gap and not to the sides. Another consideration is that perhaps smaller dimensions should be used. It seems feasible to have a very reliable process for 30 kV EBL, with higher reproducibility, as the inner workings are exposed, it becomes a matter of optimization.

4.4.3 Considerations on Angle of Deposition

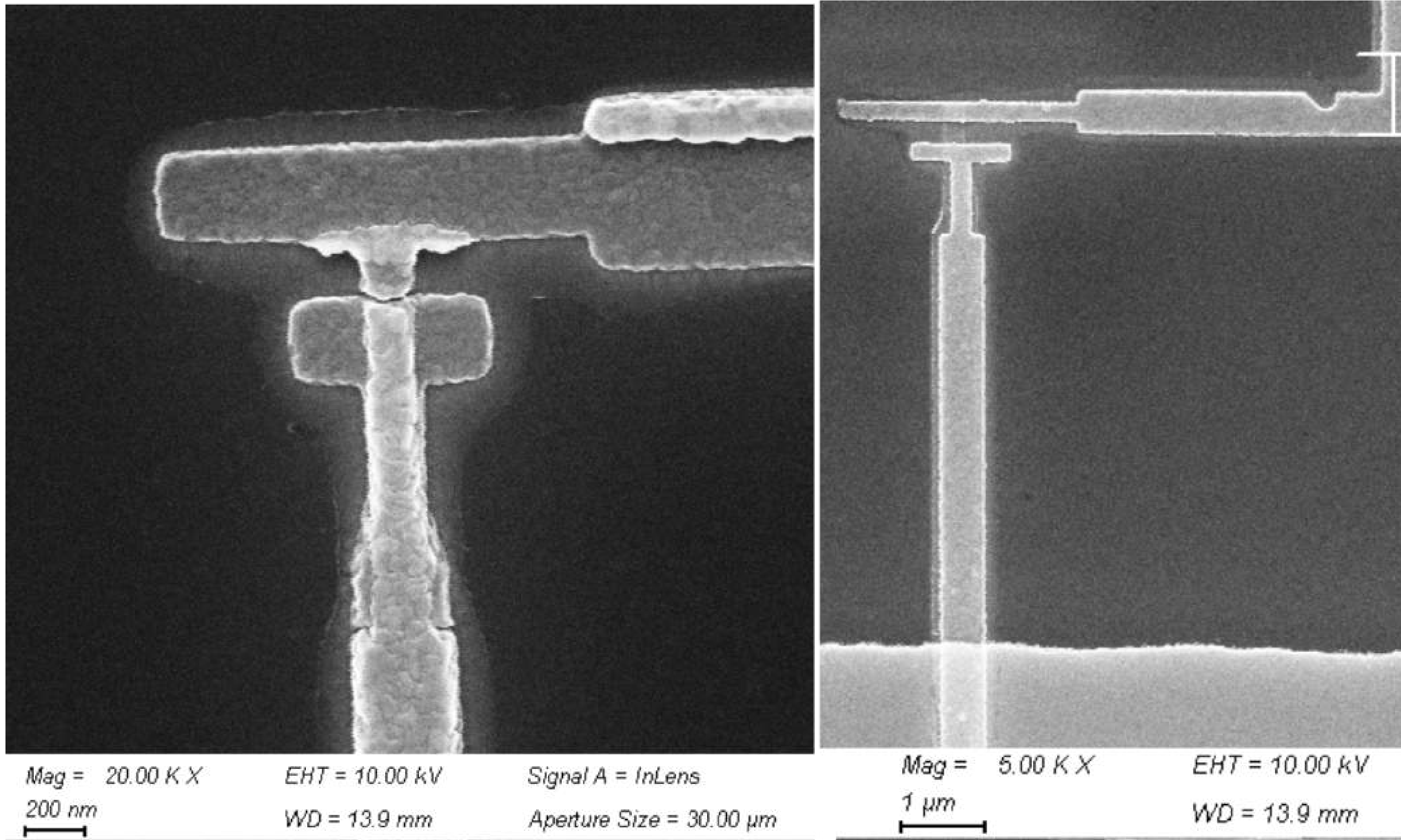

Figure 4.29: Angled deposition images. First image shows crack near junction area resulting from 90 degree deposition followed by 40 degree deposition. Angle measurement can be used to calculate resist height.In this case 30 degree angle first and 90 degree second deposition makes for easy resist height calculation.

For the calculation of the proper angle for deposition, it is necessary to know PMMA expected height, resist total height and width of bridge region. It is important to note that unless the recipe has been optimized such that bridge width comes out to intended size, the actual size must be measured using a SEM microscope. Then its just a matter of adjusting the angle of deposition to the desired junction area.

Some other considerations can be made regarding angle of deposition and their importance to the overall process. High angle depositions over pre-deposited material can cast shadows and cause cracks as seen on Figure 4.29 (left). This junction was fabricated using a right angle 90° deposition first and 40° angle after oxidation. Therefore for high angles must be used on first deposition only, when using Dolan method, this way a 90° deposition can be used secont to mend any contact issues on contact pads. The result of high angle first and normal deposition second is displayed on Figure 4.29 (right).

Furthermore angled deposition can serve as means to check resist stack height. It is important to monitor resist height, and this is a means of checking how resist height might have affected the outcome of a specific sample that is being viewed on the SEM microscope. Surely there are other means of checking resist height, through various instruments. However this allows for the calculation of resist that has been already removed. On Figure 4.29 (right) the deposition was 60 nm at a 60° angle followed by 100 nm at 90°, which it makes it easy to calculate resist stack height using basic right triangle properties. For this case resist height was calculated to be 550 nm since the shadow cast was 960 nm at a 60° angle to normal. It is optimal to choose small angles for deposition, this offers more control as the angle can be varied to change the area. When using high angles such as the deposition on (Fig. 4.29 (right)) and also for Manhattan[74] style junction, the area can not be changed and resistance needs to be optimized by area and oxidation time only.

4.4.4 Considerations on e-Beam Developers

In this section we will discuss developer options for the fabrication of Josephson Junctions. In literature we've found that development procedure is many times done with MIBK 1:1 IPA [43], however we opted for using commercially provided developers. We have experimented extensively with both developers supplied by All Resist, they both contain MIBK and IPA however in different proportions. Both 300-55 and 300-56 work for Josephson junctions, being the 300-55 the stronger acting developer among the two.

By using the weak developer we were able to work with a variant of the L junction, displayed on Figure 4.29. As seen in the image the contacting side has a T shaped structure, this structure provides enough dose near the junction region to make functional junctions with the weak 300-56 developer, example on Figure 4.35 b. However if the strong developer (300-55) is used on this structure, the issues are such as seen on Figure 4.29 (right). The gap becomes very large and the T structure starts to also deposit through the gap. If the T structure is removed the strong developer works fine (Fig. 4.35 c). Furthermore without the T, the pattern does not work well with the weak developer, as there is not enough backscattered electrons in the region. We opted for working with stronger developer and the simpler L geometry without the T, the criteria being that achieving a junction with the least amount of excess features is desirable.

4.4.5 Josephson Junction Lift-off Process

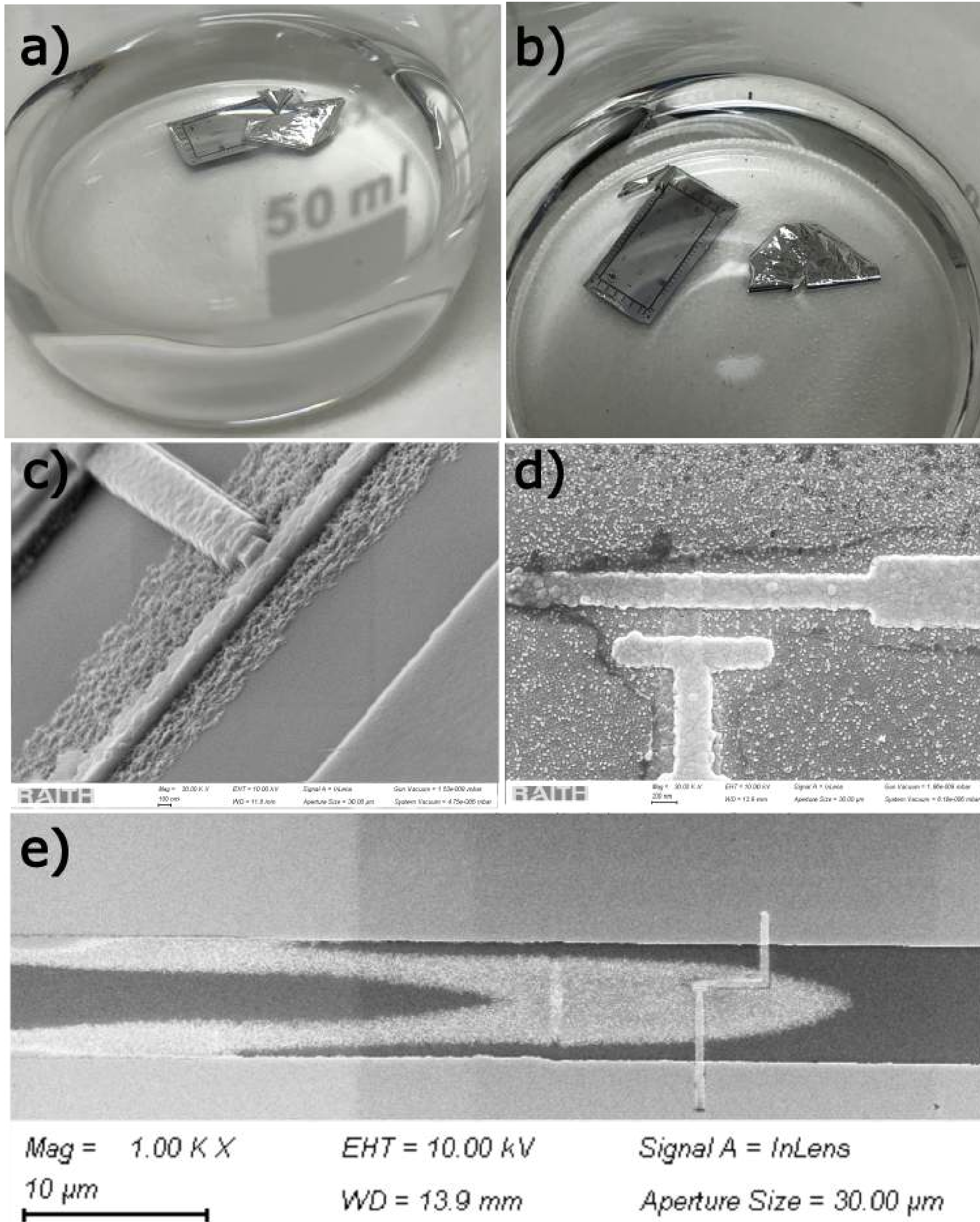

Figure 4.30: a) A becker with a chip inside undergoing lift off procedure in Acetone or DMF solvent. b) Aluminum layer is seen completely detached from sample. c-e) SEM images of defected circuits we believed to have been damaged during this process when ultrasound is applied to speed up the process.

The lift off procedure was optimized to remove the deposited layers associated with the Josephson junctions, this can be seen on Figure 4.30 a. Here we see the Al layers peeling off the sample, gently spraying with acetone will loosen it (Fig. 4.30 b). It can then be removed with tweezers. Some Al be stuck to corners, if so place very quickly in ultrasound (1s), transfer sample to clean acetone and continue process as listed on Table 4.4.5. Furthermore its important not to perform ultrasound cleaning with Dimethylformamide (DMF) as this will remove the junctions altogether. This recipe provides clean structures free from re-deposition. Re-deposition during the lift off of thin films and resist structures refers to the phenomenon where material that has been removed during the development process is redeposited onto the substrate or other surfaces (Fig. 4.30 c-e). The lift off process consists of using chemicals to dissolve the resist, removing it and allowing the excess aluminum to be removed.

We've noticed that by quickening the process using ultrasound to help remove the resist and aluminum causes detrimental effects to process quality. During ultrasound the excess aluminum film disintegrates into a fine powdery consistency that contaminates the solvent. It should be noted that the redeposition is believed to occur while the sample is being handled, while wet in acetone or DMF it will not stick. Although this is avoidable, we managed to optimize the development process parameters (such as time, temperature, and agitation), to make sure the aluminum layer is removed whole. This enables the sample to be handled in a clean solution, raising chances of success. Furthermore it should be noted that using the e-beam resist cold ($\approx 17\ C^{\circ}$) makes it harder to be removed during lift off and this should not be used as way to make resist thicker.

Step	**Description**
DMF	10 min 70°C or until Al begins to peal off (Optional).
Acetone	10 min 70°C or until Al begins to peal off, squirting the sample with some clean acetone may help.
Transfer	Transfer sample to clean becker free from aluminum.
Ultrasound	180s ultrasound cleaning.
IPA	180s ultrasound cleaning.
Dry	Rinse with IPA, dry with N_2.

4.4.6 Defining Recipe Stability Metric from Room Temperature Measurements

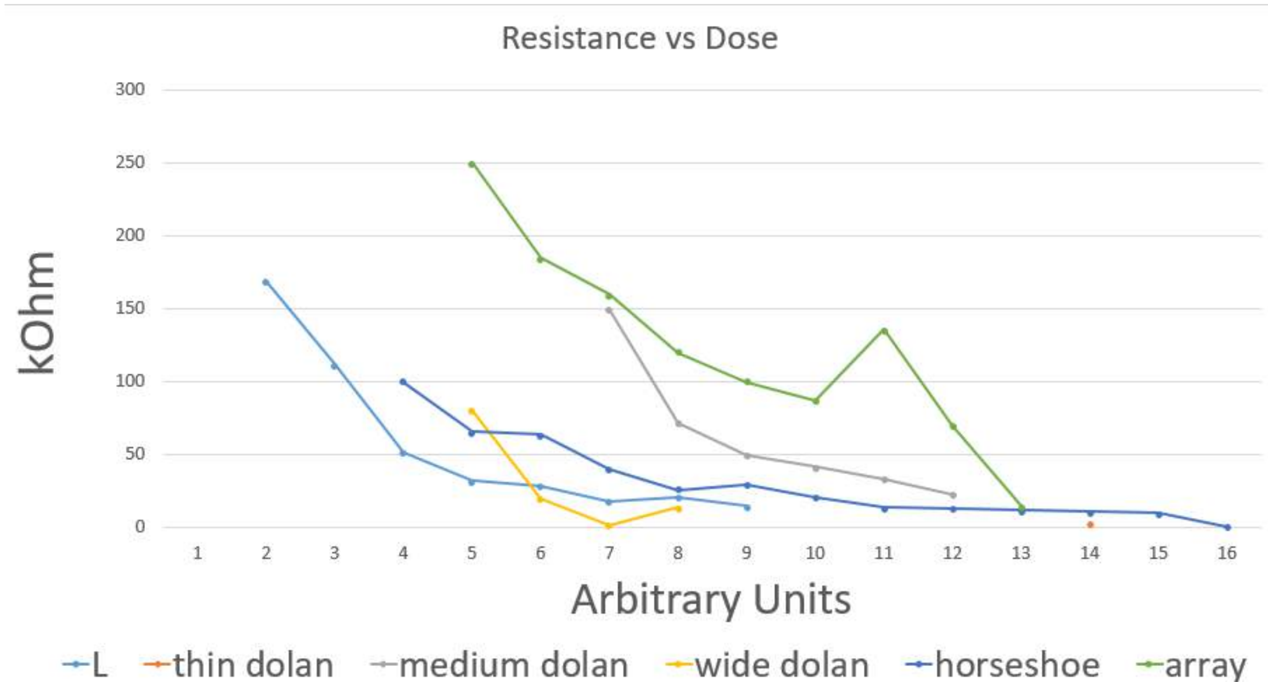

Figure 4.31: Chart displaying resistance of Josephson junction devices based on the dose applied during patterning. This chart results from a dose test deposition and the measurements of junction resistance as a function of e-beam dose. A higher dose window resulting in a functional device indicates a recipes robust to process variation.

Generally the best dose is decided based on SEM analysis of bridge structure, we thought it would be important to try and define a dose based on a dose dependent deposition. Therefore we analyzed 5 different geometries and an array of 10 Josephson Junctions. Some geometries have already been shown and others will be shown on Section 4.4.8. We then plotted the resistance of each geometry for a certain dose displayed on the Figure 4.31. From this analysis we conceptualized the fact that some geometries are more robust to process variations than others, resulting in recipes which yield less variations. This motivated the major contribution from this thesis, which was to analyze the reason for some lithography patterns to perform better than others. We measured resistance of several geometries from high dose to low dose. At low enough dose the pattern doesn't form a bridge and resistance measures is of the substrate. At the other extreme the structures is warped and destroyed resulting in a short reading. Essentially a larger dose window translates to a higher success rate. This graph shows how big is the window, for process success. Furthermore it also shows that different geometries start to form the bridge at lower doses, which implies less deterioration suffered by the top resist layer.

4.4.7 SEM Junction Area Analysis

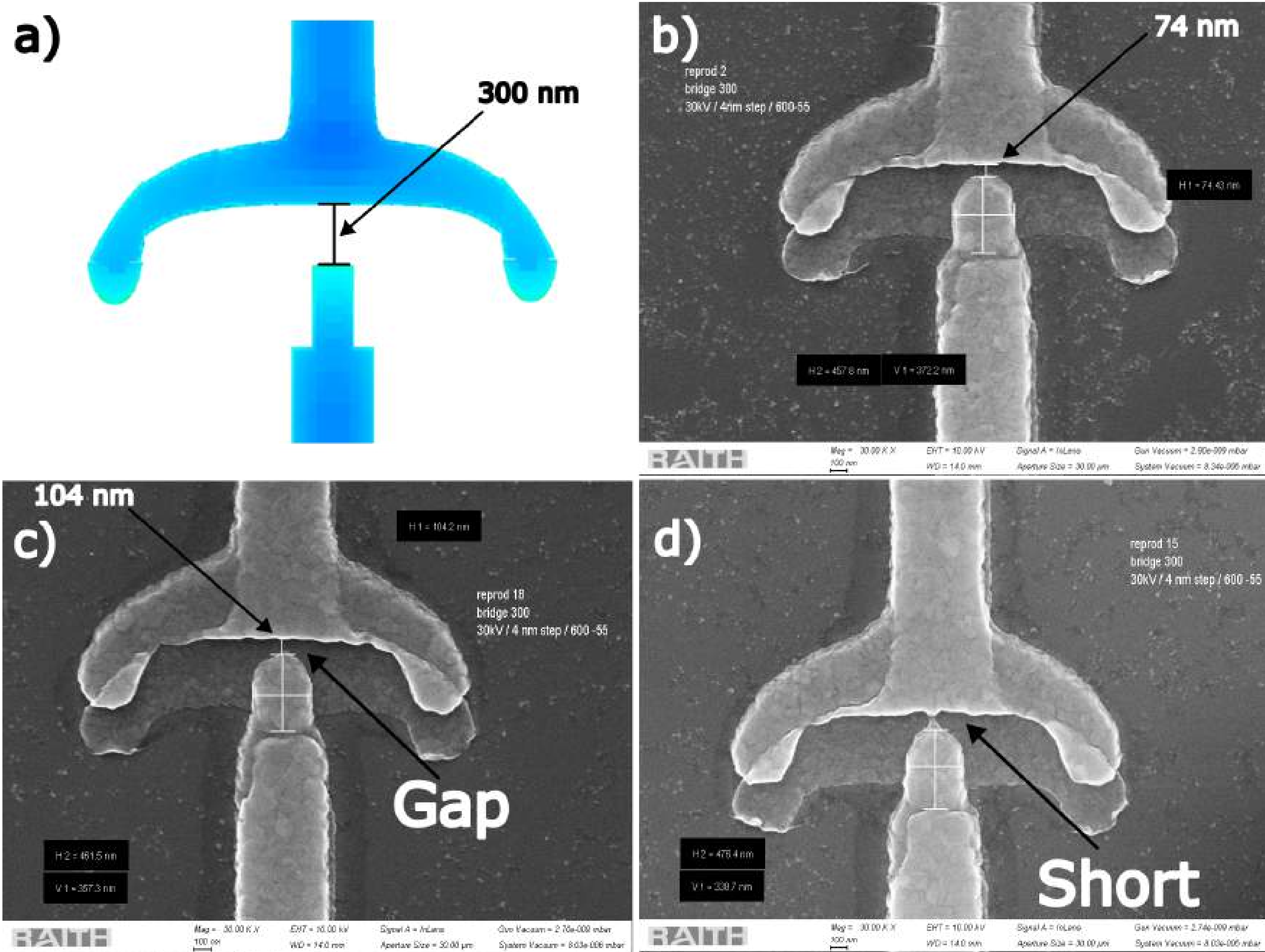

Figure 4.32: a) Horseshoe e-beam pattern with applied PEC. Three out of 27 SEM images of horseshoe junction fabricated with the same dose on the same sample within the same exposure. b) Image of horseshoe junction with measured gap of 74 nm and area of 0.161 μm^2 . c) Image of horseshoe junction with measured gap of 74 nm and area of 0.170 μm^2. d) Shorted horseshoes junction with area of 0.161 μm^2.

The same junction was exposed 27 times and the area carefully measured through SEM imaging resulting in a area variation analysis. In this section we display results of two tests each with 27 junctions, one for L and another for horseshoe junction.

For this specific sample we had 17/27 good horseshoe junctions. from the SEM images, we can say that this is an overdosed recipe. We calculated the area using the SEM images and also measured the gap which turned out to small with an average of 96 nm. The variations from each exposure is enough to cause 37% of junctions to short out. In the four images displayed here (all images available in supplementary material) Figure 4.32, we can see gap variation and a shorted junction in the last image.

This result highlights how high the range of variation associated to this process. Hence the need for recipes which accommodate these variations by having highest possible selectivity and proper backscattered electron engineering.

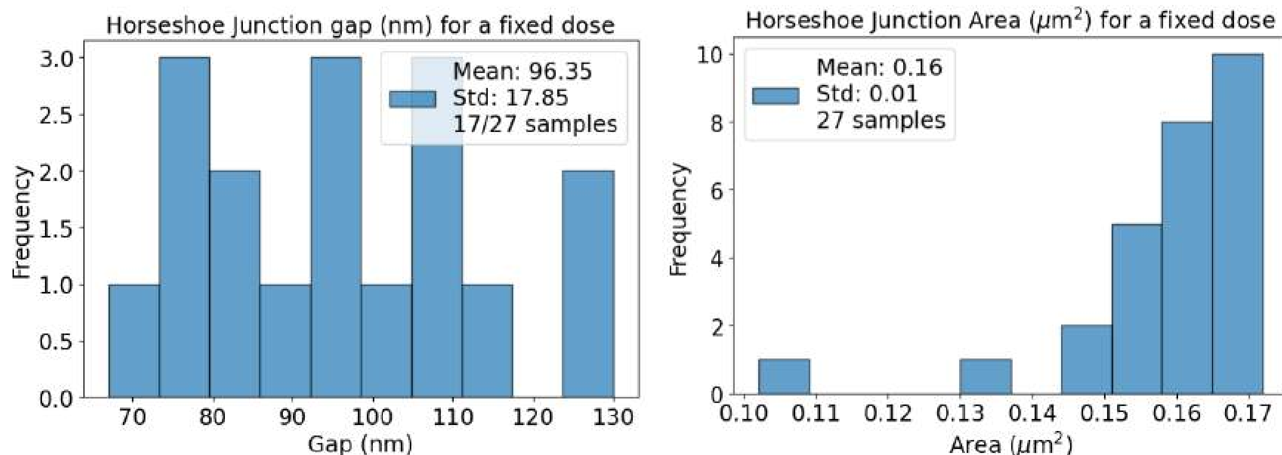

Figure 4.33: Left: histogram of gap values for 17 out of the 27 junctions which were not shorted. Right: histogram of measured area through SEM imaging of the 27 samples.

4.4.8 General Josephson Junction Fabrication Results

The junctions inspected on Figure 4.34 are from the dose test which created the graph 4.31. The three geometries are shown here before the bridge region is formed, the middle picture shows the best junction and subsequently the first bridge collapse. The thin Dolan did not form a good junction during this particular dose test, showing that 30 kV process needs to be adapted to make such small junctions. The regular thin Dolan junction shown on Figure 4.25a. The deposition occurs by projecting forward the wide side first and on the second deposition the thin side is now projected forward creating a contact over the first wide deposition. This can be seen in the Figure 4.34. Here we display tree different sizes for the wide part 400 nm, 1 μm and 4 μm. The respective resistance measurements of these dose tests are displayed on Figure 4.31. On the chart it is clear to see that more exposed area near the junctions allows for the bridge structure to form at a lower dose, avoiding the overexposing of the top resist layer.

We demonstrate a crucial balance between excessive and insufficient backscattered dose in our study. The large 4 μm exposed pad of the wide Dolan junction significantly contributes to the unexposed region. This means that even a small variation in the exposed dose can lead to a substantial variation in the dose received by the unexposed region. Our findings indicate a narrow window for successful outcomes, as illustrated in the chart.

Interestingly, the window for success shows a significant increase from the thin Dolan to the medium Dolan junctions, but decreases from the medium to the wide Dolan junctions. While the medium Dolan junction with over 1 μm does offer a window large enough for reproducibility, it still performs less effectively than the horseshoe and L junctions.

SEM imaging is an vital part of process optimization, here we show samples Josephson junctions devices,

fabricated from different geometries and seen from different angles. We managed to successfully fabricate a wide range of Josephson junction devices, including small SQUID devices enclosing 100 μm^2 area and Josephson junction arrays.

The horseshoe junction will sometimes form two side junctions as can be seen on Figure 4.37 a and b. However we suspect this should not be a problem since the tunneling across the junction is depends on the phase across them, and since both sides of junctions are connected, we suspect the phase difference should be zero. Nevertheless sometimes the side parts dont leave the gap clearly seen on Figure 4.37 b and as seen on Figure 4.37 c.

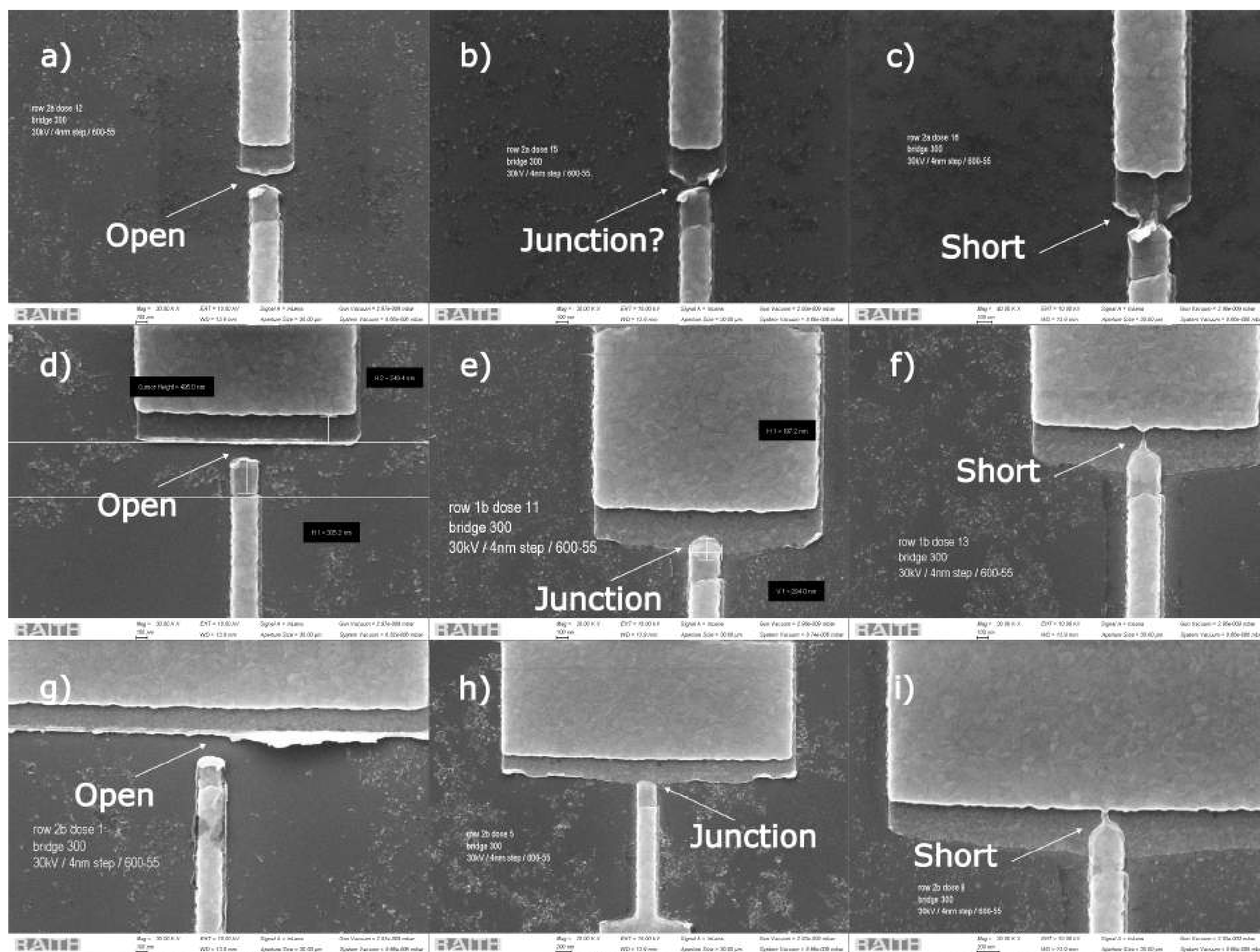

Figure 4.34: Dose test deposition of Dolan Junctions, the tree geometries are thin medium and wide Dolan. On the first column we have underdosed junctions, on the middle column the best junctions and on the right a short circuit. a-c) Thin Dolan junctions, not one properly formed junction was registered in this dose test. d-f) Midium Dolan was the best performer and the best dose yielded a satisfactory junction (e). g-i) Wide Dolan dose test showing a well formed junction (h).

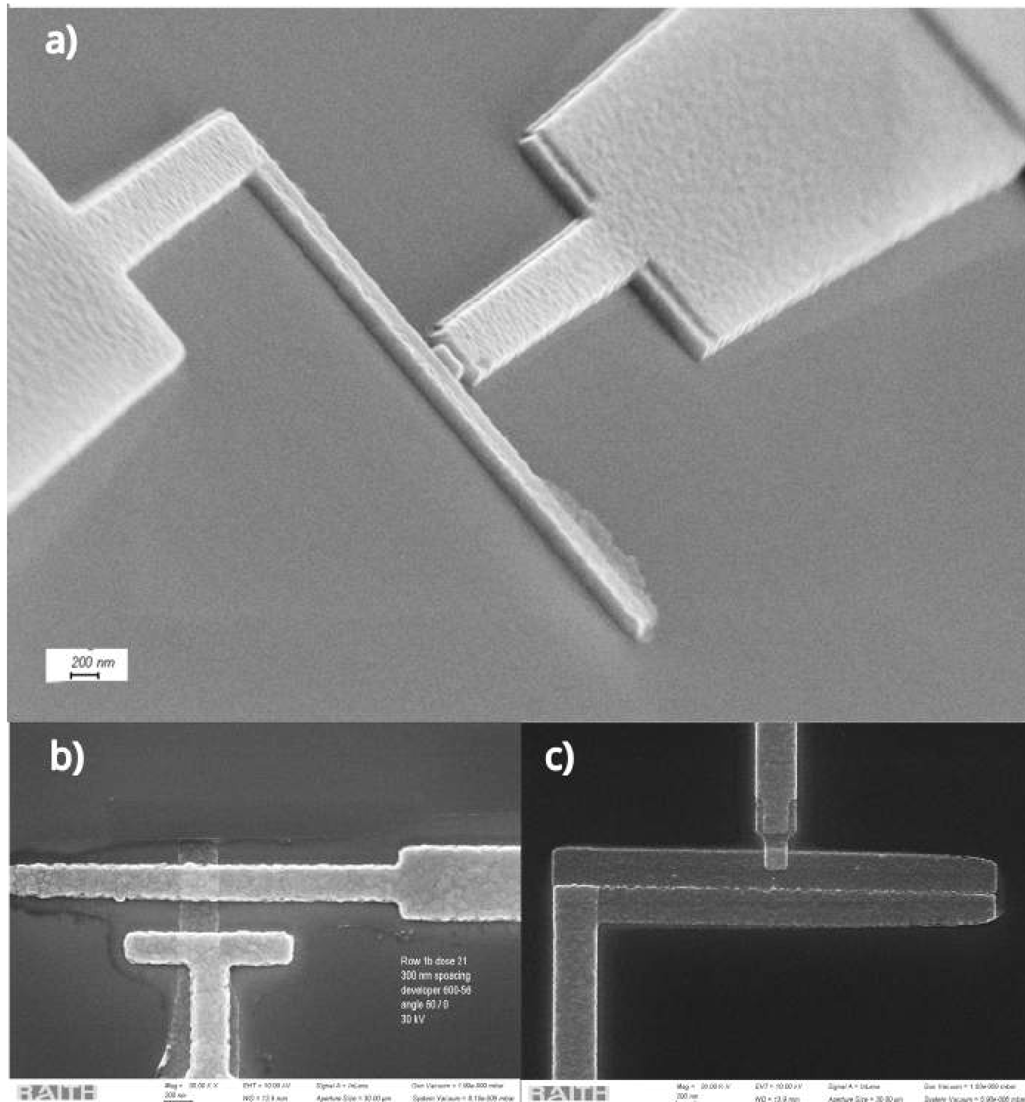

Figure 4.35: Examples of L junctions. a) L junction birds eye view. b) L junction with T shaped finger shown from above, developed with weak developer 300-56, top view. c) Regular L junction developed with strong 300-55 developer top view.

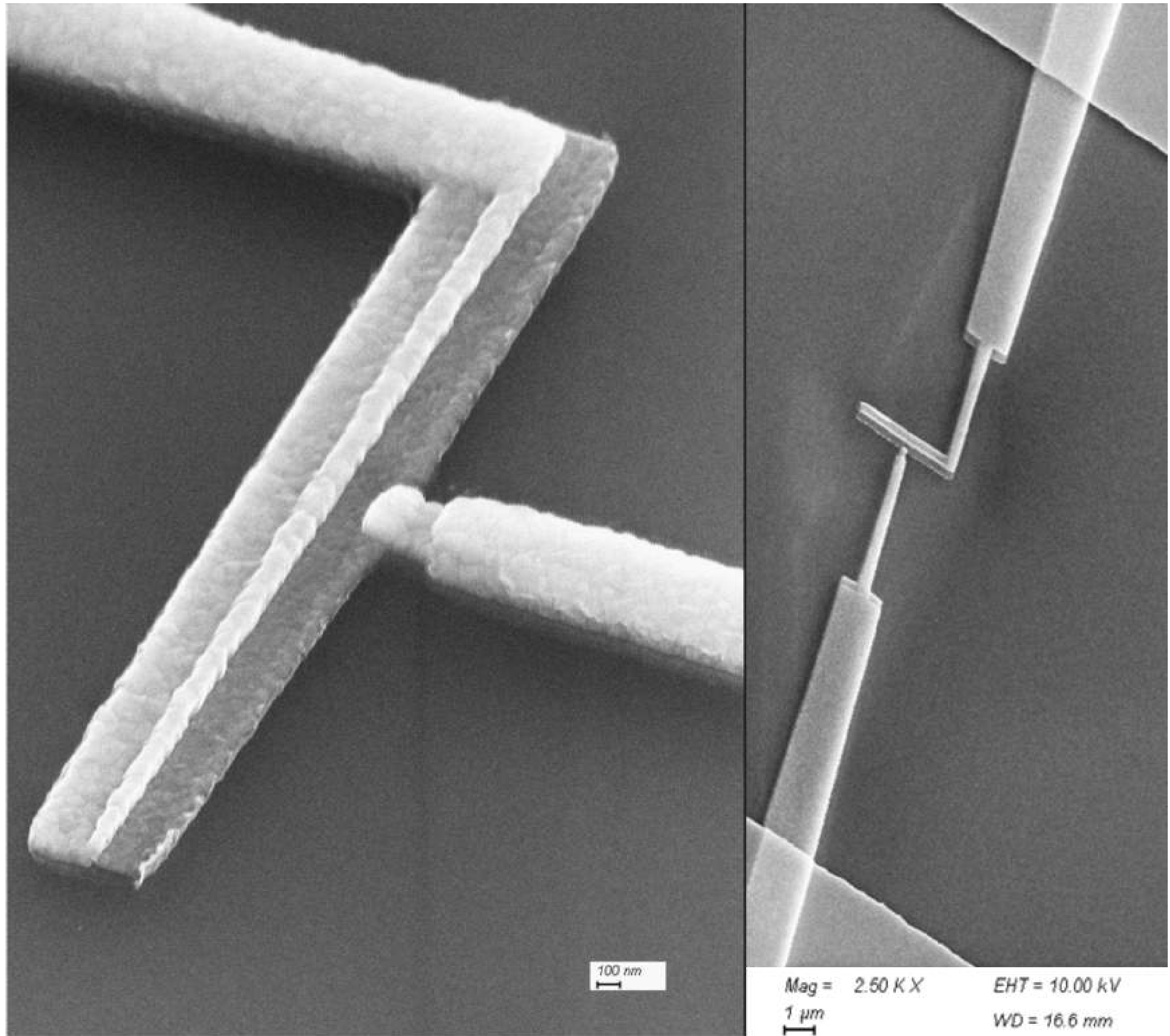

Figure 4.36: SEM image of pristine L junction deposited at 30 / -30 degrees. On the left a close up view of oxidized Al from the first deposition is contacted by non oxidized Al of the second layer. On the right the junction is seen in a zoom out view, showing its anchoring to a previously fabricated contact pad.

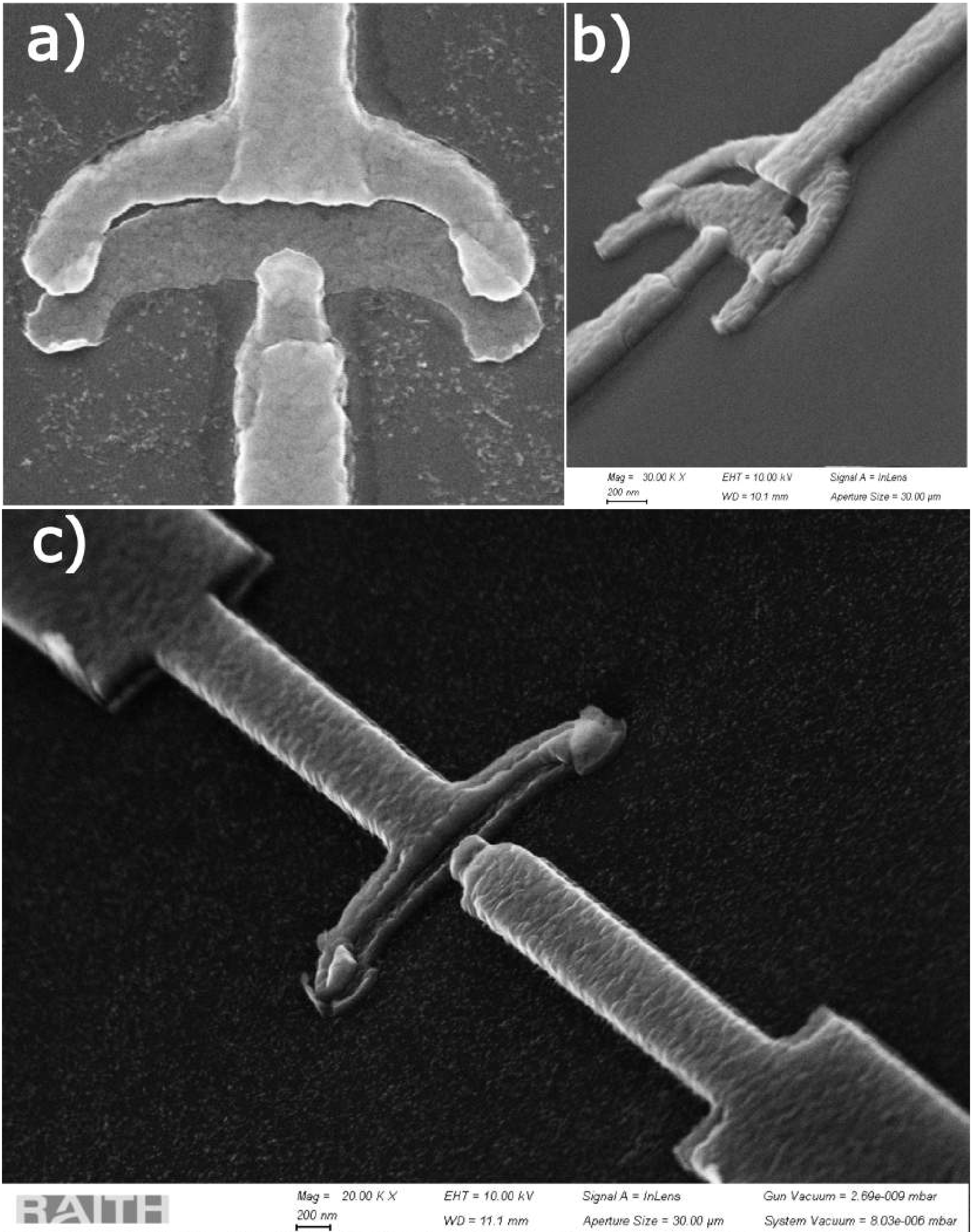

Figure 4.37: SEM images of the horseshoe junction, a) Top view of Junction, b) Angled view from the side of the junction, c) Angled view from the contact point.

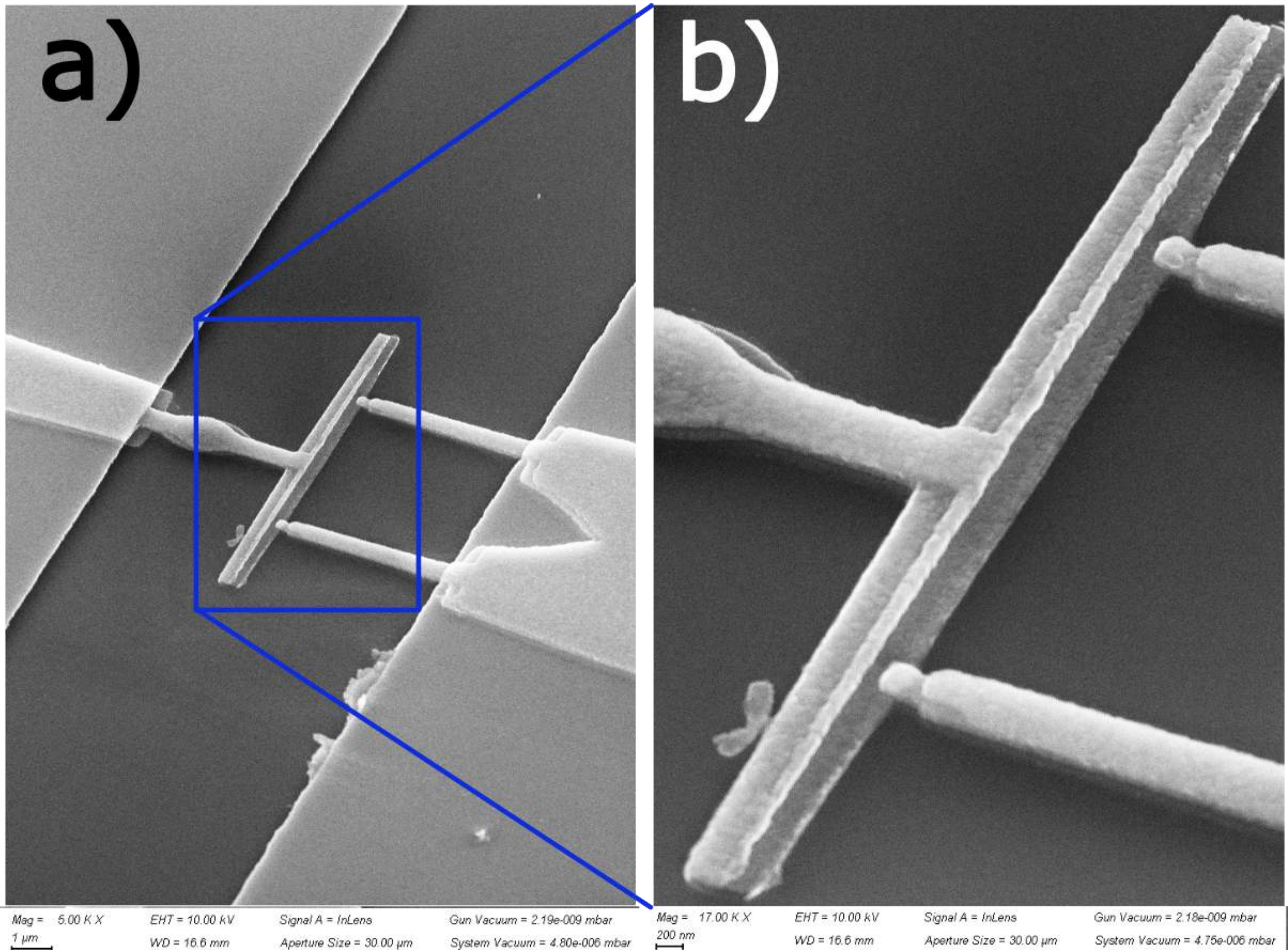

Figure 4.38: SEM image of L type squid junction, and squid. This Squid encloses a area of 100 μm^2. a) Image of squid device, b) zoom into junction contact points.

The L geometry was the first to start bringing consistent results, there were two versions of it. One with T bar which we have found records in the literature claiming it relieves stress in PMMA bridge [39, 40]. However we have found that the T structure results in the creation of more backscattered electrons in the region. Relieving excess dose from PMMA making it more durable as discussed on section 4.4.4. In the images we see perfect L junctions with precise contact points.

We suspect that the engineering of these devices has just begun, and as with any other electrical device, size matters. One of the challenges we set forth was to make the smallest squid possible. On Figure 4.38, we show a small squid (10 μm x 10 μm), it is the smallest we were able to make so far.

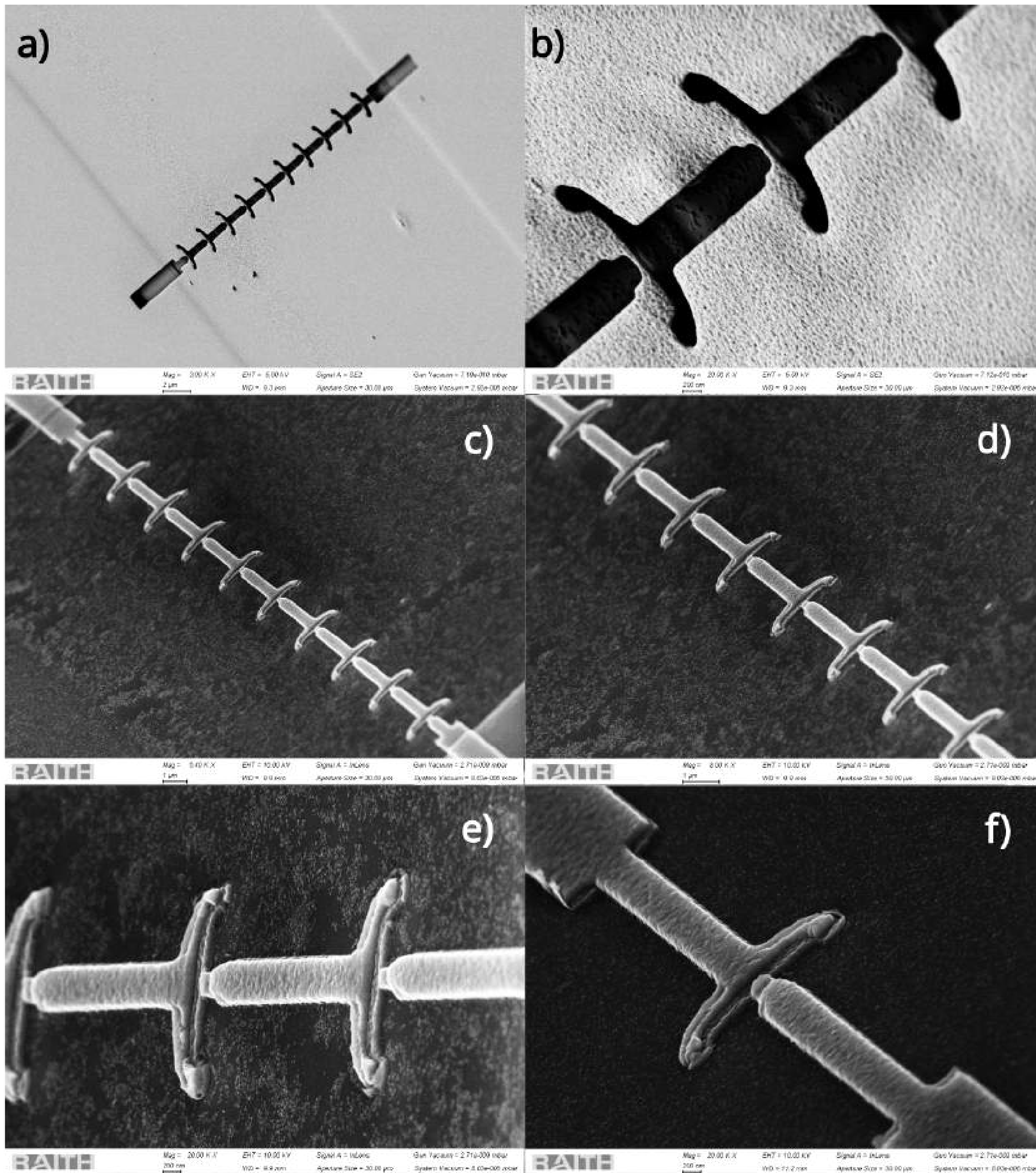

Figure 4.39: Images displaying Josephson junction arrays patterned on resist and resulting deposited devices. a) Full patterned resist structure, b)zoomed view. c-f) deposited Josephson Junction array at progressively higher magnification. SEM image

Another important result is that the horseshoe pattern enabled us to conceive devices which use Josephson junctions in numbers. This can be difficult with to achieve depending on the used geometry, it must be

periodic in a way which respects the inherent properties of the e-beam fabrication process. The horseshoe junction can be joined together in a lego like fashion, on Figure 4.39 we show an array of 10 junctions created in a row, innovative method to create multiple junctions using the horseshoe junction. This pattern works due to the unique distribution of backscattered electrons created at each bridge region. And the careful choosing of separation distance allows minimal distortions from one junction to its neighbor.

4.4.9 Sample Mounting

Lastly we must prepare the sample to be measured. In our case we used a diamond cutter, successfully cutting wafers in artisan manner takes some practice. Wafers should always be covered with resist when cutting to protect the samples. In order to maximize sample production we often apply e-beam resist to the whole wafer once circuits are ready. This ensures all samples will be subject to the same conditions, same resist height and time of deposition. However the actual time of exposure will vary from sample to sample. After exposure samples are cut into individual dies before development and further processing. Cutting after development risks contamination of the exposed structures.

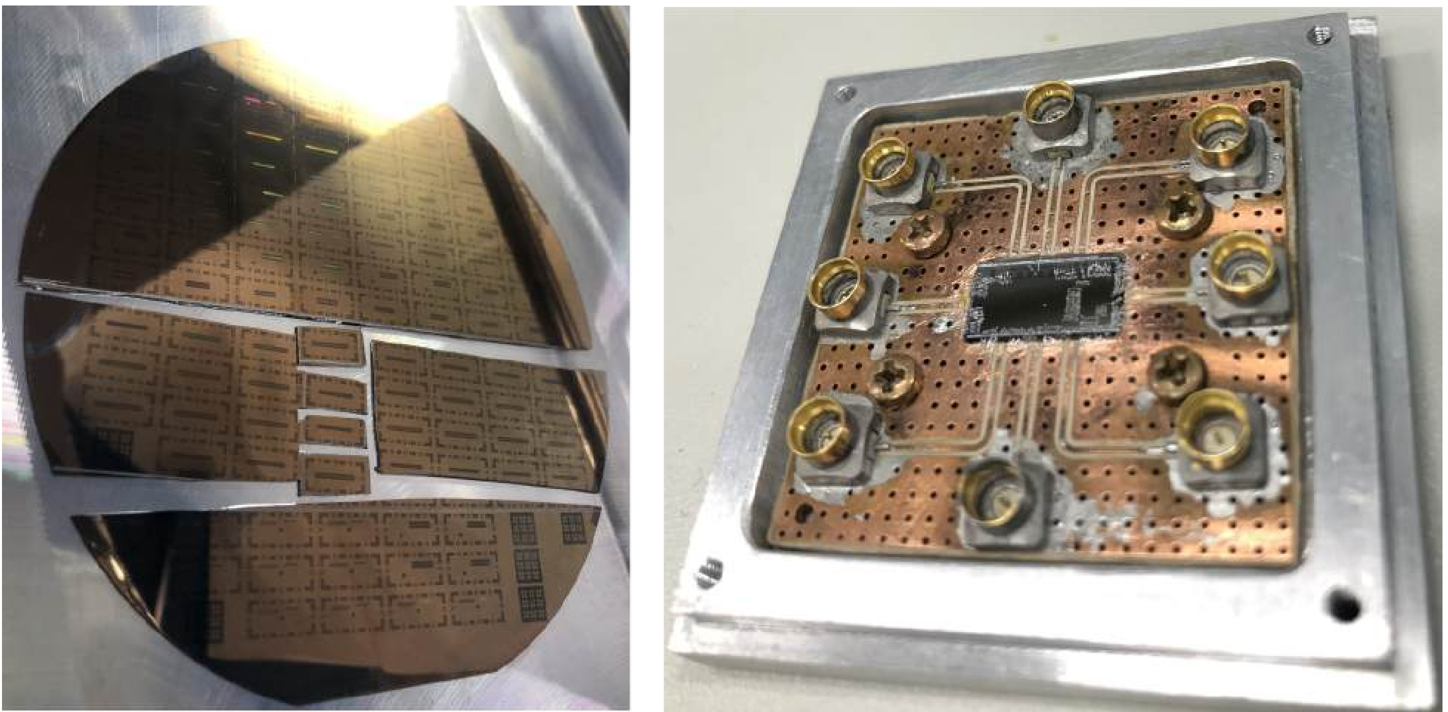

Figure 4.40: Right: Partially cut wafer with tens of samples. Left: Sample mounted and wirebonded to sample holder with 8 ports (LFDQ).

It is important to understand the details of all steps of the process in order to set up a high yielding procedure. For instance the wafer crystal orientation must be carefully aligned during photoligraphy, this will ensure dies follow the same orientation. Additionally two buffer zones must be accounted for. One for cutting between dies and another for the wirebonding pads. Enough space between dies for cutting

typically a few millimeters is plenty. As seen on Figure 4.40 right, leaving enough space ensure samples will not be lost. Furthermore sample holders usually have strict die size, therefore placing pads close to the edges will most likely result in loosing samples. Therefore the wirebonding pads are usually placed as far in as possible. This doesn't count in favor of impedance matching, in theory it is for the wirebonding wire length to be as short as possible.

Before wirebonding the sample is smeared with a very small amount of cryo-varnish for thermal anchoring to the sample holder. For application a clean toothpick can be used to pick up trace amounts, using too much varnish will cause excess to be pushed out possibly contaminating the sample. On Figure 4.40 left we can see a sample that has been properly mounted and wirebonded, most of the connections are grounds. At least two connections per pad should be made and ground planes which are separated by active circuit elements should be connected with wirebonds to avoid the creation of stray currents.

4.5 Simulation Results and Low Temperature Measurements

In this section we will discuss the results of the applied fabrication techniques which were discussed in the previous chapter. Starting with a brief description of experimental setup. We demonstrate simulation results using Qiskit Metal and ANSYS simulation software. We then present pictures of the sample and measurements of the one qubit chip.

4.5.1 Measurement Setup

Dilution refrigerators are crucial components in many quantum computing experiments and applications, particularly those involving superconducting qubits and other quantum devices. These refrigerators are capable of achieving extremely low temperatures, typically in the millikelvin range, which is necessary for maintaining the quantum coherence and control of qubits.

The dilution refrigerator used in this study is a part of the LFDQ laboratory, located in the Glebb Wataghin Physics Institute. The measurement apparatus was assembled by Prof. Dr. Francisco Paulo Marques Rouxinol and Dr. Lucas Medeiros Ruela, who also contributed with the code used to measure the circuits at low temperatures.

The dilution refrigerator (Fig. 4.41) uses a mixture of helium-3 (^{3}He) and helium-4 (^{4}He) isotopes. The operation of such refrigerators relies on the principle of dilution cooling, where the mixture of helium isotopes undergoes a series of cooling stages.

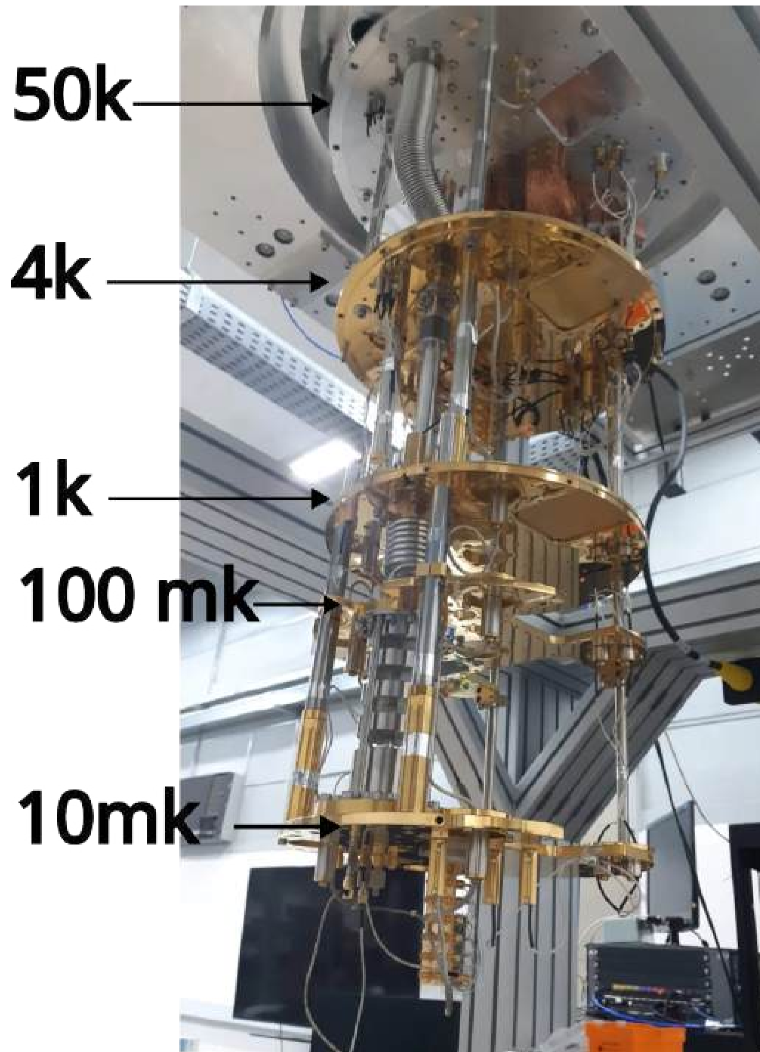

Figure 4.41: LFDQ Dillution Refrigerator, in the image 4 stages can be seen. From top to bottom we have 4k, 900mk still, 100 mK cold plate and the mixing chamber flange at 10 mK. The bottom stage is able to keep 10 mK continuously using a mixture of ^{3}He and ^{4}He isotopes.

To operate the dilution refrigerator, a vacuum is created within the chamber. Once the system has reached 10^{-5} Torr pressure, it is ready to begin cooling. First ^{4}He is pumped to make the system temperature drop to 4K. Once this temperature is reached the mixture of ^{3}He, ^{4}He isotopes will begin to be pumped into the dilution system. When the mixture is subject to a pressure drop, it undergoes a phase separation [3, 75, 76], with the helium-3 becoming enriched in the liquid phase. This phase separation process absorbs heat, causing the remaining mixture to cool down. The heat is then removed by the vapor phase, which is vented back to be recycled. By repeating this process within the still, progressively lower temperatures are achieved. A heater is placed within the still to keep it at 900 mK. This is necessary to keep the effect continuously dissipating heat.

The Dilution refrigerator can achieve temperatures as low as a 10 mK. These ultra low temperatures are essential for preserving the delicate quantum states of qubits and minimizing thermal noise, thereby enabling long coherence times and high-fidelity quantum operations. The precise mixing ratio of helium-3 and helium-4 isotopes is crucial for optimizing the performance of dilution refrigerators. Different mixing ratios can affect the cooling power, efficiency, and temperature stability of the refrigerator. Here we use a high concentration of helium-3 is used for achieving lower temperatures.

Furthermore the dilution refrigerator has 5 stages of thermal anchoring as shown in Figure 4.41 to provide stable and low-noise thermal environments for housing qubit devices. These stages help to minimize thermal fluctuations and maintain the quantum coherence of qubits. Furthermore they provide a reference temperature for the cryogenic attenuators used, to gradually decrease the number of photons transmitted. Essentially, conducting this process at cooler temperatures reduces the added noise. However, this reduction in noise comes at the cost of generating heat, which must be effectively dissipated, thus requiring a trade-off [77].

Experimental Setup

Cryogenic circuits have many components which perform varied purposes along the lines. Starting with the most broad application equipment the Vector Network Analyser (VNA), is a system composed of many individual subsystems. This is very useful for quick and reliable probing, however being a composite system means there are hard limits to its applications. The measurements are continuous, to make measurement in the time domain a complex measurement system to apply pulsed time application. To get around these limitation powerful system The circuits start at equipment which create the signals which will interact with our samples.

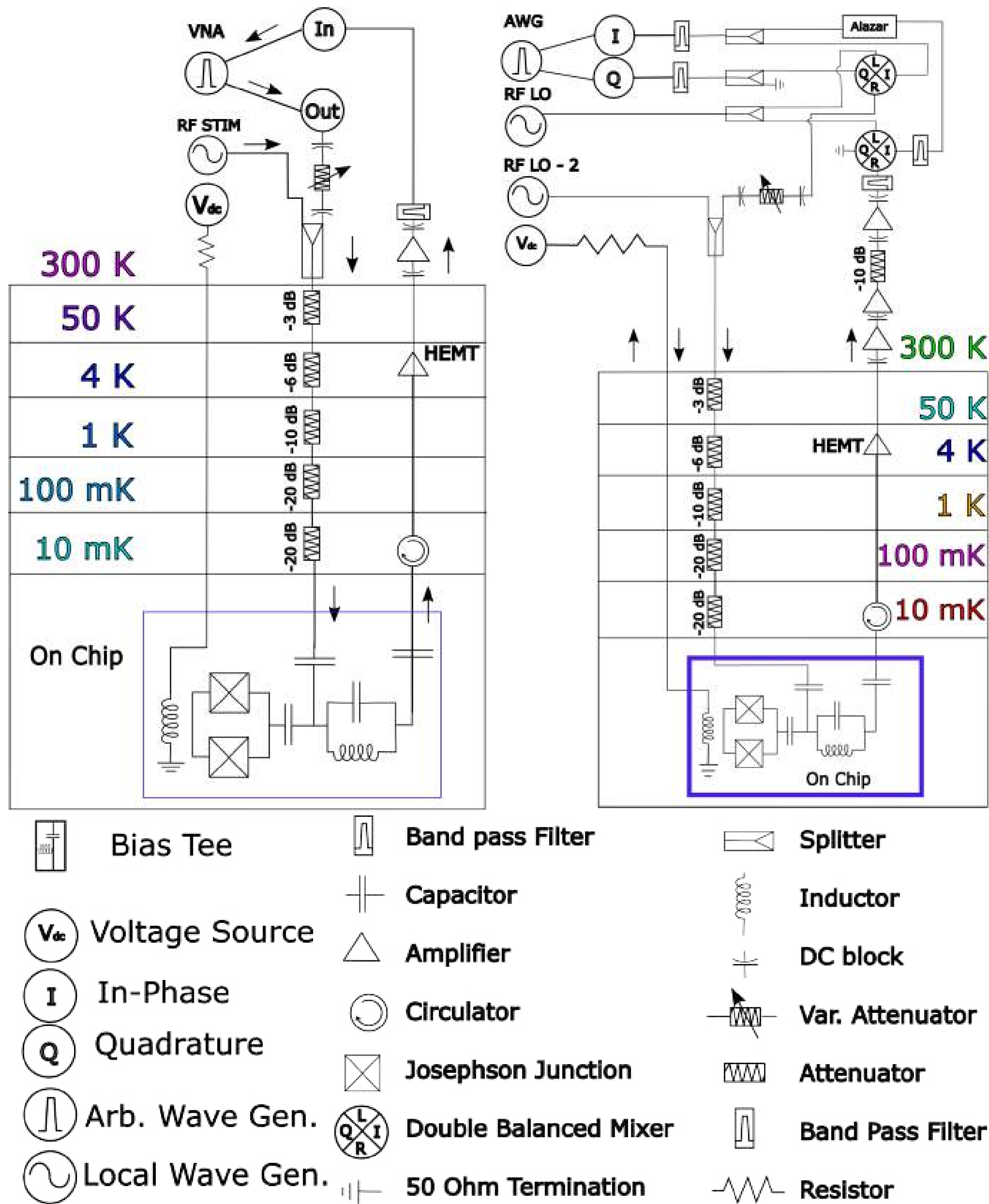

Figure 4.42: On the left we have VNA Experimental setup for measuring one microwave cavity. Signal is sent out from the VNA, passing through a digital variable attenuator, signal is them combined with RF STIM. A series of cryogenic attenuators, further attenuate the signals before reaching the cavity. The signal exits the cavity passing through a circulator and then a series of amplifiers before being captures once again by the VNA. Vdc is a voltage source used to apply magnetic flux to the qubit. On the right two tone qubit control and measurement experimental setup diagram.

The VNA is powerful tool for quickly setting up experiments and verifying system properties. Since it

has built in signal stimulation and acquisition, experimental set up is quick enabling fast trouble shooting before setting up experiments in the time domain. The VNA used in this study was Keysight ENA E5063A which has a range from 100 KHz to 18 GHz. The full diagram is shown on Figure 4.42.

The two tone experimental set-up was composed of several equipment. Starting off with Stanford Research System SIM 900 mainframe which housed 3 components a SIM 940 rubidium oscillator 10 MHz Clock, a SIM 928 Isolated Voltage Source and SIM 970 $5\frac{1}{2}$-digit voltmeter. The voltmeter and voltage source were used to apply magnetic flux to the qubit. The rubidium clock set the pace for all instruments used.

From here we used a Stanford Research Systems DG645 delay generator and two Keysight E8663D PSG Analog Signal Generators, 100kHz-9.0GHz to excite the qubit and measure the cavity. The signals were collected and processed using an Alazar high speed acquisition board. How ever in order for the signal to be processed it needed to be created at low frequency, up converted and after interacting with the sample, down converted once more to be measured. The reference signal used was 70 MHz, it was generated using a Keysight M8195A Arbitrary Wave Generator (AWG). The full setup is shown on Figure 4.42 left.

4.5.2 One Qubit Chip Design and Simulation

Here we discuss the desired characteristics we want to project into the Quantum Processing Units. These include types of qubits, types of cavity and coupling.

When defining a qubit design, all the measurement apparatus and qubit properties must be taken into account. Therefore the measurement apparatus will be ready to perform the desired measurements. With this in mind we designed two cavities one at 5 and the other at 6 GHz. We wanted to design a transmon therefore E_C and E_J were made to have $E_C/E_J = 50$. This would lead us to create a device with low charging noise and high coherence times. With this in mind we defined the characteristics of 7 GHz for the qubit.

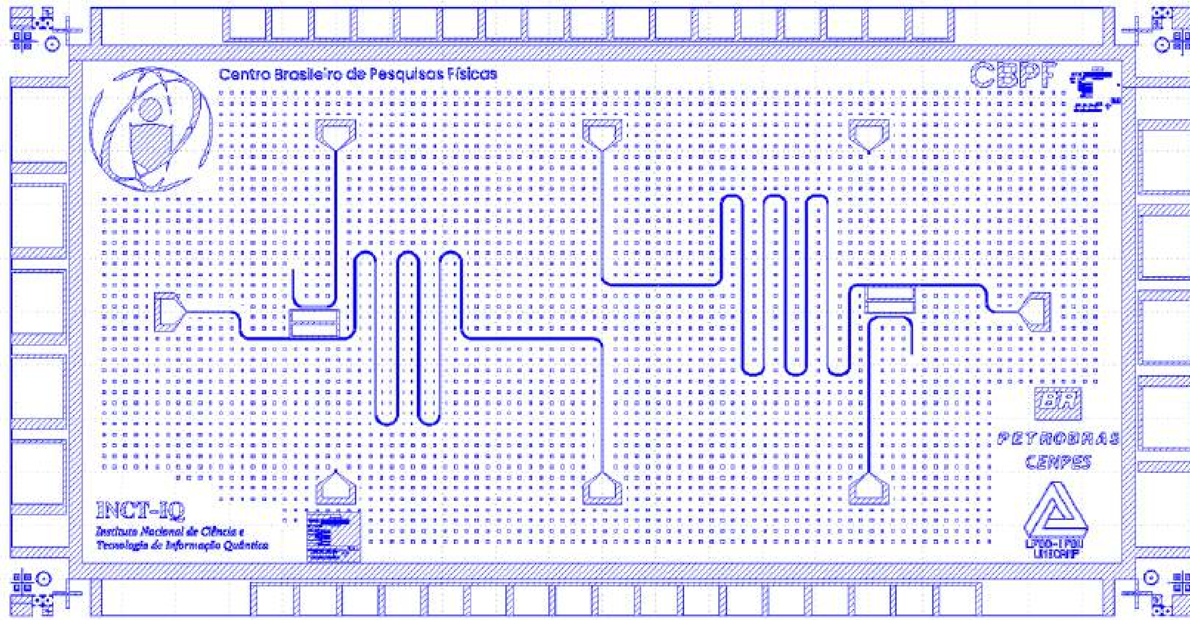

Figure 4.43: Chip containing two distinct cavity qubit systems, each cavity has a distinct frequency, one projected for 5 GHz and the other 6 GHz. Qubits were projected to have the same properties, including caivty coupling of 80 MHz.

Simulation

Using the detailed electromagnetic simulations performed with ANSYS, the results provide valuable insights into the high-frequency behavior of capacitors and resonant structures. These simulations accurately capture the complex interplay of electromagnetic fields, material properties, and geometric factors, allowing for the precise calculation of capacitance values and resonance frequencies. By visualizing field distributions and analyzing key parameters, such as impedance characteristics and energy storage capabilities, these simulations offer a comprehensive understanding of the performance of these components in high-frequency applications. The ability to optimize designs based on these simulation results enhances the efficiency and effectiveness of developing high-performance capacitors and resonant structures for various technological applications. We start by simulation the LOM model to define qubit coupling and properties.

Lumped Oscillator Mode Simulation

The Lumped Oscillator Mode (LOM) is initiated by passing in the components to be included in the simulation. For qubit and cavity, it is necessary to have qubit pads, ground plane and the cavity which it will be coupled to. It is not necessary to have the whole cavity, only the parts within the vicinity of the transmon. The capacitance matrix is obtained, usually assuming a frequency of 5GHz stimulation. By analyzing Table 4.5.2, the coupling strength between active surfaces can be evaluated.

All values in fF	ground main plane	pad bot Q1	pad top Q1	readout connector pad Q1
ground main plane	190	37	44	53
pad bot Q1	37	88	33	14
pad top Q1	44	33	84	3
readout connector pad Q1	53	15	3	72

Next these values are then processed by Qiskit Metal using Lumped Oscillator Model [63] analysis on the capacitance matrix. Which simply calculates Cq the sum of the capacitances which are applied on the Josephson junction. It also uses the capacitance between the pad and readout to calculate the coupling strength g, next it fits solutions to the Hamiltonian, yielding the following results for the transmon and its coupling properties:

Transmon Properties	**Value**
ω_q (GHz)	6.15
E_C/h (MHz)	323
E_J/h (GHz)	16.22
α (MHz)	-370
Dispersion (KHz)	2.6
Lq (nH)	10
Cq (fF)	60
$T1$ (μs)	31

Coupling Properties	**Value**
$tCqbus1$ (fF)	5
$gbus$/h (MHz)	70
χ_{bus1} (MHz)	10
$1/T1_{bus1}$ (KHz)	5.2
$T1_{bus1}$ (μs)	31

The advantage of this process, compared to doing it by hand, is the speed and accuracy at which circuits can be designed and processed. The simulated Transmon properties are as follows: the qubit frequency, ω_q, is 6.15 GHz; the anharmonicity, α, is -370 MHz; and the qubit coherence time, T_1, is 31 μs. With a cavity frequency of 5.4 GHz and a coupling strength, g_{bus1}, of 70 MHz, the dispersive shift, χ_{bus1}, is -10 MHz. These parameters provide the system with reasonable working conditions.

Other properties are also considered, such as the charging energy E_C, which is 323 MHz, and the qubit charge dispersion, which is 2.6 kHz. Furthermore, the qubit capacitance, C_q, is 60 fF. At this point, it is worth noting that $E_C/E_J = 50.2$, aligning with the desired transmon values.

It should be noted that the Josephson frequency, given by E_J/h, is 19.22 GHz, which results from selecting a qubit inductance, L_q, of 10 nH. This value is chosen based on expected values and does not arise from geometric features. Instead, it is directly related to barrier properties, such as the width and area of the oxide layer during Josephson Junction fabrication. The oxidation dictates the potential of the tunneling barrier, restricting the flow of supercurrent, which gives rise to the inductance. The relationship between the Josephson inductance and the room temperature resistance, through the Josephson critical current I_C, is described by the Ambegaokar-Baratoff relation [78]. Using this value and simulated circuit properties, the predicted qubit frequency is 6.2 GHz, calculated using the equation for transmon energy, which can be approximated as $hf_{01} = \sqrt{8E_JE_C} - E_C$.

The coupling properties to the bus are as follows: the coupling capacitance, t_{Cqbus1}, is 5 fF; the inverse of the bus coherence time, $1/T_{1bus1}$, is 5.2 kHz; and the bus coherence time, T_{1bus1}, is 31 μs. In retrospect, T_1 should have been optimized to reach times of 100 μs.

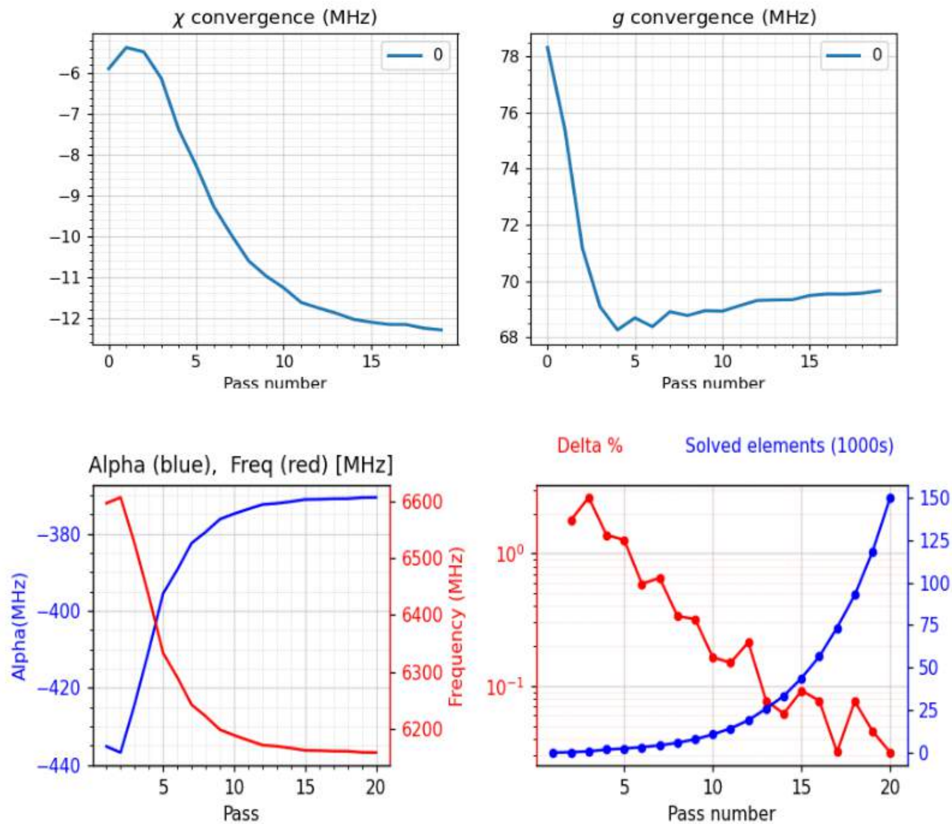

Figure 4.44: Here we have the convergence of the simulated qubit characteristics g, χ, charging energy (alpha), qubit frequency and delta. Capacitance Matrix simulation results acquired by ANSYS, these results are then processed using the LOM package for circuit quantization by Qiskit Metal.

Capacitor Simulation

We designed the chip to have a high Q cavity and and a coupled transmon of higher frequency with coupling factor g = 80 Mhz. This meant we would be able to observe the avoided crossing [49] by manipulating the qubit with applied magnetic flux. Furthermore we simulated the interdigitaded capacitors to have critical capacitance [64]. The results are displayed on the capacitance matrix on Table 4.6.

This ensures the waveguide is in a regime were the photon will spend some time within the cavity, enough to interact with our qubit. The coupling capacitance determines the cavities quality factor. A low

All values in fF	cap in	cap out
cap in	13.2	−3.2
cap out	−3.2	16.8

Table 4.6: Capacitance Matrix.

Q means the coupling capacitance is high and photons will have an easy time coming in and out of the cavity. A high Q cavity implies the photon will spend a long time within the cavity. At low Q photons will not spend enough time within the cavity for the experiment to evolve, very high Q cavities will be harder to measure. Therefore a critical coupling regime is required. The capacitors are simulated to find the frequency based capacitance and from this define if it is within the critical coupling regime. This enables the fabrication of cavities with expected values for quality factors.

4.5.3 Trilayer Circuit - Horseshoe Junction - Sample Characterization

Throughout the thesis we have developed fabrication techniques for the fabrication of Josephson junctions and Superconducting Circuits. Through the techniques described our fabrication run on a four inch wafer with many different circuits, for this measurement we had 7 samples of this type. They were then probed for yield of working junctions on the circuits border. This particular sample was chosen to be measured due to having the highest number of working junctions deposited in its outskirts.By analyzing the results of the room temperature resistance measurements which has a mean value of 24.7 kOhm, the predicted qubit frequency would be 5.17 ± 0.73 GHz as shown on Figure 4.46. The device had a yield of 26 out 27 junctions working 96% (Fig. 4.45).

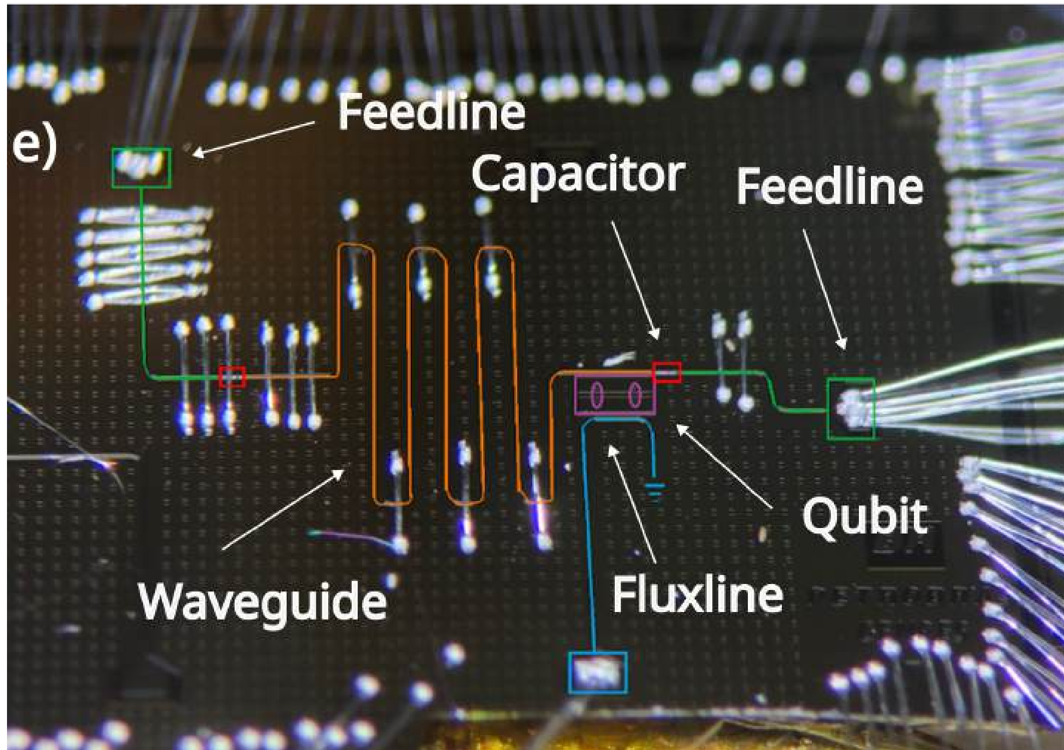

Figure 4.45: The circuit measured which contained 96% functioning junctions along the border. Green traces are feedlines, red squares indicated capacitors, orange is the waveguide, blue indicates the fluxline. Purple indicates the qubit.

Yield Analysis Horseshoe Junction

Resistance is a fundamental property in electronic circuits, and for Josephson junctions they indicate the transparency of the insulating barrier of Al_xO_y. Here we present data which was collected from the trilayer 1 qubit chip. In this analysis, we examine a set of resistance values measured from horseshoe junctions. The data consists of 23 resistance values, ranging from 17 to 48 kOhms. The mean resistance found on this chip is 24.7 kOhms, with a standard deviation of 7.8 kOhms. These values indicate the central tendency and spread of the resistance data, respectively. Figure 4.46 shows the histogram of the resistance values, with the x-axis representing resistance and the y-axis representing frequency. The histogram is divided into 15 bins to display the distribution of resistance values. This was the best sample our group has measured so far with 96% of working junctions and 30% standard deviation.

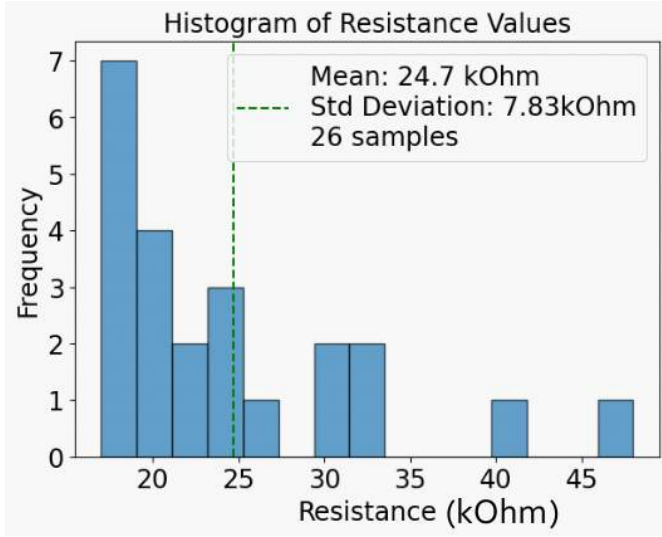

Parameters	**Simulated Transmon**
ω_q (GHz)	5.17 (6.03 - 4.44)
ω_c (GHz)	4.9
EC (MHz)	323
EJ (GHz)	11.7
$gbus1_in_MHz$ (MHz)	70
χ (MHz)	10

Figure 4.46: Left: Histogram of Resistance (kOhms) Values for the 26 samples which had resistance greater than zero, with mean value of 24.7 kOhm and standard deviation of 7.83 kOhm. On the right, updated predicted circuit values.

Milikelvin Measurements

Some of the capacitors of this batch were etched away during fabrication. While we have fixed this issue during the nanofabrication step by increasing resist stack height. We chose to proceed with these circuits by exposing new capacitors during the nano-lithography step, this resulted in a decreased quality factor.

The sample was glued to the sample holder with cryowax and wire-bonded to the copper contacts. On Figure 4.47 we show a complete device, we can see on Figure 4.47a progressive zoom into the circuit using a SEM, which amplifies down to the Josephson junction within the qubit on Figure 4.47d. This sample showed some metallic residue over the Si substrate, which was probably the defect in this particular sample and why the reason for measuring bad junctions in this circuit.

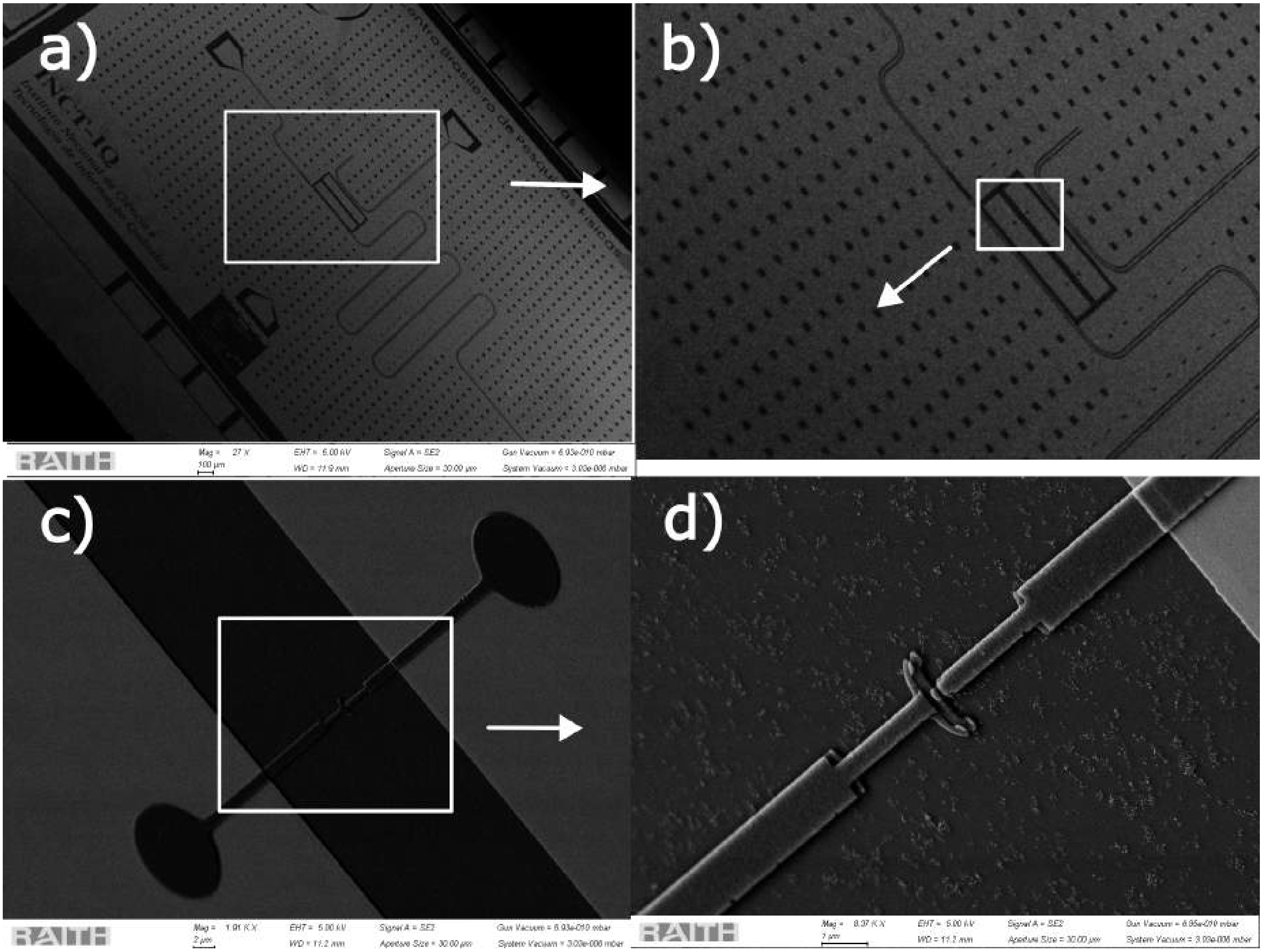

Figure 4.47: Circuit fabricated using trilayer technique and horseshoe EBL pattern. a-d) progressive zoom SEM images of the circuit and the deposited Josephson Junction, this circuit was discarded during inspection and we can see that junction is fine bur the surface has some sort of metallic residue.

Moving on to the measurements, at mK temperature range we were able to characterize the qubit in terms of its frequency, which enables us to calculate Josephson energy and charging energy. We first measured a power sweep which showed the cavity dressed mode at 4387 MHz which is seen on Figure 4.48. Furthermore we see that the by applying flux to the qubit we showed the transition from bare to dressed on Figure 4.48 right. This shows evidence of a functioning qubit. From these curves we were able to map out the energy levels of the qubit cavity system. We were also able to verify that the junctions had similar resistances, since the cavity and bare mode oscillated periodically for both the negative and positive voltages.

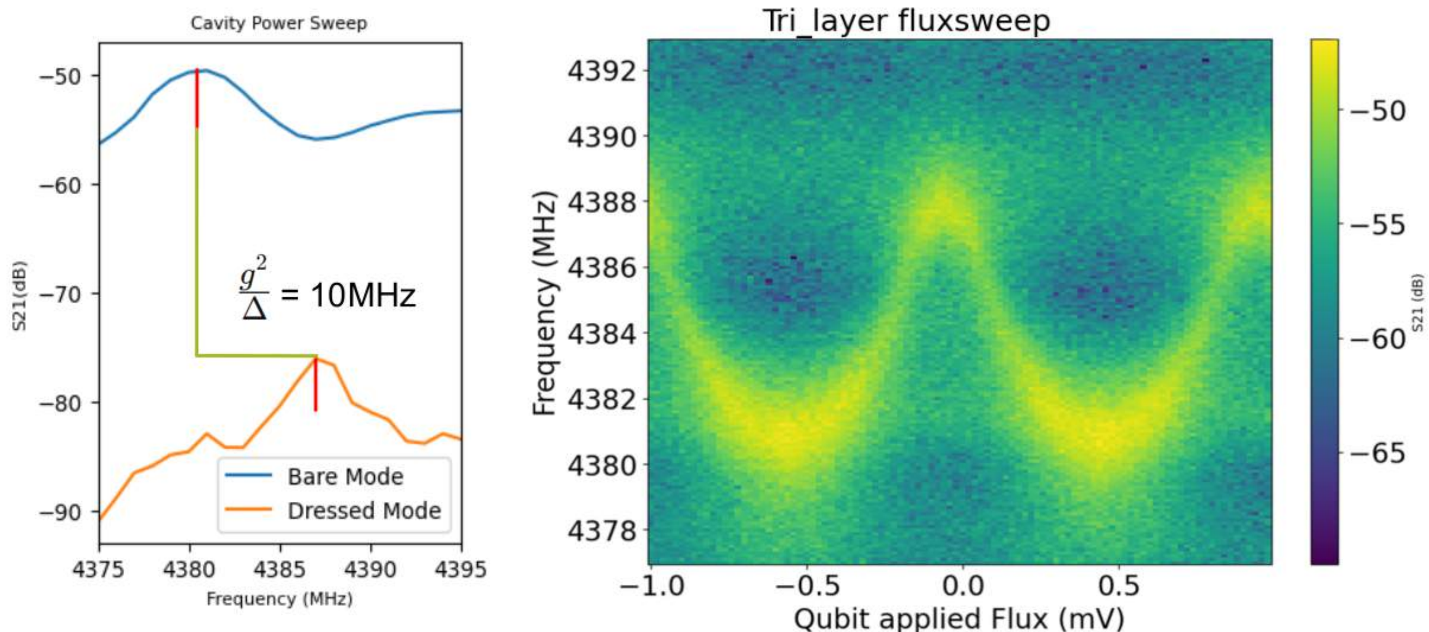

Figure 4.48: On the left side we see the cavity dressed and bare mode, we would hope to see two Lorentzian curves, however we suspect this specific sample had a damaged capacitor. Nonetheless two resolved peaks can be seen and $\chi = 10$ MHz. On the right side a flux sweep is performed, demonstrating the attenuation of the Josephson energy using magnetic flux.

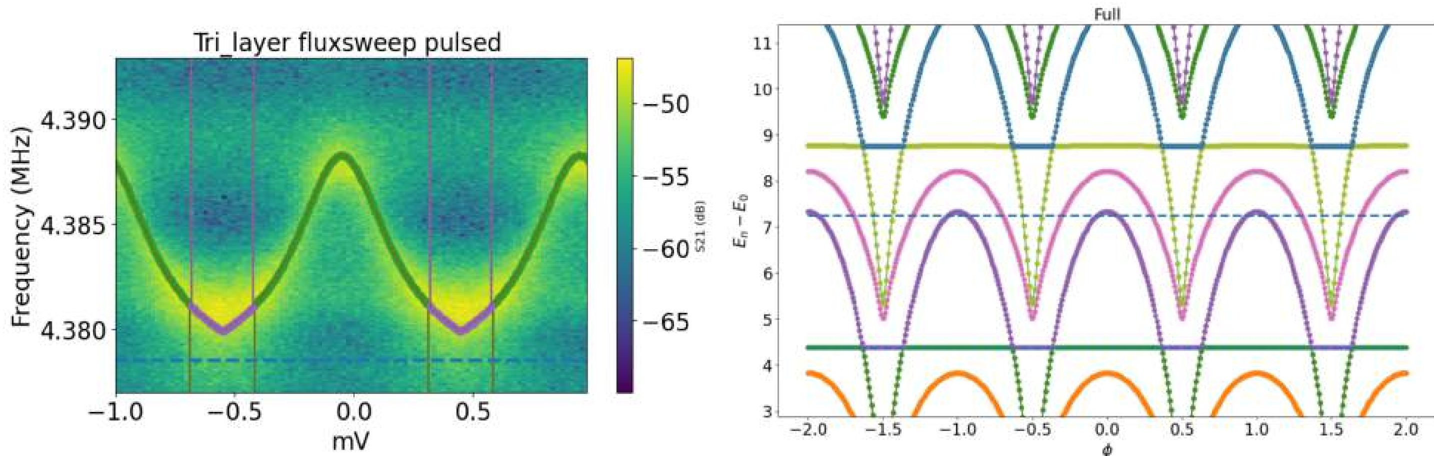

Figure 4.49: Left image shows bare to dressed mode oscillation due to applied flux, fitted with Qutip model. Left image displays the full energy spectrum derived from the fitting of the observed spectrum.

The flux sweep measurement will allow us to characterize the qubit. From this curve it is possible to fit the Jaynes Cummings Hamiltonian in the dispersive regime. To fit this curve, Qutip [66, 67] Python open source library was used. Essentially the Jaynes Cummings hamiltonian is simulated. The initials

values are the expected values from prior simulations and gradually adjusted by making small changes to Josephson Energy E_J, qubit frequency w_q, coupling strength g, and charging energy E_C. Once the curve is properly fit the whole energy spectrum for the coupled system is resolved.

The results are displayed on Table 4.7. The most discrepant value here is the qubit frequency. It is known that oxygen will diffuse within the Josephson junction raising its characteristic impedance. Since the sample was fabricated a measured two weeks later, this time drift caused the qubit frequency to decrease from expected values [79]. The cavity resonance was also a bit distant. We believe the difference in cavity frequency is a result of trilayer thin film configuration which may have altered the expected phase velocity. The charging energy and cavity coupling agree well with simulated results.

Parameters	**Simulated Transmon**	**Measured Transmon**
ω_q (GHz)	5.17 (6.03 - 4.44)	3.85
ω_c (GHz)	4.9	4.38
E_C/h (MHz)	323	300
E_J/h (GHz)	11.7	7.2
$gbus$/h (MHz)	70	73
χ (MHz)	18	10

Table 4.7: Final results of measured transmon.

Chapter 5

Conclusions and Perspectives

We have demonstrated in this thesis the difficulties inherent to fabrication techniques for superconducting circuits and Dolan techniques involving Josephson Junctions. We have shown the differences of many types of circuits as well as displayed the special care that must be taken at different steps of the photolithography microfabrication process. Furthermore we have gone in depth into the realm of working with double layered resists for Dolan technique Josephson junctions fabrication. Provided guidelines for testing and optimization of nanolithography recipes.

Furthermore we showed practical comparisons for working with different configurations of Al and Nb. Presented challenges and advantages of each film from a nanofabrication standpoint. For Josephson junctions we compared recipes, analyzed results, provided working solutions and went on to describe the reasoning behind failed passed attempts. Enabling the wide comprehension of the applied methodology and the prediction of new methods for the 30 kV Dolan technique.

The recipe for the trilayer circuits was only barely finished when the trilayer-qubit samples from Section 4.5.2 were measured. There was an issue of over etching and the capacitor was slightly damaged, we chose to attempt a measurement by depositing a new capacitor together with the Josephson junction, unfortunately this resulted in a cavity with low quality. And to make matters worse the Edwards Scroll Pump gave in shortly after the measurement, and the Dilution Refrigerator underwent a 5 month maintenance period. Nevertheless we aim to have provided fertile ground for a rapid increase in the number of active qubits and begin setting up standards for T_1 and T_2. From a fabrication standpoint we have provided templates for many circuits to be tested. Amplifiers and chips with superconducting qubits. A road map to a 4 qubit QPU.

5.1 Four Qubit QPU Perspectives

When increasing the number of qubits the we chose X transmons [80] for the practical implementation of their geometry into the desired circuit features. Our chip has four qubits multiplexed onto a feed line. Each cavity has a distinct length, and consequently a distinct resonance frequency. Allowing for multiplexed measurement of the qubits. Each qubit has a flux line, allowing each qubit to be tuned individually. In this case we also have flux lines leading up to qubits which will be used as couplers, this way couplers can be brought to coupling regimes or tuned to act as isolators instead of couplers. Detailed description can

be seen on Figure A.1.

5.1.1 Chip Fabrication

We fabricated the 4 qubit QPU chip in trilayer fabrication technique, and applied the horseshoe junction EBL pattern. While we do not have the means of testing the circuit we present some fabrication results and images to show we have the means of fabricating such a device.

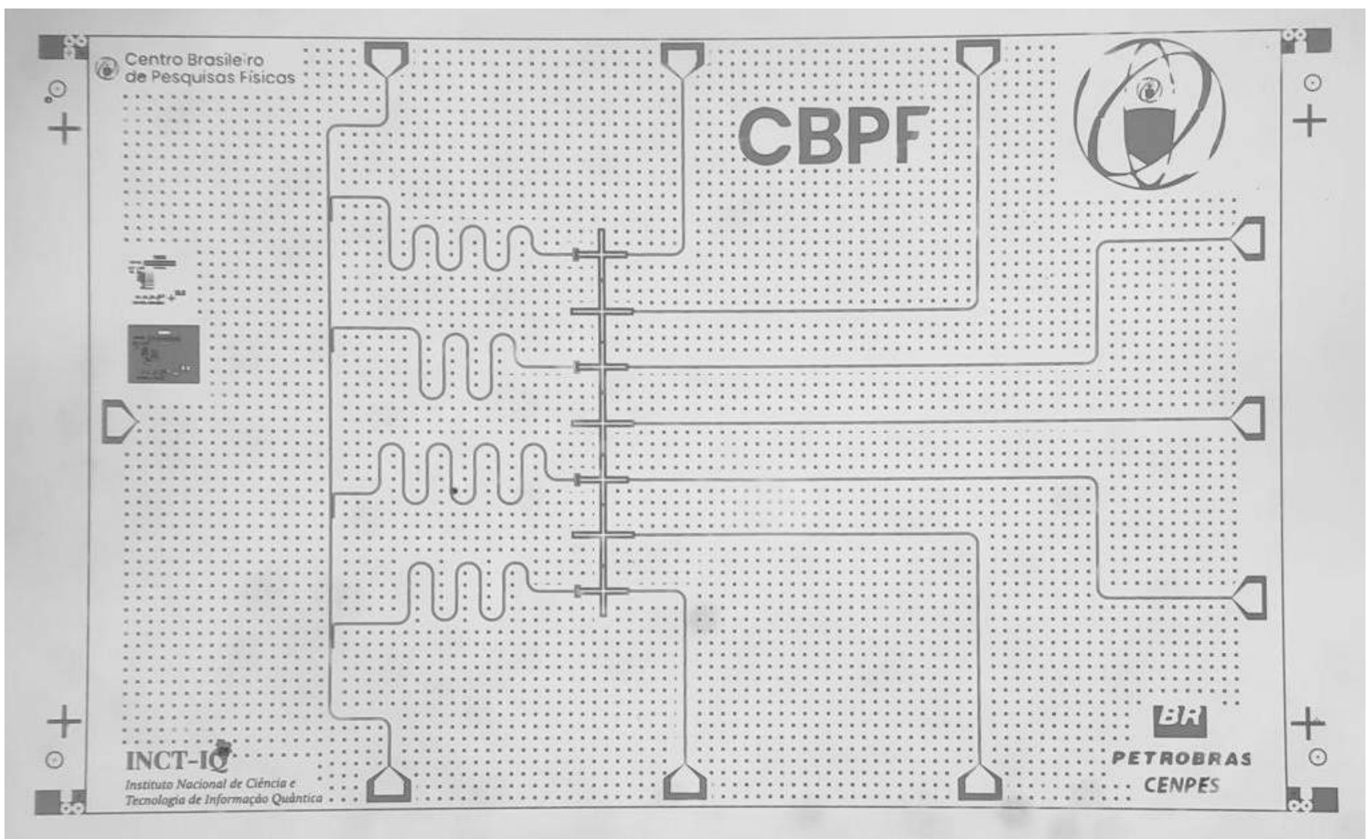

Figure 5.1: Four qubit Quantum Processing Unit, designed and fabricated.

5.2 Accomplishments

- Thorough explanation of the 30kV e-beam process used to fabricate resist bridge like structures.
- Thorough analysis of Josephson junction fabrication through:
  - Most importantly the definition of various methods to standardize the production and inspect the quality of the fabrication process.
  - SEM analysis of patterned resist structure.

  - SEM images of deposited junctions.
  - Statistical analysis and description of the 30kV e-beam properties, and how they affect undercuts and bridge like structures.
  - Simulations of 30 kV e-beam applied to different geometries.
  - Predicted the outcomes of certain geometries and compared them to real results observed in the laboratory.
  - Room temperature resistance measurements.

- Fabrication of an array of 10 Josephson Junctions, verified functionality through room temperature resistance measurements.
- Fabrication SQUID device enclosing a small area of 10 μm by 10 μm.
- Optimization of the technical aspect of 30kV e-beam process to fabricate Josephson junctions used to fabricate resist bridge like structures.
- Developed a new geometry with 96% reproducibility.
- Described how this study may be continued and further improved by separating the simple patterning from undercut generation by designating regions within the geometry to produce backscattered electrons.
- Development of 6 types of superconducting circuits through the application and optimization of nanofabrication procedures.
  - Optimization of photo lithography recipes.
  - Development of overlay procedures for photo lithography recipes.
  - Optimization of wet etching recipes.
  - Optimization of dry etching recipes.
  - Techniques for multi-layer etching.
- Simulations of superconducting qubits, cavities, amplifiers.
- Fabrication of superconducting qubits, cavities, amplifiers.
- Fabrication quality analysis of superconducting circuits through SEM images, Energy-dispersive X-ray spectroscopy and perfilometry.
- Measurement of superconducting qubit coupled to a 1 dimensional microwave cavity.
  - Simulation of cavity coupling, qubit frequency, and cavity frequency, anharmonicity and state dependent cavity shift χ.
  - Tri-layer Si/Al/Nb/Al superconducting circuit recipe development.

- Horseshoe Josephson junctions.
- Measurement of bare and dressed cavity state and flux modulation of the qubit.

- Patent deposited
  - 2024 - BR 1020240127714 - “HORSESHOE - TYPE JOSEPHSON JUNCTION DEVICE AND METHOD FOR MANUFACTURING THE DEVICE” - Authors: Arthur M. Rebello, Ivan S. Oliveira, João P. Sinnecker.

- Associated publication

Article

Optimizing Josephson Junction Reproducibility in 30 kV E-Beam Lithography: An Analysis of Backscattered Electron Distribution

Arthur M. Rebello [1,†], Lucas M. Ruela [2,†], Gustavo Moreto [2], Naiara Y. Klein [1], Eldues Martins [3], Ivan S. Oliveira [1], João P. Sinnecker [1,*] and Francisco Rouxinol [2,*]

[1] Coordenação de Matéria Condensada, Física Aplicada e Nanociência (COMAN), Centro Brasileiro de Pesquisas Físicas (CBPF), Rio de Janeiro 22290-180, RJ, Brazil; artrebello@cbpf.br (A.M.R.); naiaraklein@gmail.com (N.Y.K.); ivan@cbpf.br (I.S.O.)
[2] Quantum Device Physics Laboratory, Universidade Estadual de Campinas (Unicamp), Instituto de Física Gleb Wataghin (IFGW), Campinas 13083-859, SP, Brazil; lucasmr@ifi.unicamp.br (L.M.R.); g169380@dac.unicamp.br (G.M.)
[3] Leopoldo Américo Miguez de Mello Research, Development and Innovation Center (CENPES), Rio de Janeiro 21941-915, RJ , Brazil; eldues@petrobras.com.br (E.M.)
* Correspondence: sinnecker@cbpf.br (J.P.S.); rouxinol@ifi.unicamp.br (F.R.)
† These authors contributed equally to this work.

Abstract: This paper explores methods to enhance the reproducibility of Josephson junctions, which are crucial elements in superconducting quantum technologies, when employing the Dolan technique in 30 kV e-beam processes. The study explores the influence of dose distribution along the bridge area on reproducibility, addressing challenges related to fabrication sensitivity. Experimental methods include e-beam lithography, with electron trajectory simulations shedding light on the behavior of backscattered electrons. Wedescribe the fabrication of various Josephson junction geometries and analyze the correlation between the success rates of different lithography patterns and the simulated distribution of backscattered electrons. Our findings demonstrate a success rate of up to 96.3% for the double-resist 1-step low-energy e-beam lithography process. As a means of implementation strategy, we provide a geometric example that takes advantage of simulated stability regions to administer a controlled, uniform dose across the junction area, introducing novel features to overcome the difficulties associated with fabricating bridge-like structures.

Citation: Rebello, A.M.; Ruela, L.M.; Moreto, G.; Klein, N.Y.; Martins, E.;

5.2.1 Acknowledgements

1) FAPERJ PROCESSO E-26/010.000980/2019 (NANO DEVICE NETWORK)
2) The electron microscopy/nanolithography work has been performed with the JSM 6490-LV / RAITH e-Line / JEM 2100F microscope(s) of the LABNANO/CBPF, Rio de Janeiro.
3) FAPERJ/CBPF/CNE project E26/200.830/2021
4) FAPERJ TEMATICO E-26/211.391/2021
5) LFDQ - Quantum Devices Physics Laboratory - FAPESP grant number 2017/08602-0 and 2021/01066-1, NAMITEC , National Council for Scientific and Technological Development – CNPq - 406193/2022-3
6)A. M. Rebello and N. Y. Klein, acknowledge FAPERJ and PETROBRAS for partially financing this project.
7)Scholarship for productivity and research process - CNPq- 305431/2022-6

5.2.2 Abbreviations

QPU	Quantum Processing Unit
PEC	Proximity Effect Correction
PSF	Point Spread Function
RIE	Reactive Ion Etching
cQED	cavity Quantum Electrodynamics
UHV	Ultra High Vacuum
EBL	Electrom Beam Lithography
PMMA	Poly(methyl methacrylate)
MMA	Methyl methacrylate

Appendix A

Four qubit Quantum Processing Unit

The laboratory to be built in our facility (CBPF) would have everything necessary to measure and operate this chip. Here we display a GDS file image of the 4 qubit chip which was designed and simulated by us.

In the figure a red square shows a cell with the main components, a microwave cavity, qubit and coupler (Fig. A.1). Next we show the gds file with positioned Josephson junctions, and proceed to show SEM images displaying the fabricated device.

To be sure of the quality of the circuits we perform Electron Diffraction Spectroscopy EDS to show were able to correctly etch the trilayer material shown on Figure A.3. Lastly we demonstrate the layout of the circuit configuration for the measurement and operation of such a device Fig A.4.

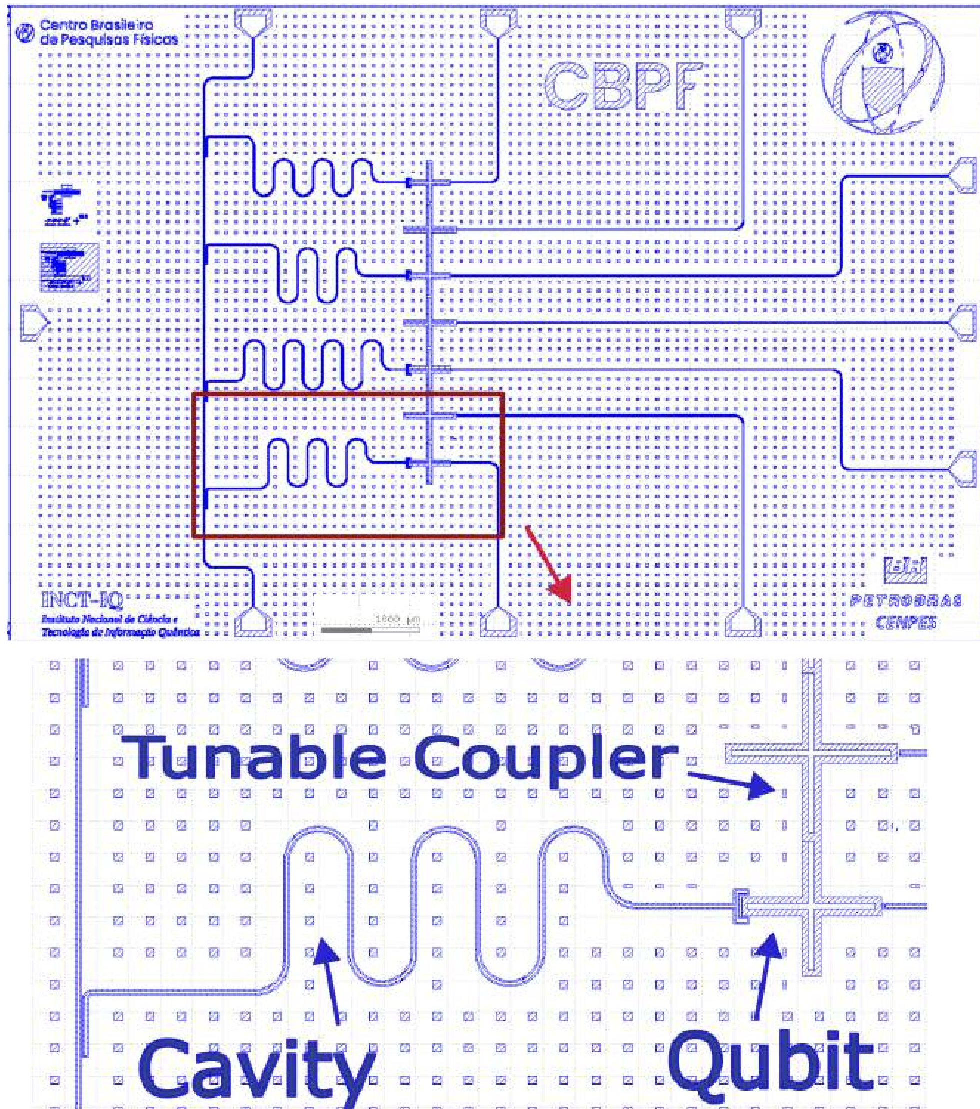

Figure A.1: Top image displays full lay out of the Four Qubit Tunable Coupler chip. In the bottom image we see a zoomed in view of the main components.

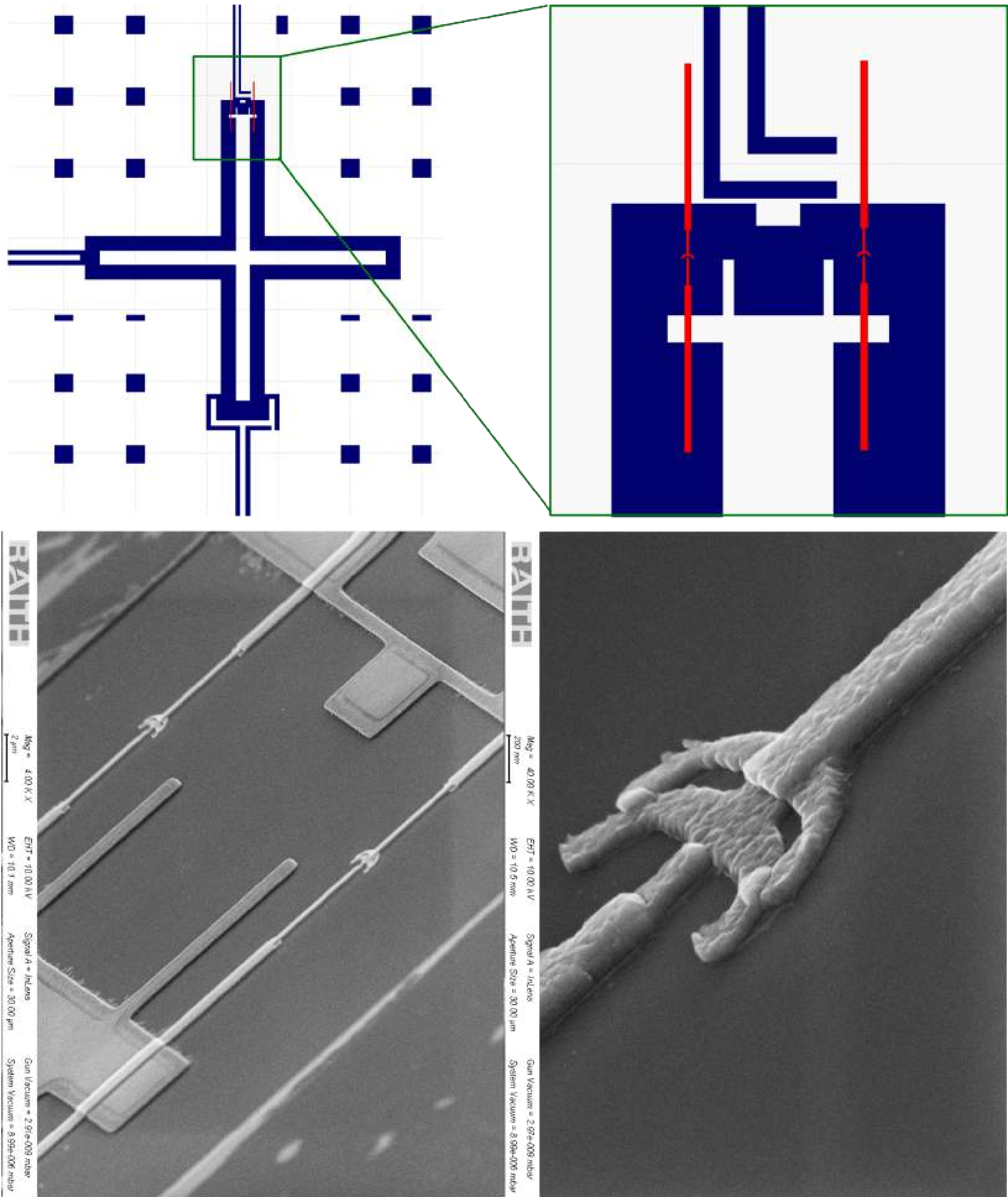

Figure A.2: Top left displays gds file for x transmon, top right shows zoom in to Josephson Junction area. Bottom left shows SEM image of fabricated device with deposited Josephson junctions Bottom right shows zoom in to horseshoe junction.

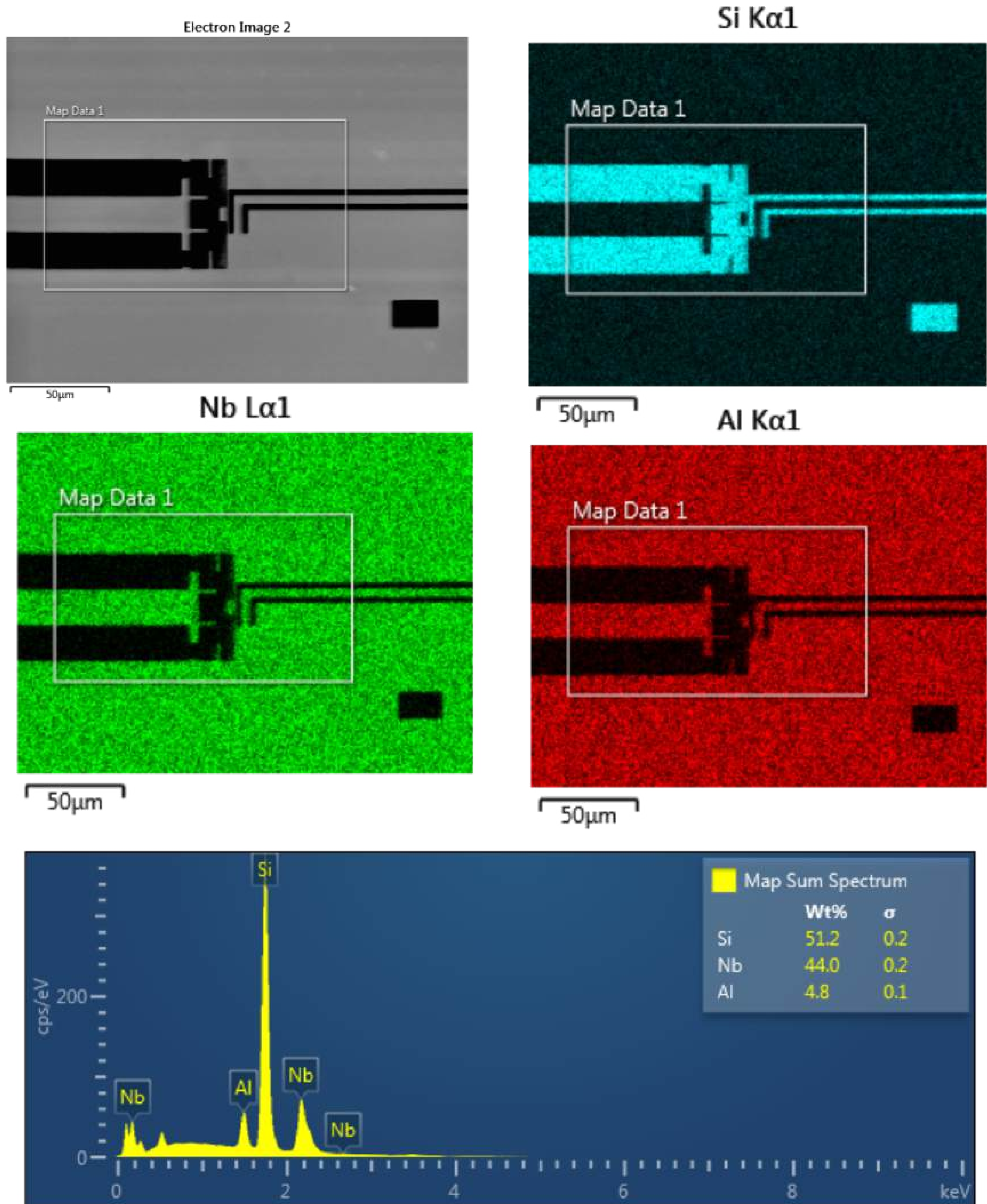

Figure A.3: EDS Analysis of Josephson junction deposition region. Analysis shows that all contacts are properly isolated, furthermore the Si substrate is free from Al or Nb contamination.

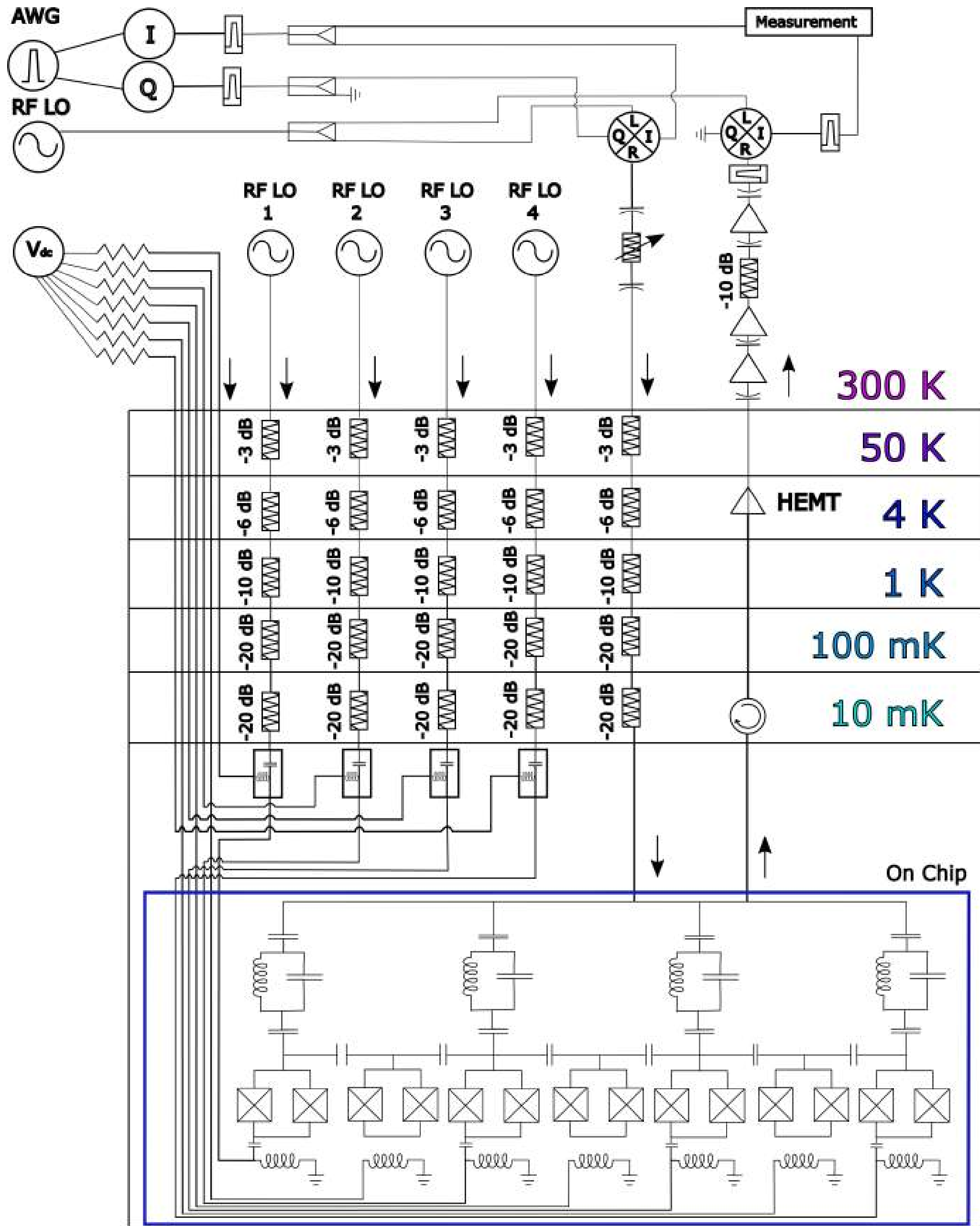

Figure A.4: Four qubit QPU experimental set-up. In this set-up each qubit is coupled to a cavity, making a total of four multiplexed microwave cavities. The qubit control is done using a bias-T to apply microwave signals and current through the same feed line. Furthermore an additional three feed lines are used to tune couplers which can be switched on or off, connecting or isolating the qubits.

Appendix B

Superconducting Circuits

Here we display other circuits which were simulated and fabricated during the development of this Thesis. On Figure B.1 we display the sample which was used for room temperature probing of Josephson junctions. Next we show chips with applications in quantum computing. The first chip is simplest means of achieving entanglement of two qubits following the steps of [4] (Fig. B.3 top). One waveguide is used to couple two qubits by bringing them into the same resonance by using the flux lines to modify their total energy. The second circuit does the same, but by having a tunable coupler [5, 8] (Fig. B.3 bottom) element instead of using the cavity to mediate the interaction, now qubits can effectively sealed off by putting the variable coupler at a distant frequency. This circuit can be improved to a more modern design [9]. The third circuit is a KITWPA, the design was similar to the one used in [6](Fig. B.3 top), we modified it because we had access to better lithography equipment, therefore we were able to shrink down features. There have been many other advances in the area [81, 82] and there is much room for improvement. Impedance matching had to be accounted for, the circuit is displayed on Figure B.3 bottom. The fourth circuit is a couple of multiplexed qubits and photonic crystal. The idea was derived from the paper by [7], however this crystal has strong inductive coupling.

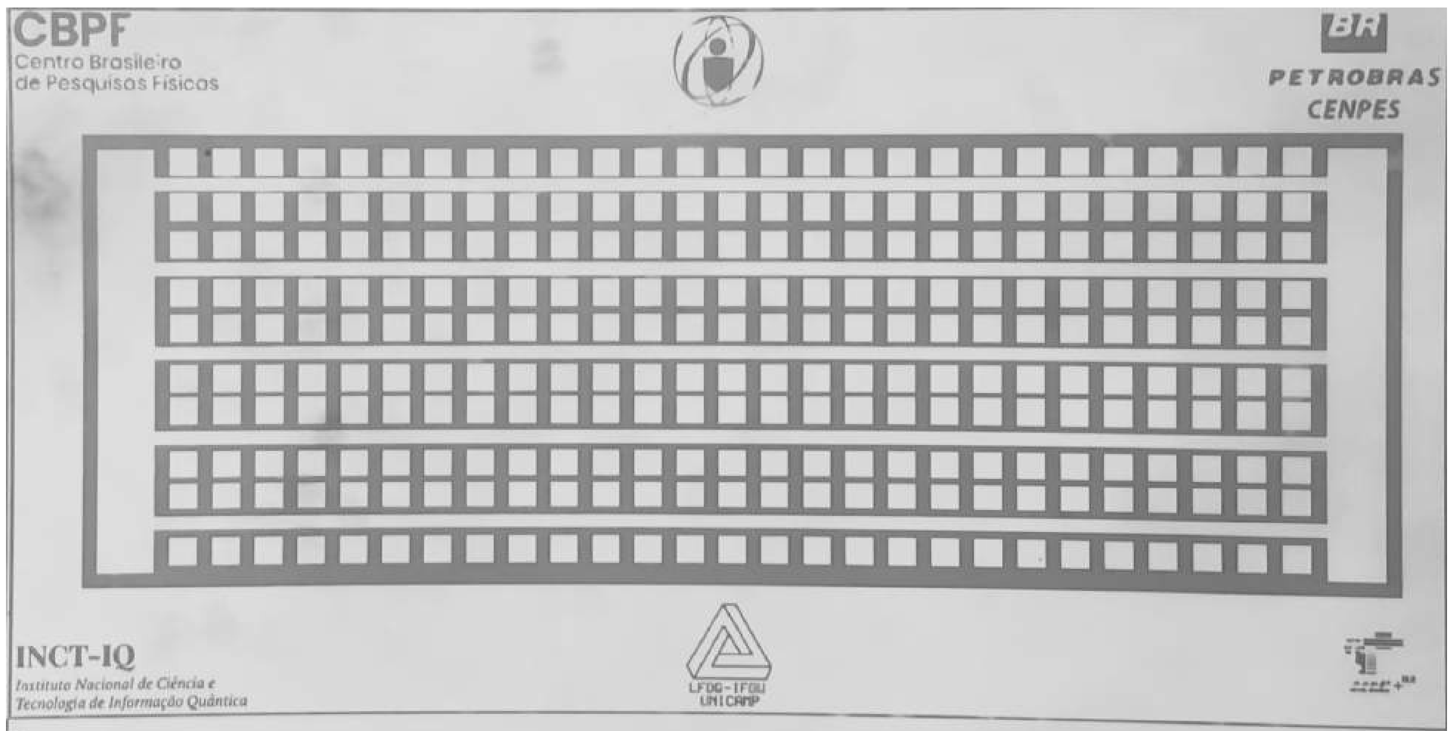

Figure B.1: Metallic pads for Josephson junction probing at room temperature. The design allows for one probe to stay stationary while the pads are probed.

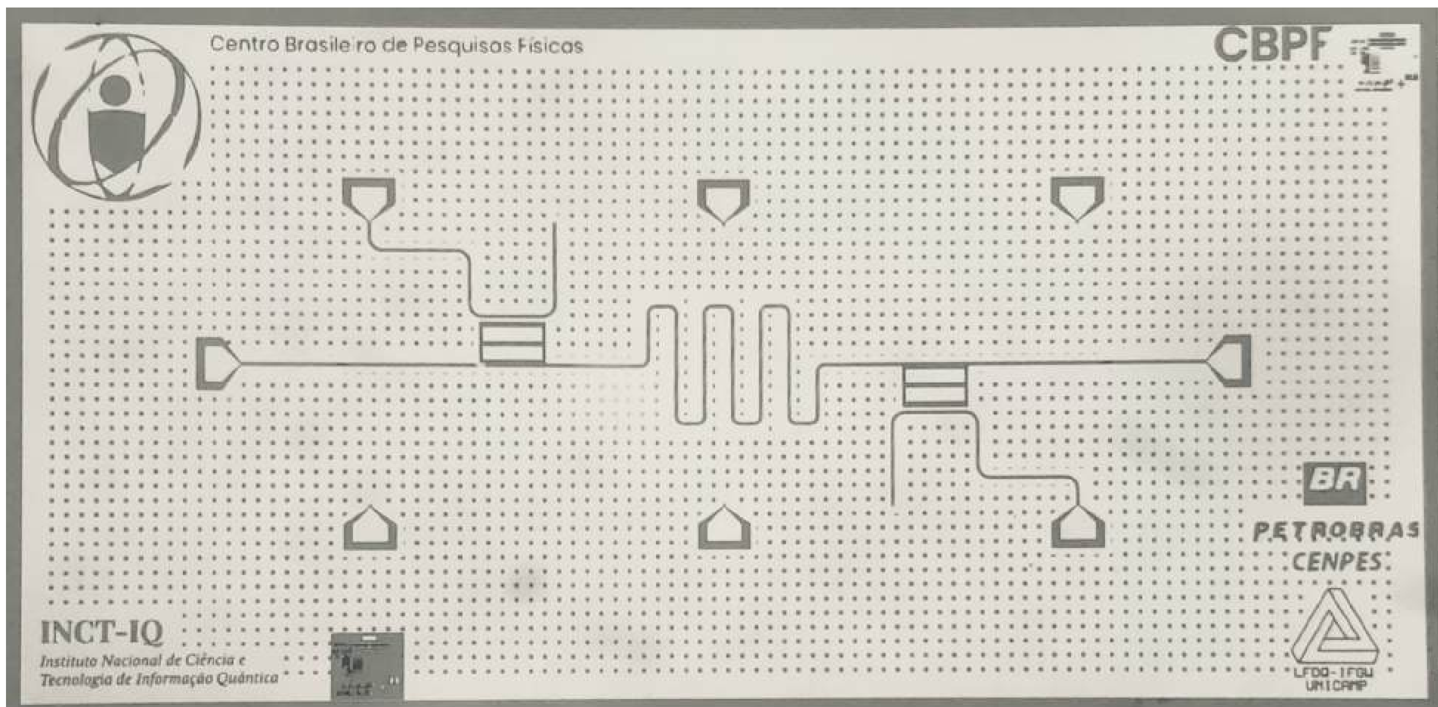

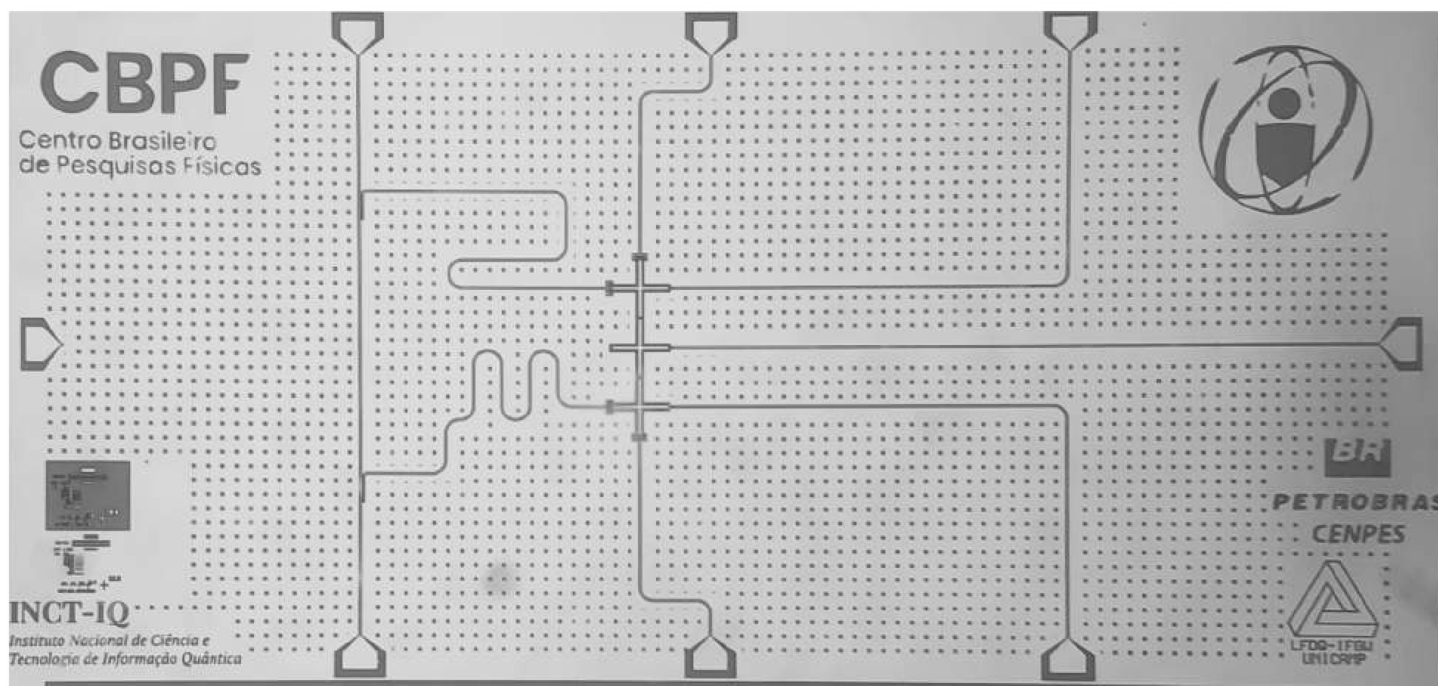

Figure B.2: Top: Circuit with two transmon pocket qubits and one half wave capacitively coupled microwave cavity. Bottom: Two Xmon qubits connected by a third qubit serving as variable coupler.

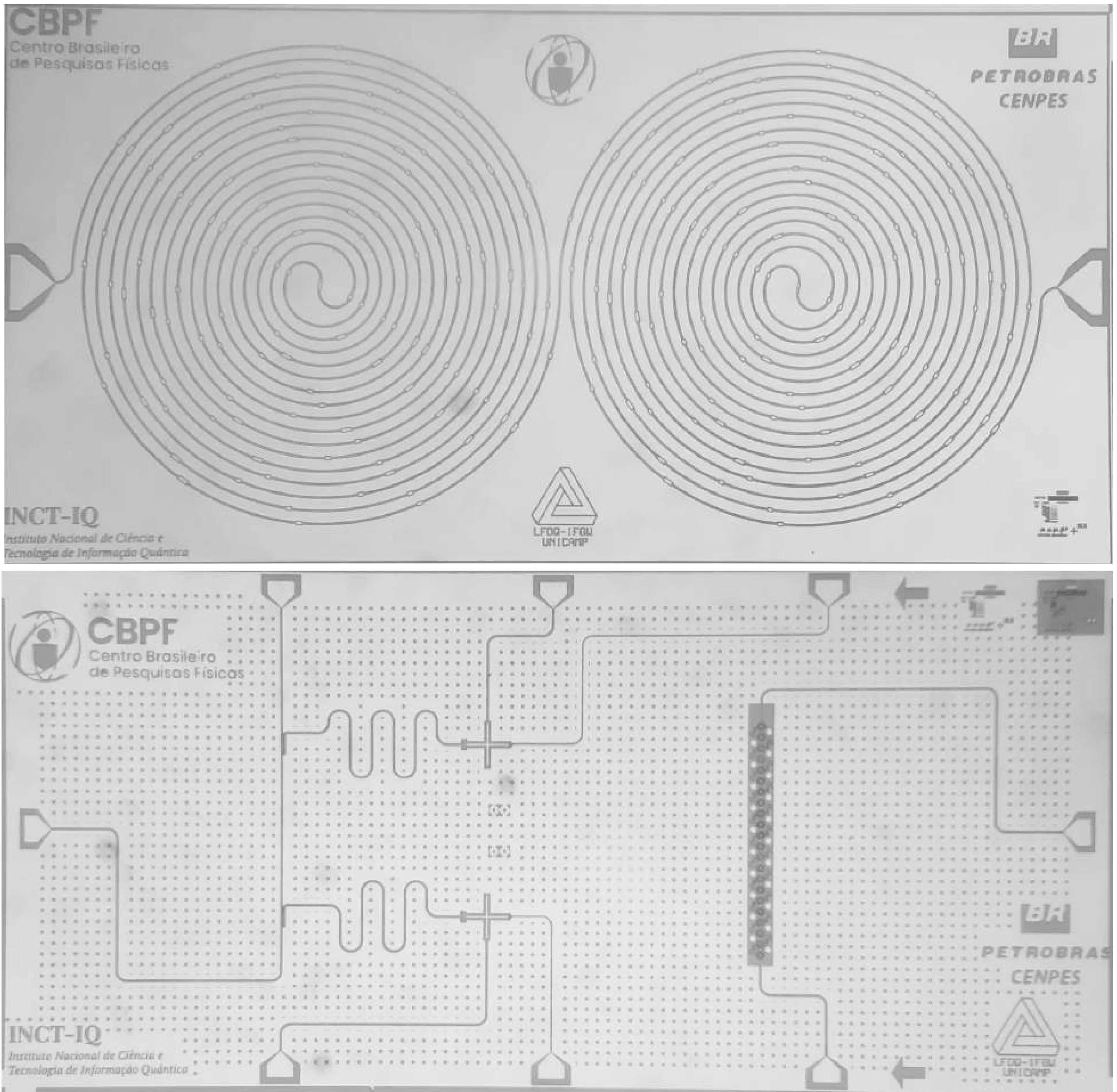

Figure B.3: Top: KITWPA Bottom: Circuit with two multiplexed Xmons qubits multiplexed to a feed line and a photonic crystal on the right side.

Appendix C

Trilayer Al/Nb/Al Circuit Recipe

It should be noted that a possible improvement of this recipe would be to eliminate wet etching steps with dry etching, by using a different chemistry to etch away aluminum using RIE.

Reagents:

- Resist: AR-P 3120 (3 ml)
- Developer: AR-P 300-26 (ratio 1 : 3 H2O) (500 ml)
- Stopper: H2O (200 ml)
- Acetone, IPA

Process Recipes

- Ion milling – 30s
- Al e-beam deposition rate of 1 A/s, at UHV (10^{-8} Torr).
- Nb magnetron sputtering deposition rate 1 nm/s, 3 mTorr.
- Nb plasma reactive ion etching 5 sccm SF6, 3.5 sccm Ar, 30 W, 30 mTorr.
- Al wet etching Phosphoric acid : Acetic acid : Nitric acid : Water (73:3:3:21), 100ml.

Procedure

1. Start with clean 4 in high resistivity wafer
2. Wafer must be kept within UHV for steps 3-6.

3. Ion milling 60s
4. Al deposition 20 nm
5. Nb deposition 80 nm
6. Al deposition 20 nm
7. Apply photoresist 3500 rpm (24±2 Celsius)
8. Soft bake at 100 C for 60s
9. Cold plate 30s
10. Expose
11. Develop in at least 500 ml of developer as it reacts to Al film and could cause re-deposition. Also, it is useful to develop the wafer upside down.
12. Rinse using H2O 200 ml
13. Spin or N2 dry, then perform after bake at 110 C for 60s
14. Cold plate 30s
15. Dip in acid until looks evenly etched and then place in ultrasound for 5 seconds
16. Rinse in 3x using H2O 200ml
17. Spin or N2 dry, then bake at 110 for 30s to remove excess water
18. Cold plate 30s
19. Inspect – if necessary repeat
20. SF6 plasma reactive ion etching 6.5 min should be enough. 30 W / 30 mtorr / 5 sccm SF6 / 3.5 sccm Ar
21. Inspect – if necessary repeat
22. Dip in acid until looks evenly etched and then place in ultrasound for 5 seconds
23. Rinse in 3x using H2O 200ml
24. Spin or N2 dry, then bake at 110 for 30s to remove excess water
25. Cold plate 30s
26. Inspect – if necessary repeat

27. Lift off using 70 C acetone for 1 min then 3 min ultrasound.
28. To remove the acetone use Isopropyl Alcohol, 3 min ultrasound
29. Spin or N2 dry, then bake at 110 for 30s to remove excess water
30. Cold plate 30s

Bibliography

[1] "127-qubit quantum processor: Meet eagle," https://www.ibm.com/quantum/blog/127-qubit-quantum-processor-eagle, accessed on 2024-04-20.

[2] A. Wallraff, D. I. Schuster, A. Blais, L. Frunzio, R.-S. Huang, J. Majer, S. Kumar, S. M. Girvin, and R. J. Schoelkopf, "Strong coupling of a single photon to a superconducting qubit using circuit quantum electrodynamics," *Nature*, vol. 431, no. 7005, p. 162–167, Sep. 2004. [Online]. Available: http://dx.doi.org/10.1038/nature02851

[3] H. Zu, W. Dai, and A. de Waele, "Development of dilution refrigerators—a review," *Cryogenics*, vol. 121, p. 103390, 2022. [Online]. Available: https://www.sciencedirect.com/science/article/pii/S001122752100148X

[4] J. Majer *et al.*, "Coupling superconducting qubits via a cavity bus," *Nature*, vol. 449, no. 7161, pp. 443–447, 09 2007. [Online]. Available: https://doi.org/10.1038/nature06184

[5] M. C. Collodo, J. Herrmann, N. Lacroix, C. K. Andersen, A. Remm, S. Lazar, J.-C. Besse, T. Walter, A. Wallraff, and C. Eichler, "Implementation of conditional phase gates based on tunable zz interactions," *Phys. Rev. Lett.*, vol. 125, p. 240502, Dec 2020. [Online]. Available: https://link.aps.org/doi/10.1103/PhysRevLett.125.240502

[6] S. Zhao, "Physics of superconducting travelling-wave parametric amplifiers," Ph.D. dissertation, Department of Physics, University of Cambridge, September 2021, this dissertation is submitted for the degree of Doctor of Philosophy, Corpus Christi College.

[7] M. Scigliuzzo, G. Calajò, F. Ciccarello, D. Perez Lozano, A. Bengtsson, P. Scarlino, A. Wallraff, D. Chang, P. Delsing, and S. Gasparinetti, "Controlling atom-photon bound states in an array of josephson-junction resonators," *Phys. Rev. X*, vol. 12, p. 031036, Sep 2022. [Online]. Available: https://link.aps.org/doi/10.1103/PhysRevX.12.031036

[8] Y. Sung *et al.*, "Realization of high-fidelity cz and zz-free iswap gates with a tunable coupler," *Phys. Rev. X*, vol. 11, p. 021058, Jun 2021. [Online]. Available: https://link.aps.org/doi/10.1103/PhysRevX.11.021058

[9] D. L. Campbell, A. Kamal, L. Ranzani, M. Senatore, and M. D. LaHaye, "Modular tunable coupler for superconducting circuits," *Physical Review Applied*, vol. 19, p. 064043, 2023.

[10] G. J. Mooney, C. D. Hill, and L. C. L. Hollenberg, "Entanglement in a 20-qubit superconducting quantum computer," *Scientific Reports*, vol. 9, no. 1, p. 13465, 2019. [Online]. Available: https://doi.org/10.1038/s41598-019-49805-7

[11] F. Arute *et al.*, "Quantum supremacy using a programmable superconducting processor," *Nature*, vol. 574, no. 7779, pp. 505–510, 10 2019. [Online]. Available: https://doi.org/10.1038/s41586-019-1666-5

[12] I. Q. Research. (2022) Quantum volume: A comprehensive guide. Accessed: January 8, 2024. [Online]. Available: https://research.ibm.com/blog/quantum-volume-256

[13] M. Brooks, "Beyond quantum supremacy: the hunt for useful quantum computers," *Nature*, vol. 574, no. 7776, pp. 19–21, 2019.

[14] C. Davisson and L. H. Germer, "Diffraction of electrons by a crystal of nickel," *Phys. Rev.*, vol. 30, pp. 705–740, Dec 1927. [Online]. Available: https://link.aps.org/doi/10.1103/PhysRev.30.705

[15] J. Verstraten, K. Dai, M. Dixmerias, B. Peaudecerf, T. de Jongh, and T. Yefsah, "In-situ imaging of a single-atom wave packet in continuous space," 2024.

[16] P. Jurcevic *et al.*, "Demonstration of quantum volume 64 on a superconducting quantum computing system," *Quantum Science and Technology*, vol. 6, no. 2, p. 025020, mar 2021. [Online]. Available: https://dx.doi.org/10.1088/2058-9565/abe519

[17] R. Acharya *et al.*, "Suppressing quantum errors by scaling a surface code logical qubit," 2022.

[18] D. Cozzolino, B. Da Lio, D. Bacco, and L. K. Oxenløwe, "High-dimensional quantum communication: Benefits, progress, and future challenges," *Advanced Quantum Technologies*, vol. 2, no. 12, p. 1900038, 2019. [Online]. Available: https://onlinelibrary.wiley.com/doi/abs/10.1002/qute.201900038

[19] M. Rademacher, J. Millen, and Y. L. Li, "Quantum sensing with nanoparticles for gravimetry: when bigger is better," *Advanced Optical Technologies*, vol. 9, no. 5, pp. 227–239, 2020. [Online]. Available: https://doi.org/10.1515/aot-2020-0019

[20] E. D. Walsh, W. Jung, and G.-H. e. a. Lee, "Josephson junction infrared single-photon detector," *Science*, vol. 372, no. 6540, p. 409–412, Apr 2021. [Online]. Available: http://dx.doi.org/10.1126/science.abf5539

[21] M. Rademacher, J. Millen, and Y. L. Li, "Quantum sensing with nanoparticles for gravimetry: when bigger is better," *Advanced Optical Technologies*, vol. 9, no. 5, pp. 227–239, 2020. [Online]. Available: https://doi.org/10.1515/aot-2020-0019

[22] A. Ranadive, M. Esposito, L. Planat, E. Bonet, C. Naud, O. Buisson, W. Guichard, and N. Roch, "Kerr reversal in josephson meta-material and traveling wave parametric amplification," *Nature Communications*, vol. 13, no. 1, Apr. 2022. [Online]. Available: http://dx.doi.org/10.1038/s41467-022-29375-5

[23] J. M. Martinis *et al.*, "Decoherence in josephson qubits from dielectric loss," *Phys. Rev. Lett.*, vol. 95, p. 210503, Nov 2005. [Online]. Available: https://link.aps.org/doi/10.1103/PhysRevLett.95.210503

[24] A. Nersisyan *et al.*, "Manufacturing low dissipation superconducting quantum processors," 2019.

[25] A. A. Pishchimova, N. S. Smirnov, D. A. Ezenkova, E. A. Krivko, E. V. Zikiy, D. O. Moskalev, A. I. Ivanov, N. D. Korshakov, and I. A. Rodionov, "Improving josephson junction reproducibility for superconducting quantum circuits: junction area fluctuation," *Scientific Reports*, vol. 13, no. 1, p. 6772, 2023. [Online]. Available: https://doi.org/10.1038/s41598-023-34051-9

[26] T. Shiota, T. Imamura, and S. Hasuo, "Fabrication of high quality nb/alo/sub /x-al/nb josephson junctions. iii. annealing stability of alo/sub /x tunneling barriers," *IEEE Transactions on Applied Superconductivity*, vol. 2, no. 4, pp. 222–227, 1992.

[27] I. M. Pop, T. Fournier, T. Crozes, F. Lecocq, I. Matei, B. Pannetier, O. Buisson, and W. Guichard, "Fabrication of stable and reproducible submicron tunnel junctions," *Journal of Vacuum Science & Technology B*, vol. 30, no. 1, p. 010607, 01 2012. [Online]. Available: https://doi.org/10.1116/1.3673790

[28] S. Nik, P. Krantz, L. Zeng, T. Greibe, H. Pettersson, S. Gustafsson, P. Delsing, and E. Olsson, "Correlation between al grain size, grain boundary grooves and local variations in oxide barrier thickness of al/alox/al tunnel junctions by transmission electron microscopy," *SpringerPlus*, vol. 5, no. 1, p. 1067, 2016, pMID: 27462515. [Online]. Available: https://doi.org/10.1186/s40064-016-2418-8

[29] H. Kim *et al.*, "Effects of laser-annealing on fixed-frequency superconducting qubits," *Applied Physics Letters*, vol. 121, no. 14, p. 142601, 10 2022. [Online]. Available: https://doi.org/10.1063/5.0102092

[30] Y. Chen *et al.*, "Qubit architecture with high coherence and fast tunable coupling," *Phys. Rev. Lett.*, vol. 113, p. 220502, Nov 2014. [Online]. Available: https://link.aps.org/doi/10.1103/PhysRevLett.113.220502

[31] J. Kelly *et al.*, "State preservation by repetitive error detection in a superconducting quantum circuit," *Nature*, vol. 519, no. 7541, pp. 66–69, 2015. [Online]. Available: https://doi.org/10.1038/nature14270

[32] A. Dunsworth *et al.*, "Characterization and reduction of capacitive loss induced by sub-micron Josephson junction fabrication in superconducting qubits," *Applied Physics Letters*, vol. 111, no. 2, p. 022601, 07 2017. [Online]. Available: https://doi.org/10.1063/1.4993577

[33] C. J. Richardson, V. Lordi, S. Misra, and J. Shabani, "Materials science for quantum information science and technology," *MRS Bulletin*, vol. 45, p. 485, 2020.

[34] D. Lan, G. Xue, Q. Liu, X. Tan, H. Yu, and Y. Yu, "Fabrication of al/alox/al junctions using pre-exposure technique at 30-kev e-beam voltage*," *Chinese Physics B*, vol. 25, no. 8, p. 088501, jun 2016. [Online]. Available: https://dx.doi.org/10.1088/1674-1056/25/8/088501

[35] E. Xie, "Optimized fabrication process for nanoscale josephson junctions used in superconducting quantum circuits," Master's thesis, Munich, September 2013.

[36] J.-Z. Pan *et al.*, “Frequency-tunable transmon in a three-dimensional copper cavity *,” *Chinese Physics B*, vol. 24, no. 11, p. 110301, oct 2015. [Online]. Available: https://dx.doi.org/10.1088/1674-1056/24/11/110301

[37] H. Paik *et al.*, “Observation of high coherence in Josephson junction qubits measured in a three-dimensional circuit QED architecture,” *Physical Review Letters*, vol. 107, no. 24, p. 240501, 12 2011. [Online]. Available: https://link.aps.org/doi/10.1103/PhysRevLett.107.240501

[38] A. D’Elia *et al.*, “Characterization of a transmon qubit in a 3d cavity for quantum machine learning and photon counting,” *Applied Sciences*, vol. 14, no. 4, p. 1478, 2024.

[39] S. Skinner, R. Lewis, M. Eichenfield, and C. Harris, “Nanoscale Dolan Bridges with Integrated Stress Relief for Self-Aligned Josephson Junctions,” in *APS March Meeting Abstracts*, ser. APS Meeting Abstracts, vol. 2021, jan 2021, p. S47.014.

[40] J. S. Kelly, “Fault-tolerant superconducting qubits,” Doctoral dissertation, University of California, Santa Barbara, Santa Barbara, CA, March 2015, submitted in partial satisfaction of the requirements for the degree of Doctor of Philosophy in Physics.

[41] G. J. Dolan, “Offset masks for lift-off photoprocessing,” *Applied Physics Letters*, vol. 31, no. 5, pp. 337–339, 08 2008. [Online]. Available: https://doi.org/10.1063/1.89690

[42] S. Schmidlin, “Physics and technology of small josephson junctions,” Ph.D. dissertation, Royal Holloway, University of London, October 2013, a thesis submitted to the University of London for the Degree of Doctor of Philosophy.

[43] A. Osman, “Reliability and reproducibility of josephson junction fabrication - steps towards an optimized process,” *Department of Microtechnology and Nanoscience, Division of Quantum Technology*, 2019.

[44] F. Sterr, “Optimization of josephson junction nanofabrication for superconducting quantum circuits,” Master’s thesis, Technische Universität München, March 2013.

[45] M. C. Rosamond, J. T. Batley, G. Burnell, B. J. Hickey, and E. H. Linfield, “High contrast 3d proximity correction for electron-beam lithography: An enabling technique for the fabrication of suspended masks for complete device fabrication within an uhv environment,” *Microelectronic Engineering*, vol. 143, pp. 5–10, 2015, special Issue on Micro/Nano Lithography with Photons, Electrons & Ions 2014. [Online]. Available: https://www.sciencedirect.com/science/article/pii/S0167931715000295

[46] T. H. P. Chang, “Proximity effect in electron-beam lithography,” *Journal of Vacuum Science and Technology*, vol. 12, no. 6, pp. 1271–1275, 11 1975. [Online]. Available: https://doi.org/10.1116/1.568515

[47] B. Abdo, J. M. Chavez-Garcia, M. Brink, G. Keefe, and J. M. Chow, “Time-multiplexed amplification in a hybrid-less and coil-less Josephson parametric converter,” *Applied Physics Letters*, vol. 110, no. 8, p. 082601, 02 2017. [Online]. Available: https://doi.org/10.1063/1.4976962

[48] J. Y. Qiu *et al.*, "Broadband squeezed microwaves and amplification with a josephson travelling-wave parametric amplifier," *Nature Physics*, vol. 19, no. 5, pp. 706–713, May 2023. [Online]. Available: https://doi.org/10.1038/s41567-022-01929-w

[49] D. I. Schuster, "Circuit quantum electrodynamics," Doctoral dissertation, Yale University, 2007, dissertation Director: Professor Robert J. Schoelkopf.

[50] D. M. Pozar, *Microwave Engineering.* John Wiley & Sons, 2011.

[51] B. Josephson, "Possible new effects in superconductive tunnelling," *Physics Letters*, vol. 1, no. 7, pp. 251–253, 1962.

[52] P. Krantz, M. Kjaergaard, F. Yan, T. P. Orlando, S. Gustavsson, and W. D. Oliver, "A quantum engineer's guide to superconducting qubits," *Applied Physics Reviews*, vol. 6, no. 2, Jun. 2019. [Online]. Available: http://dx.doi.org/10.1063/1.5089550

[53] Ezratty, Olivier, "Perspective on superconducting qubit quantum computing," *Eur. Phys. J. A*, vol. 59, no. 5, p. 94, 2023. [Online]. Available: https://doi.org/10.1140/epja/s10050-023-01006-7

[54] C. Hamilton, "Josephson voltage standards," 2000-10-01 2000.

[55] P. Krantz, M. Kjaergaard, F. Yan, T. P. Orlando, S. Gustavsson, and W. D. Oliver, "A quantum engineer's guide to superconducting qubits," *Applied Physics Reviews*, vol. 6, no. 2, Jun. 2019. [Online]. Available: http://dx.doi.org/10.1063/1.5089550

[56] Y. A. Pashkin, O. Astafiev, T. Yamamoto, Y. Nakamura, and J. S. Tsai, "Josephson charge qubits: a brief review," *Quantum Inf Process*, vol. 8, pp. 55–80, 2009.

[57] P. W. Shor, "Polynomial-time algorithms for prime factorization and discrete logarithms on a quantum computer," *SIAM Journal on Computing*, vol. 26, no. 5, pp. 1484–1509, 1997. [Online]. Available: https://doi.org/10.1137/S0097539795293172

[58] R. Acharya *et al.*, "Multiplexed superconducting qubit control at millikelvin temperatures with a low-power cryo-cmos multiplexer," *Nature Electronics*, vol. 6, no. 11, pp. 900–909, Nov 2023. [Online]. Available: https://doi.org/10.1038/s41928-023-01033-8

[59] A. Patterson *et al.*, "Calibration of a cross-resonance two-qubit gate between directly coupled transmons," *Physical Review Applied*, vol. 12, no. 6, Dec. 2019. [Online]. Available: http://dx.doi.org/10.1103/PhysRevApplied.12.064013

[60] E. Hyyppä *et al.*, "Unimon qubit," *Nature Communications*, vol. 13, no. 1, p. 6895, 2022.

[61] Y. Kim *et al.*, "Evidence for the utility of quantum computing before fault tolerance," *Nature*, vol. 618, no. 7965, pp. 500–505, Jun 2023. [Online]. Available: https://doi.org/10.1038/s41586-023-06096-3

[62] A. D. King *et al.*, "Computational supremacy in quantum simulation," 2024.

[63] Z. K. Minev, T. G. McConkey, M. Takita, A. D. Corcoles, and J. M. Gambetta, "Circuit quantum electrodynamics (cqed) with modular quasi-lumped models," 2021.

[64] M. Göppl, A. Fragner, M. Baur, R. Bianchetti, S. Filipp, J. M. Fink, P. J. Leek, G. Puebla, L. Steffen, and A. Wallraff, "Coplanar waveguide resonators for circuit quantum electrodynamics," *Journal of Applied Physics*, vol. 104, no. 11, p. 113904, 12 2008. [Online]. Available: https://doi.org/10.1063/1.3010859

[65] Z. K. Minev, T. G. McConkey, M. Takita, A. D. Corcoles, and J. M. Gambetta, "Circuit quantum electrodynamics (cqed) with modular quasi-lumped models," 2021.

[66] J. R. Johansson, P. D. Nation, and F. Nori, "Qutip: An open-source python framework for the dynamics of open quantum systems," *Computer Physics Communications*, vol. 183, pp. 1760–1772, 2012.

[67] ——, "Qutip 2: A python framework for the dynamics of open quantum systems," *Computer Physics Communications*, vol. 184, p. 1234, 2013.

[68] V. Schmitt, "Design, fabrication and test of a four superconducting quantum-bit processor," THÈSE DE DOCTORAT, Université Pierre et Marie Curie - Paris VI, 2015, nNT : 2015PA066184, tel-01214394. [Online]. Available: http://www.theses.fr/2015PA066184

[69] A. K. Sarangan, *Nanofabrication: Principles to Laboratory Practice*, 1st ed. CRC Press, 2016. [Online]. Available: https://doi.org/10.1201/9781315370514

[70] P. Hovington, D. Drouin, and R. Gauvin, "Casino: A new monte carlo code in c language for electron beam interaction - part i: Description of the program," *Scanning*, vol. 19, pp. 1–14, 1997.

[71] D. Drouin, A. Couture, D. Joly, X. Tastet, V. Aimez, and R. Gauvin, "Casino v2.42 - a fast and easy-to-use modeling tool for scanning electron microscopy and microanalysis users," *Scanning*, vol. 29, pp. 92–101, 2007.

[72] S. Aya, K. Kise, H. Y. H. Yabe, and K. M. K. Marumoto, "Validity of double and triple gaussian functions for proximity effect correction in x-ray mask writing," *Japanese Journal of Applied Physics*, vol. 35, no. 3R, p. 1929, mar 1996. [Online]. Available: https://dx.doi.org/10.1143/JJAP.35.1929

[73] A. Ripin, E. Connors, and J. Nichol, "urpec matlab package," https://github.com/nicholgroup/urpec, 2018.

[74] N. Muthusubramanian, P. Duivestein, C. Zachariadis, M. Finkel, S. L. M. van der Meer, H. M. Veen, M. W. Beekman, T. Stavenga, A. Bruno, and L. DiCarlo, "Wafer-scale uniformity of dolan-bridge and bridgeless manhattan-style josephson junctions for superconducting quantum processors," 2023.

[75] O. Lounasmaa, *Experimental Principles and Methods Below 1 K*. Acad. Press, 1974. [Online]. Available: https://books.google.com.br/books?id=-p1vtgAACAAJ

[76] P. Das, R. B. de Ouboter, and K. W. Taconis, "A realization of a london-clarke-mendoza type refrigerator," in *Low Temperature Physics LT9*, J. G. Daunt, D. O. Edwards, F. J. Milford, and M. Yaqub, Eds. Boston, MA: Springer US, 1965, pp. 1253–1255.

[77] S. Krinner, S. Storz, P. Kurpiers, P. Magnard, J. Heinsoo, R. Keller, J. Lütolf, C. Eichler, and A. Wallraff, "Engineering cryogenic setups for 100-qubit scale superconducting circuit systems," *EPJ Quantum Technology*, vol. 6, no. 1, p. 2, 2019.

[78] V. Ambegaokar and A. Baratoff, "Tunneling between superconductors," *Phys. Rev. Lett.*, vol. 10, pp. 486–489, Jun 1963. [Online]. Available: https://link.aps.org/doi/10.1103/PhysRevLett.10.486

[79] J. M. Fink, "Quantum nonlinearities in strong coupling circuit qed," Doctoral Thesis, ETH Zurich, Zurich, Switzerland, 2010.

[80] R. Barends *et al.*, "Coherent josephson qubit suitable for scalable quantum integrated circuits," *Phys. Rev. Lett.*, vol. 111, p. 080502, Aug 2013. [Online]. Available: https://link.aps.org/doi/10.1103/PhysRevLett.111.080502

[81] M. Malnou, J. Aumentado, M. Vissers, J. Wheeler, J. Hubmayr, J. Ullom, and J. Gao, "Performance of a kinetic inductance traveling-wave parametric amplifier at 4 kelvin: Toward an alternative to semiconductor amplifiers," *Phys. Rev. Appl.*, vol. 17, p. 044009, Apr 2022. [Online]. Available: https://link.aps.org/doi/10.1103/PhysRevApplied.17.044009

[82] M. Borghesi *et al.*, "Progress in the development of a kitwpa for the dartwars project," *Nuclear Instruments and Methods in Physics Research Section A: Accelerators, Spectrometers, Detectors and Associated Equipment*, vol. 1047, p. 167745, 2023. [Online]. Available: https://www.sciencedirect.com/science/article/pii/S0168900222010373